CHEMICAL VAPOR DEPOSITED GROWTH OF HEXAGONAL BORON NITRIDE ON COPPER AND COPPER-NICKEL BINARY ALLOYS

A Dissertation

by

KARTHIK SRIDHARA

Submitted to the Office of Graduate and Professional Studies of
Texas A&M University
in partial fulfillment of the requirements for the degree of

DOCTOR OF PHILOSOPHY

Chair of Committee,	Luke O. Nyakiti
Committee Members,	Tahir Cagin
	Hong Liang
	Patrick Shamberger
Head of Department,	Ibrahim Karaman

August 2019

Major Subject: Materials Science and Engineering

ABSTRACT

Hexagonal boron nitride (h-BN) is an ultra-wide band gap van der Waals semiconducting material. It has been extensively studied for electronic applications such as tunnel and gate dielectric, and as a substrate for two-dimensional (2D) materials. Large area (mm^2) h-BN films are typically grown using chemical vapor deposition (CVD) on various transition metal foils, including copper (Cu) and nickel (Ni) foils. The growth on Cu is monolayer limited and controlled large area n-layer h-BN remains a challenge. Alternatively, h-BN growth on Ni yields multilayer h-BN films, but results in submicron domain sizes and substrate grain-dependent growth. h-BN films with large crystal sizes and thicknesses are needed for electronic applications, to demonstrate tunnel junction and field effect devices using 2D materials.

In this work, we demonstrate h-BN growth using atmospheric pressure chemical vapor deposition (APCVD) on polycrystalline Cu and Cu-Ni binary alloys. The h-BN growth morphology on Cu was studied using scanning probe microscopy, which revealed a $\approx$1-2 µm crystal size, corrugated nature of h-BN growth, and poor coalescence of h-BN domains. A two-step thermal annealing and electropolishing technique was used to improve the Cu foil surface, which increased the h-BN crystal size from $\approx$1 µm to $\approx$4 µm and reduced secondary nucleation on h-BN films. While these are incremental improvements, the need for n-layer h-BN growth still persists. Thus, we utilized Cu-Ni binary alloys as substrates. The Cu-Ni binary alloys were prepared using electroplating Cu on Ni and Ni on Cu to create Cu-rich and Ni-rich alloys, respectively, and subsequent thermal annealing at 1030°C for >5 hours. This resulted in the growth of well-coalesced monolayered h-BN on Cu-rich alloys with $\approx$15 µm crystal size and multilayered h-BN with $\approx$20 µm crystal size on Ni-rich alloys. Characterization techniques such as atomic force microscopy, electron microscopy techniques, X-ray photoelectron spectroscopy and Fourier transform infrared reflection absorption spectroscopy were used to analyze the alloy substrate morphology, h-BN crystal and film morphology. This work demonstrates the use of alloy composition along with CVD growth parameters to achieve controlled large area n-layer h-BN.

DEDICATION

This work is dedicated to my parents: Ram and Bhanu Sridhara, and my maternal and paternal grandparents.

ACKNOWLEDGMENTS

I would first like to acknowledge my advisor, Dr. Luke Nyakiti, for providing me the opportunity to pursue my graduate studies under his guidance. He has been very patient and calm throughout the ups and downs of research. He has been an excellent advisor and a scientist. I have learnt a great deal of science especially about TEM sample preparation and furnace assembly from him. I would also like to acknowledge, Dr. Boris Feigelson, my supervisor at NRL, who has been an excellent mentor in the past and now. He has provided me more than ample space to let me learn new techniques and to mature as a future scientist. I owe my deepest thanks to both of them.

I would like to thank my TAMU committee members: Dr. Tahir Cagin, Dr. Hong Liang and Dr. Patrick Shamberger from whom I have learnt a lot as a student. Special thanks to Dr. Cagin, with whom I have had many inspiring and intellectual conversations. I would also like to thank my NRL colleagues: Dr. James Wollmershauser, Dr. D. Kurt Gaskill, Dr. Evgeniya Lock, Dr. Jennifer K. Hite, Dr. Fritz J. Kub, for their continued involvement with my work and guidance. Thanks to NRL postdocs Dr. Nick Sharac, Dr. Matt Dejarld, Dr. James Morse and Dr. Shojan Pavunny, with whom I have had many meaningful conversations. Special thanks to my friend, Laleh Emdadi, who supported me throughout my grad school endeavors. Thanks to my friends at Texas A&M: Lorena Garcia, Tim Brown, Heidi Clarke, Arun and Kavya Bhaskar, Avinash Parnandi, Ahmet Tigli, Pavan Akula, all of whom made my time in Texas a very memorable one.

I express my indebtedness and gratitude to my parents Ram and Bhanu Sridhara for their unconditional support during my studies. I express thanks for the hours of reading and review support extended by my family members: Kiran and Abhinaya Sridhara, Dr. and Mrs. Guruswamy, Ram and Ahalya Jalasutram.

My deep and sincere thanks to numerous other friends, officials and colleagues, who had inspired and supported me during the tenure of this work.

CONTRIBUTORS AND FUNDING SOURCES

Contributors

This work was supported by a dissertation committee chaired by Dr. Luke Nyakiti, Dr. Tahir Cagin, Dr. Hong Liang and Dr. Patrick Shamberger. There are two special members on my committee: Dr. Boris Feigelson and Dr. Evgeniya Lock from US Naval Research Laboratory, Washington DC. The following scientists below contributed to this dissertation: Dr. Boris Feigelson assisted and performed growth of h-BN. Dr. James Wollmershauser guided and provided valuable feedback for mechanical polishing of alloys. Dr. Jennifer Hite trained me on the Helios FIB EBSD. Dr. Boris Feigelson and Dr. Luke Nyakiti were involved in data analysis of this work. Dr. Fritz Kub and Dr. Boris Feigelson supervised and funded the work while at US Naval Research Laboratory, Washington, DC.

Funding Sources

Funding for this work has been sponsored by Office of Naval Research. Dissertation writing supported by Boost fellowship from Texas A&M University-Galveston.

NOMENCLATURE

2D	Two-dimensional
AFM	Atomic Force Microscopy
ALD	Atomic Layer Deposition
APCVD	Atmospheric Pressure Chemical Vapor Deposition
BSE	Backscattering Electrons
CM-AFM	Contact Mode Atomic Force Microscopy
CuNi	Cu-rich Cu-Ni alloy with 50-100% Cu
Cu-Ni	Cu-Ni Binary alloy with all compositions of 0% Cu to 100% Cu
CVD	Chemical Vapor Deposition
EBSD	Electron Backscattering Diffraction
EDS/EDX	Energy Dispersive Spectroscopy
EP	Electropolished/Electropolishing
FTIR	Fourier Transform Infrared Spectroscopy
FT-IRRAS	Fourier Transform Infrared Reflection Absorption Spectroscopy
h-BN	Hexagonal Boron Nitride
HTHP	High Temperature High Pressure
LFM	Lateral Force Microscopy
LPCVD	Low Pressure Chemical Vapor Deposition
MBE	Molecular Beam Epitaxy
MIM	Metal-Insulator-Metal
MIMIM	Metal-Insulator-Metal-Insulator-Metal

MP	Mechanically Polished
NiCu	Ni-rich Cu-Ni alloy with 50-100% Ni
SE	Secondary Electrons
SEM	Scanning Electron Microscopy
SPM	Scanning Probe Microscopy
STM	Scanning Tunneling Microscopy
TA	Thermal Annealing/Thermally Annealed
TAEP	Thermally Annealed and Electropolished
TM-AFM	Tapping Mode Atomic Force Microscopy
TMDs	Transition Metal Dichalcogenides
wt.%	Weight Percent
XPS	X-ray Photoelectron Spectroscopy

TABLE OF CONTENTS

Page

LIST OF FIGURES

LIST OF TABLES

TABLE Page

1. INTRODUCTION

1.1 Introduction

The demonstration of electric field effect in graphene [1] led to a new field of two-dimensional (2D) van der Waals materials [2, 3] such as hexagonal boron nitride (h-BN) and transition metal dichalcogenides (TMDs) [3]. These materials are unique because of the ability to isolate 2D atomic layers from the three dimensional (3D) vertical stack. In 3D vertical stacks, each of the 2D atomic layers are held together by van der Waals forces [3]. Out of all the 2D van der Waals materials, graphene has been extensively studied. New applications using graphene have been demonstrated for example, in field effect transistors [4], frequency multiplier [5], photodetectors [6, 7], transparent conducting electrodes [8, 9, 10], plasmonics [11, 12, 13, 14], water filtration [15], and permeation barriers [16] to name a few.

The use of graphene for electronics has been long sought after by researchers [17] due to its exemplary electronic properties marked by experimental observation of massless Dirac fermions, ambipolar behavior [18, 19] and extremely high electron mobility [20]. For graphene to be used as a material of choice in the fabrication of future electronic device applications, such as field effect devices [4], radio frequency (RF) transistors [21], and resonant tunnel devices [22, 23], a suitable structurally compatible insulating material is needed to act as a substrate, tunnel, and gate dielectric.

Hexagonal boron nitride (h-BN), a structurally similar material to graphene, has been proposed as an excellent substrate [24,25], tunnel [26,27], and gate dielectric [28,29,30] for graphene and TMDs alike. Like graphene (Figure 1.1a), h-BN has a honeycomb hexagonal lattice structure with alternating boron and nitrogen atoms in-plane (Figure 1.1b), with each layer held together by van der Waals forces. The interlayer spacing of h-BN is $\approx$ 3.3 Å is similar to graphene, which is $\approx$ 3.35 Å. The small lattice mismatch of $\approx$ 1.7% between graphene and h-BN [24] coupled with the lack of dangling bonds and surface charge trap states, and a low surface roughness of $\approx$

0.9 nm, makes h-BN an ideal substrate for graphene-based electronic devices [31, 32]. Unlike graphene which is a semi-metal, h-BN is an insulator with a very large electronic band gap (5.9 eV) [33] making h-BN an excellent tunnel and gate dielectric ($\varepsilon_r = 4.9$) for vertical heterostructure devices [26, 27, 34]. Recent reports also suggest h-BN as a substrate with high heat dissipation for graphene devices due to h-BN's high thermal conductivity [35] with the coefficient of thermal expansion being α_a=-2.9$\times 10^{-6}$K^{-1} and α_c= 40.5$\times 10^{-6}$ K^{-1} at 297 K [36].

Besides the 2D material applications, h-BN has been gaining attention in its own right for single photon emission [37, 38, 39, 40] and quantum emitting applications [41, 42, 43, 44, 45, 46, 47]. These excellent properties gives h-BN a pivotal role for the success of 2D electronic devices and quantum computing applications.

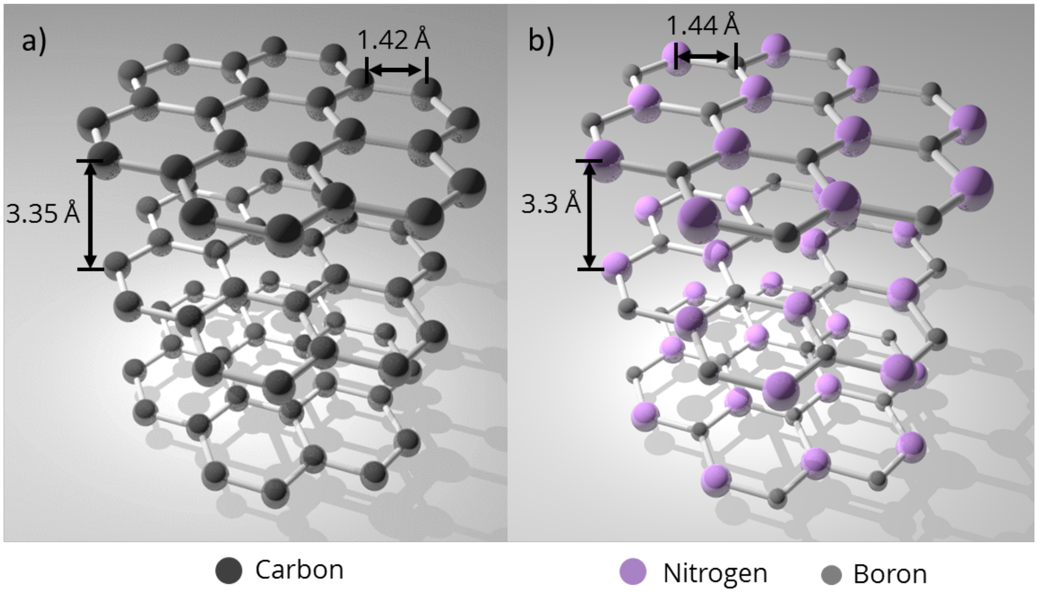

Figure 1.1: The crystal structure of a) graphene, and b) hexagonal boron nitride. In (a), all the atoms represent carbon. In (b), the larger atoms represent nitrogen and smaller atoms are boron [48].

Most of the reported results on the importance of h-BN for 2D electronics are obtained using mechanical exfoliation of h-BN flakes from bulk h-BN crystals. These bulk h-BN crystals are produced using high-temperature high-pressure process (HTHP) [33, 49]. However, only micrometer-sized crystals can be isolated by mechanical exfoliation using scotch tape technique, which is acceptable for proof-of-concept studies in a laboratory environment [50, 51]. Mechanical exfoliation of 2D monolayer structures typically leads to poor yield and is not industrially scalable. Hence, there is a need for large area growth (>1 cm^2) of h-BN (and graphene) for commercial realization of 2D electronic devices.

The growth of h-BN was successfully demonstrated by different research groups using other methods like molecular beam epitaxy (MBE) [52], atomic layer deposition (ALD) [53, 54, 55, 56] and chemical vapor deposition (CVD) [57, 58]. However, CVD is best suited for large area growth of hBN because of its ability to deposit on a variety of substrates, thicknesses, and the growth rates can be precisely controlled. Our group together with other researchers have previously grown graphene and h-BN on transition metal substrates such as Cu, Ni, and Pt using CVD [57, 58, 59, 60, 61, 62, 63, 64, 65, 66, 67, 68, 69].

1.2 Motivation for this work

The CVD growth of h-BN on Cu is known to be self-limiting [64, 70, 71], i.e., typically yielding no more than one to two monolayers of h-BN. On the other hand, CVD growth of h-BN on Ni is not self-limiting, resulting in thicker uncontrolled h-BN films [57, 64]. Therefore, there is a need for a new substrate for the controlled growth of thin (1-2 monolayers) and thick (>3 monolayers) h-BN using CVD.

Si/SiO_2 substrates are often used for the growth of TMDs, and device fabrication of TMD [72, 73, 74, 75, 76, 77, 78, 79, 80] and graphene-based electronic devices [23, 81, 82, 83, 84, 85, 86]. However, Si/SiO_2 is reported to dope the 2D material and deteriorate its electronic properties [24]. Thick (>3 monolayers) mechanically exfoliated h-BN has been used as an intermediate substrate to isolate 2D materials from Si/SiO_2 substrates [24, 87], enabling complete isolation of 2D materials from Si/SiO_2 substrates [24]. As h-BN can be used as a tunnel dielectric, thinner (1-2 monolayers) and thicker (>3 monolayers) h-BN is needed to control the tunneling currents for vertical heterostructure devices as was demonstrated by others using graphene [21, 22, 23, 26, 27]. Similarly, when h-BN is used as a gate dielectric for field effect devices [28, 30], the thickness can be used to regulate the field-effect to control channel currents between the source and the drain of the transistor. However, a precise layer control of h-BN crystals is not feasible with mechanical exfoliation, CVD can be utilized to epitaxially grow monolayered and multilayered h-BN with a large crystal size (>100 µm in size) on Cu and Ni foil substrates.

1.3 Objective of the work

The research results that I report aims to accomplish the following: 1) to understand the growth morphology of h-BN on polycrystalline Cu foil substrates using atmospheric pressure chemical vapor deposition (APCVD) and, 2) to investigate h-BN growth on Cu-Ni binary alloy compositions from 100 wt.% Cu to 100 wt.% Ni. Various surface characterization techniques are used to determine the limitations of the Cu substrate for h-BN growth. To overcome these limitations, novel Cu-Ni binary alloy substrates are developed to assess the feasibility to grow thin and thick h-BN. The general trend of the h-BN growth on the alloys and the alloy composition that results in well-coalesced h-BN film and large multilayered h-BN crystals is reported.

1.4 Impact of the work

Two fundamental outcomes of this work are anticipated, this includes, 1) The growth morphology of h-BN on Cu is assessed, which provides a deeper insight into the limitations of the Cu substrate for h-BN growth. 2) The development of Cu-Ni binary alloys for the h-BN growth is novel and leads to the growth of high quality well-coalesced and multilayered h-BN crystals. This constitutes a major development of a substrate for h-BN growth where the alloy composition, along with the CVD growth conditions, can be used to control the h-BN crystal size and thickness. The isomorphous Cu-Ni binary alloy substrates will consequently complement the current use of Cu substrates as a substrate of choice for h-BN growth. Therefore, the requirement for controlled layer-by-layer growth of h-BN for 2D materials electronic devices can be realized from the results of this work.

1.5 Dissertation outline

The results of the study is presented in five sections. Section two reviews the chemical vapor deposition (CVD) technique in the context of the h-BN growth on various transition metal foil substrates. Section two also outlines the challenges faced in h-BN growth, and the emergence of Cu-Ni alloys as a substrate for the growth of h-BN.

Section 3 discusses the experimental methods used for this dissertation i.e., the preparation of Cu substrates; the development of a two-step thermal annealing and electropolishing processing technique; the preparation of Cu and Ni-based alloys using Ni electroplating of Cu foils and Cu electroplating of Ni foils and subsequent thermal annealing; and the development of the mechanical polishing of Cu-Ni alloys. The experimental section finally examines the APCVD reactor setup, the h-BN growth and characterization conditions.

Section 4 is divided into three subsections. The first subsection details the growth morphology of h-BN on polycrystalline Cu as probed by Fourier transform infrared reflection absorption spectroscopy (FT-IRRAS), scanning electron microscopy, and scanning probe microscopy (SPM) techniques, which shows that the corrugations observed in h-BN film are a reflection of Cu surface. The second subsection expands on the benefits of the two-step thermal annealing and electropolishing processing technique of Cu for improving the growth of h-BN and graphene. The usage of two-step processing technique increases the crystal size of h-BN and reduces the secondary nucleation of h-BN. A similar effect is observed when graphene is grown on surface-prepared Cu. The final subsection of the section analyzes the influence of Cu grain orientation on h-BN growth evaluated using electron backscattering diffraction (EBSD) and SEM technique. The results show that h-BN growth has strong dependency on Cu grain orientations.

Section 5 reports on the successful growth of h-BN on Cu-Ni binary alloy substrates, and is presented in five subsections. The first subsection introduces the surface morphology of the Cu-Ni binary alloys before and after mechanical polishing using SEM and AFM, along with chemical composition and microstructure analysis. The second subsection discusses the general trend of h-BN growth on Cu-Ni alloys, where the amount of h-BN decreases with increasing Cu concentration in the binary alloy. The third and fourth subsections focus on the specific behavior of h-BN growth on $\text{Cu}_{1-x}\text{Ni}_x$ and $\text{Ni}_{1-x}\text{Cu}_x$ alloys. Monolayer well-coalesced h-BN crystals and films are observed to grow on Cu-Ni alloys and large multilayered h-BN crystals are observed to grow on Ni-Cu alloys. The fifth subsection of the section presents a brief discussion on the differences in h-BN growth at the 50 wt.% alloy composition of $\text{Cu}_{50}\text{Ni}_{50}$ and $\text{Ni}_{50}\text{Cu}_{50}$ alloys. The deviation in h-BN growth at this composition is due to difference in the alloy surfaces and microstructures. The key finding of this section is that h-BN grown on Cu-Ni and Ni-Cu alloys exhibit different growth behavior.

Section 6 of the dissertation ends with a summary and conclusions of the work, and how the presented results lead to future work.

2. LITERATURE REVIEW

This section presents a literature review on growth of graphene and hexagonal boron nitride. As the dissertation is focused on h-BN, more attention is given to the h-BN. The review is presented in five subsections: i) A brief introduction on the h-BN growth techniques developed over the years; ii) Synthesis of bulk h-BN crystals using high temperature and high-pressure process; iii) Introduction to relevant aspects of the chemical vapor deposition; iv) Chemical vapor deposition (CVD) growth of graphene on Cu and Ni; and v) Growth of h-BN synthesized using CVD on various transition metal substrates.

2.1 Introduction

The importance of hexagonal boron nitride for 2D electronics and quantum emitters has been briefed in the previous section (Section 1.1). For these applications, there are two primary methods of obtaining h-BN crystals: 1) Top down ad 2) Bottom-up processing techniques [88, 89]. The top down approach involves mechanical exfoliation by repeated peeling and thinning of bulk h-BN crystals using a scotch tape and depositing the thinned crystals from the scotch tape onto Si/SiO_2 substrates [1, 2]. While this method yields high quality h-BN crystals, marked by low concentration of defects and high crystallinity, the domains of such crystals are limited to $\approx$100 µm in size [88, 89]. An added limitation of this laborious process is the lack of control of placing the h-BN crystals in desired location. Methods using poly(dimethylsiloxane) (PDMS) stamp procedure [90, 91, 92, 93] have been developed to increase the control of placement for creating 2D heterostructures. However, the yield is very low and the thickness control (no. of. monolayers) is very poor [88, 89]. On the contrary, bottom-up synthesis involves using scalable CMOS-ready CVD technique on various transition metals that doubles up as both a catalyst to breakdown the precursor molecule and as a substrate for h-BN deposition.

2.2 Synthesis of bulk h-BN crystals

Bulk h-BN crystals are synthesized using a high temperature and high-pressure process (HTHP). One of the seminal works on this synthesis route has been reported by Watanabe et al [33], where the group prepared bulk h-BN crystals using HTHP and at ambient pressure [33, 49]. Figure 2.1 shows the pressure-temperature diagram of hexagonal and cubic boron nitride. The sample was prepared using barium boron nitride ($Ba_3B_2N_4$) solvent system, which was encapsulated in a molybdenum capsule. The sample was then compressed to a pressure of >4 GPa while being annealed to 1500-1750°C. This high temperature and high-pressure condition were subjected on the sample for 20-80 hours, where samples up to 2-4 mm were prepared (Figure 2.1b). These conditions promoted h-BN crystal growth instead of cubic boron nitride (cBN), which require higher pressure and temperature as per the phase diagram (Figure 2.1c). The ambient pressure synthesis differs from the HTHP process where the h-BN powder is placed in a crucible (BN or alumina) with a Ni solvent and heated to $\approx$1350-1500°C. In this process, the h-BN powder and solvent ratio was kept at 1:10. Figure 2.1b and 2.1c show the bulk h-BN crystals prepared using ambient pressure process.

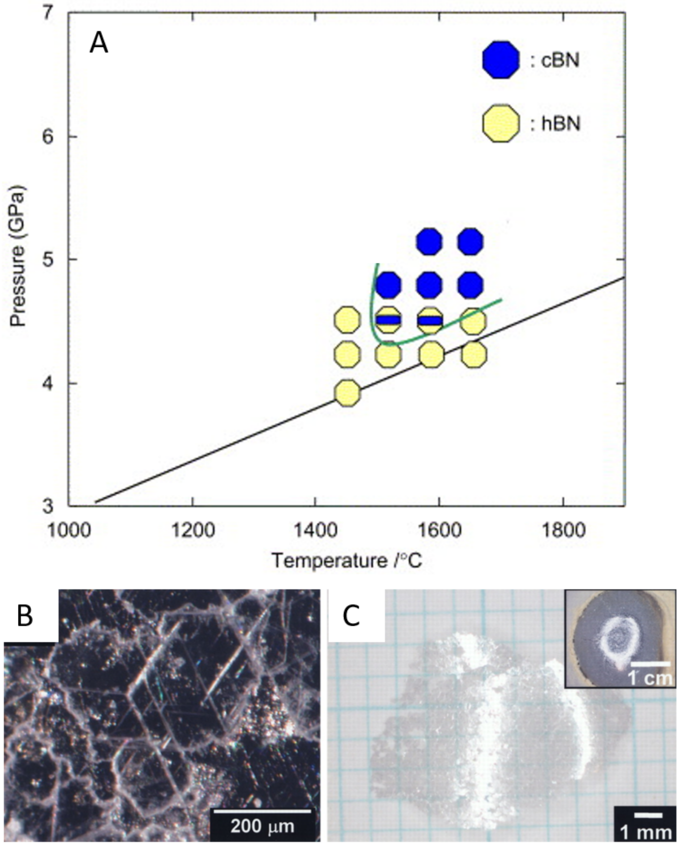

Figure 2.1: a) Pressure-Temperature reaction boundary of cBN formation in Ba–BN solvent [94]. Blue and yellow circles correspond to the recovery of hBN and cBN, respectively. Yellow circle with shaded rectangle corresponds to co-existing of hBN and cBN in the sample. Solid black line is reported as hBN-cBN phase boundary [94]. Optical micrographs of recrystallized hBN obtained with a Ni-Mo solvent. b) Typical hBN crystal on the solidified solvent (as grown) [49]. c) A fragment of aggregate hBN crystals after acid treatment (the inset is an optical micrograph of a recovered sample). The shiny white regions are reflected light [49]. (a) Reprinted with permission from [94]. Copyright 2007 Elsevier. (b-c) Image obtained from [49]. Reprinted with permission from AAAS.

2.3 Fundamentals of chemical vapor deposition

Chemical Vapor Deposition (CVD) is a materials processing technique that involves reaction or decomposition of precursor gases in a furnace with controlled pressure and temperature environment [95]. The precursor gases are transported into the furnace using carrier gases (Ar or N_2), where the flow is regulated by a mass flow controller. As the precursor molecules are broken down, often in the presence of a catalyst, at or near substrate surfaces at high temperature, and a thin film is deposited on the surface [95]. The reactions and the mass transport processes that take place in a CVD furnace is shown in Figure 2.2. Using CVD, both thin (tens of nanometers) and thick films (hundreds of micrometers) of materials can be deposited [95]. A wide variety of materials from metals, ceramics, dielectrics and semiconductors can be deposited [95]. CVD can also be used to deposit films of varying degree of crystallinity i.e. amorphous, polycrystalline and single crystal films [95]. CVD also enables epitaxial (layer-by-layer) growth, which can be used to deposit atomically thin films [95].

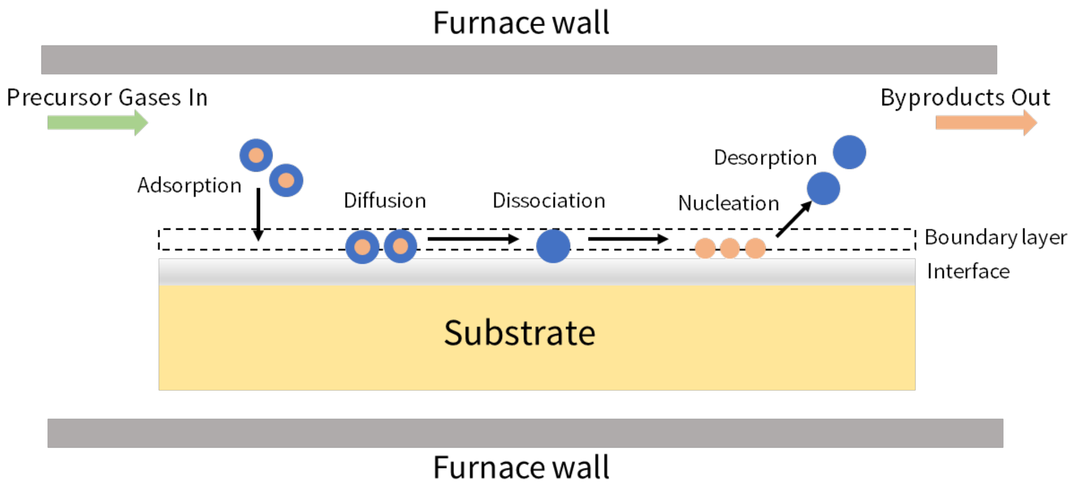

Figure 2.2: Reactions and mass transport in a chemical vapor deposition reactor.

The primary advantage of CVD film growth is that the films are conformal and can be deposited on various structures with sidewalls and steps [95]. CVD also features variable growth rates, where the growth rate can be controlled by a flow control of the precursor gas using a mass flow controller. This enables the growth of films with various thickness. The primary disadvantage of CVD technique is the volatility of precursors and growth or deposition at high temperatures (>500°C) [95]. Despite the disadvantages, CVD is used prominently in microelectronic fabrication [95].

Two-dimensional materials such as graphene and hexagonal boron nitride can be grown using thermal chemical vapor deposition [59, 96]. In this technique, the precursors are sent into the CVD growth chamber, and in the presence of a transition metal catalyst, precursor molecules breakdown leaving being graphene or h-BN. The energy required for the precursor decomposition, catalytic activity, and promotion of lateral crystal and film growth is supplied by heat of the thermal CVD reactor [89]. The primary advantage of using CVD for 2D material growth is the ability to tailor the morphology, crystal sizes and layer thickness by adjusting the growth temperature, pressure, precursors and substrate surface preparation [89].

2.4 Growth of graphene on Cu and Ni

After the mechanical isolation of graphene and the successive experiments [1, 2, 18], there has been a lot of effort to grow graphene on large area substrates ($\approx$1 cm^2) [59]. Graphite has been shown to form on transition metal surfaces such as Ni, as a precipitate, during annealing and cooling processes from atmospheric carbon [97, 98, 99]. This once problematic method of graphite growth is currently being reconsidered as a means to grow graphene [100]. Graphene has been shown to grow on a variety of substrates by the thermal decomposition of a hydrocarbon source, such as methane and ethanol, on both single crystal and polycrystalline: Ir, Ru, Co, Pt, Ni and Cu [59, 60, 61, 100, 101]. The most common transition metal substrates used for CVD graphene growth are polycrystalline Cu [59] and Ni [60], due to their abundance and low cost.

The mechanisms of graphene growth on transition metal substrates takes either one of two forms: segregation-diffusion or catalytic breakdown of a hydrocarbon molecule. Growth of graphene on Ni (polycrystalline Ni) involves segregation and diffusion of carbon in Ni, while growth on Cu (polycrystalline Cu) involves catalytic breakdown (dehydrogenation) of hydrocarbon molecule [59, 59, 60, 100, 101]. The two different mechanisms of graphene growth can be traced to the solubility of C in metal, which can be ascertained from the phase diagram (Figure 2.3). Carbon is not soluble in Cu, as can be seen by lack of a distinct C-Cu phase formation (Figure 2.3a). In C-Ni system (Figure 2.3b), carbon is soluble in Ni forming a metastable solid solution with a solubility of $\approx$0.6 at.% C in Ni at $\approx$1000°C. At this temperature, C diffuses into the bulk of Ni and on cooling, C atoms from the bulk diffuse onto the surface forming hexagonal sp^2 structure leading to graphene (or graphite) [60, 100].

While this method leads to large area graphene growth, the lack of control for uniform single layer graphene and small graphene grain size is problematic. In recent years, there have been reports of controlled bilayer graphene growth on polycrystalline Ni foils [60]. However, another transition metal, Cu, has shown greater promise of large area uniform single layer graphene growth [59, 100]. Growth on Cu involves the catalytic breakdown of hydrocarbon molecule such as methane (CH_4) at >900°C. The carbon atoms dissociated from the hydrocarbon precursor nucleate on the Cu surface and form a hexagonal crystal structure leading to graphene growth [59]. Unlike Ni, single layers of graphene can be grown on Cu foils leading to the commercial viability of mass producing monolayer graphene using CVD [102].

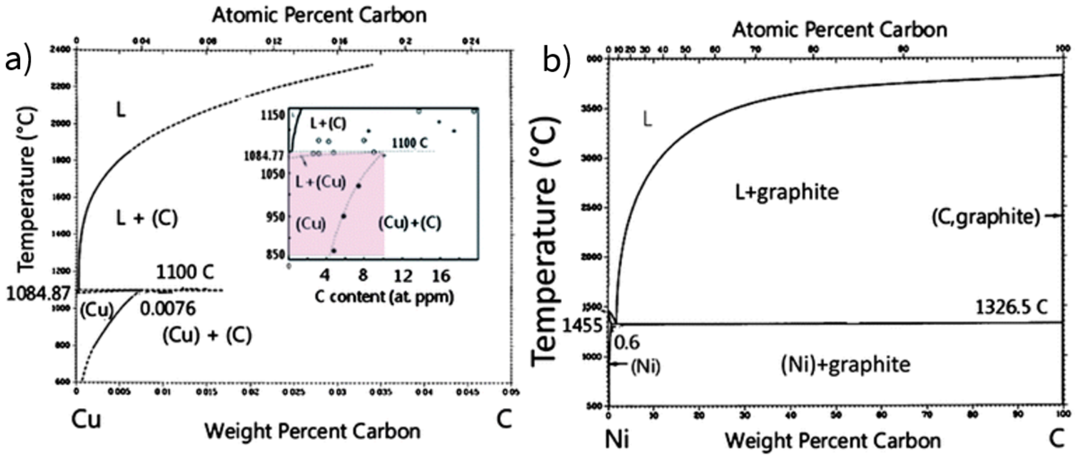

Figure 2.3: a) C-Cu phase diagram and b) C-Ni phase diagram. Carbon shows no solubility in Cu but is partially soluble in Ni [100]. Reprinted with permission from [100]. Copyright 2011 Royal Society of Chemistry.

2.5 Synthesis of h-BN on transition metal substrates

Like graphene, the growth of h-BN using CVD has been explored on various transition metal substrates such as Pt, Ir, Ru, Co, Cu and Ni [62, 63, 103, 104, 105, 106, 107, 108]. The various substrates that were used for h-BN growth have been summarized in Table 2.1. A typical furnace setup for growing h-BN is shown in Figure 2.4a. While graphene growth takes place in either of the two mechanisms (segregation-diffusion or catalytic breakdown) depending on the substrate, h-BN grows by means of catalytic decomposition of boron-nitrogen source [57, 58, 64].

Table 2.1: Substrates for the CVD growth of h-BN nanosheets in the context of the periodic table [88]. Table obtained with permission from [88]. Copyright 2017 Elsevier.

Period	Group				
	6	8	9	10	11
4	Cr [109]	Fe [108, 110, 111, 112]	Co [113]	Ni [57, 114, 115, 116, 117, 118, 119, 120, 121]	Cu [28, 58, 64, 66, 67, 68, 69, 115, 122, 123, 124, 125, 126]
5		Rh [127, 128] [127]	Ru [103, 129, 130, 131]	Pd [132]	Ag [133]
6			Ir [107]	Pt [62, 134, 135]	Au [136]

The primary precursors used for h-BN growth are ammonia borane or borazane (H_3NBH_3) and borazine ($B_3H_6N_3$) [57, 58, 64]. Unlike graphene growth where the hydrocarbon source, methane (CH_4) decomposes to C and H_2, the decomposition of ammonia borane and borazine is more complicated. Ammonia borane decomposes below its melting temperature (106°C) producing hydrogen, monomeric aminoborane (BH_2NH_2) and borazine ($B_3H_6N_3$) (Figure 2.4b). Additionally, both monomeric aminoborane and borazine breakdown further forming hydrogen and h-BN on the substrate surface [64]. On the other hand, borazine undergoes dehydrogenation forming polyborazylene ($\approx$70°C), which further dehydrogenates leading to elemental boron and nitrogen on the substrate surface, forming h-BN films [57]. While borazine has a slightly simpler decomposition, ammonia borane is a more common precursor used to grow h-BN due to its relative stability in a laboratory ambient, wider availability and reduced moisture sensitivity than borazine [64]. Auwaerter et al and Mueller et al have used β-tricholoroborazine for h-BN growth on Ni(111) and Pt(111), respectively [114, 135]. The β-tricholoroborazine precursor is reported to release HCl gas when exposed to humidity, which is corrosive to the metal piping and valves of the CVD reactor furnace [88]. Besides the more common ammonia borane and borazine, other precursors for h-BN growth were also demonstrated shown in Table 2.2 [88]. Besides single compound precursors, multi-compound precursor with a 1:1 ratio of B and N were also demonstrated as shown in Table 2.2 [88]. However, unlike single compound precursor, the multi-compound precursor is more complicated as it requires precise control to maintain the B and Ni stoichiometry [88]. Therefore, very few reports present demonstrating h-BN growth using multi-compound precursors.

Table 2.2: Table of precursors used for h-BN growth [88]. Table obtained with permission from [88]. Copyright 2017 Elsevier.

Precursor	Quality of h-BN	Growth Conditions	Ref
Ammonia Borane	Single crystalline h-BN with domain size up to centimetre size was obtained. Mono- to multilayers have been grown on various substrates	Growth temperature varies from 700 to 1100°C. APCVD and LPCVD systems are often used	[58, 66, 122, 123, 134, 137, 138, 139, 140, 141, 142,143]
Borazine	Monolayer and few-layered h-BN have been achieved. Monolayer with domains as large as 0.3 mm has been reported	UHV-CVD, LPCVD, and conventional APCVD systems have been used Growth temperature varies from 700 to 1000°C	[28,109, 110, 111, 118, 135, 143, 144, 145]

Table 2.2: Continued

Precursor	Quality of h-BN	Growth Conditions	Ref
β-Tricholoroborazine	Monolayer on Ni (111) and Pt (111) substrates was achieved	Growth was carried out using a UHV system at 723°C	[114,135]
Diborane and ammonia	h-BN film thickness (monolayer to 100-layers) and crystallinity are dependent on the choice of substrates, deposition time, and sequential exposures of the precursors	Growth was carried out in an LPCVD system at 600-1025°C	[116,146]
Decaborane and ammonia	Thickness was about 2 nm on Ni and 2-15 nm on Cu	Growth was carried out at 1000°C for 10 min in an APCVD system	[147]
Dimeric diborazane and trimeric triborazane	Thickness was about 2-5 nm. Compared to ammonia borane, these precursors led to faster growth rates and more polymeric particles	The precursors decompose around 80-90°C. The growth was carried out at 1040°C in an APCVD system	[148]
BCl_3, NH_3, N_2, and H_2	The maximum thickness was about 10 nm	Growth temperature was 1000 °C in an APCVD system	[149]

Table 2.2: Continued

Precursor	Quality of h-BN	Growth Conditions	Ref
BF_3, N_2, and H_2	1-8 layer thick and a domain size of up to 4 μm were obtained	Microwave plasma CVD system was used for the growth. The microwave power, growth temperature, and time was 800 W, 800°C, and 1 hour, respectively	[150,151]
Trimethylamine	Monolayer h-BN and h-BCN films were grown on Cu. With a sublimation temperature above 40°C, 2-5% carbon doping can be achieved	Growth was carried out at 1050°C for 5-20 min using an APCVD system	[152]
Trimethylborate, O_2, and ammonia	h-BN monolayer	Growth was carried out in a three step boration-oxidation–nitration process in a LPCVD system	[128]

The growth of h-BN films remains sensitive to the growth pressure of the CVD reactor and the choice of LPCVD or APCVD growth of h-BN is dependent on the availability of equipment in the research group and final desired product (Table 2.3) [89]. Both monolayer and multilayered h-BN films have been grown in a low-pressure CVD (LPCVD) system (2-200 Torr) on Cu and Ni with varying degrees of uniformity [57, 58, 64, 66]. The operating pressure (low pressure or ambient pressure) of the CVD reactor dictates if the growth mechanism is surface limited (as in LPCVD) or mass-transport limited (APCVD) [89].

Table 2.3: Table shows various h-BN growth routes taken by the community [89]. Table reprinted with permission from [89]. Copyright 2018 Royal Society of Chemistry.

Substrate	CVD route	Growth temp. (°C)	Precursor	Layer no.	Single domain (mm^2)	E_g (eV)	Key parameter	Ref.
Cu foil	APCVD	1000	Ammonia borane	2-5 layers	-	5.56	-	[58]
Cu foil	APCVD	1000	Ammonia borane	6-8 layers	-	-	Cu morphology	[123]
Cu foil	LPCVD	1000	Ammonia borane	Monolayer	0.5	6.07	-	[64]
Cu foil	APCVD	1050	Ammonia borane	Monolayer	35	6.04	Surface smooth	[66]
Cu foil	LPCVD	1000	Ammonia borane	Monolayer	170	-	Cu pretreatment	[153]
Cu foil	LPCVD	1000	Ammonia borane	Monolayer	2200	5.9	Using Cu enclosure	[154]
Cu foil	APCVD	1065	Ammonia borane	Monolayer	170	5.85	Synthetic control	[124]
Ni film	APCVD	1000	Borazine	5–50 nm	-	5.92	Precursor dosage	[57]
Ni(111)	APCVD	800-1030	Ammonia borane	Few-layers	-	-	Repeated growth	[145]

Table 2.3: Continued

Substrate	CVD route	Growth temp. (°C)	Precursor	Layer no.	Single domain (mm^2)	E_g (eV)	Key parameter	Ref.
Pt foil	LPCVD	1100	Ammonia borane	Monolayer	-	6.06	Repeated growth	[134]
Pt foil	APCVD	1000	Ammonia borane	1–3 layers	0.5 (for monolayer)	6.07 (1L), 5.94 (2L)	Repeated growth with layer controllability	[62]
Fe foil	LPCVD	1100	Borazine	5–15 nm	-	-	Furnace cooling rate	[112]
Fe foil	LPCVD (cold-wall)	900	Borazine	Monolayer	170	-	NH_3 pre-annealing	[111]
Fe-Ni	LPCVD	900-1100	B,N-Solid source	Monolayer, few-layers	-	5.8	Co-Segregation	[155]
Cu-Ni	LPCVD	1050-1085	Ammonia borane	Monolayer	7500	-	Tuning Ni dosage	[156]

As h-BN is composed of alternating boron and nitrogen, the domain shape of h-BN can vary with N or B termination. Preliminary investigations reveal that h-BN forms triangular and hexagonal shapes (Figure 2.4) [64, 157]. The triangular crystal shapes are the most frequently occurring as they are more thermodynamically favorable than the hexagonal shape due to nitrogen-terminated edge [64]. Other crystal shapes such as truncated triangles can also exist, which might indicate a faster growth edge [157]. The shape control is reported to be achieved by substrate modification through the creation of oxygen-rich Cu surface [66, 89]. It was reported that the high-oxygen concentration reduced the energy barrier for the formation of both nitrogen- and boron-terminated edges leading to the formation of hexagonal domains of h-BN [66, 89]. Zhang et al have theoretically shown that the h-BN domain shape can be manipulated by altering the B and N stoichiometry [157]. Stehle et al have experimentally shown that the stoichiometry can be altered by placing the Cu substrate further down the horizontal CVD reactor, away from the precursor inlet [124, 125]. This led to the h-BN domains change from triangular shapes to a more hexagonal domain structure [124].

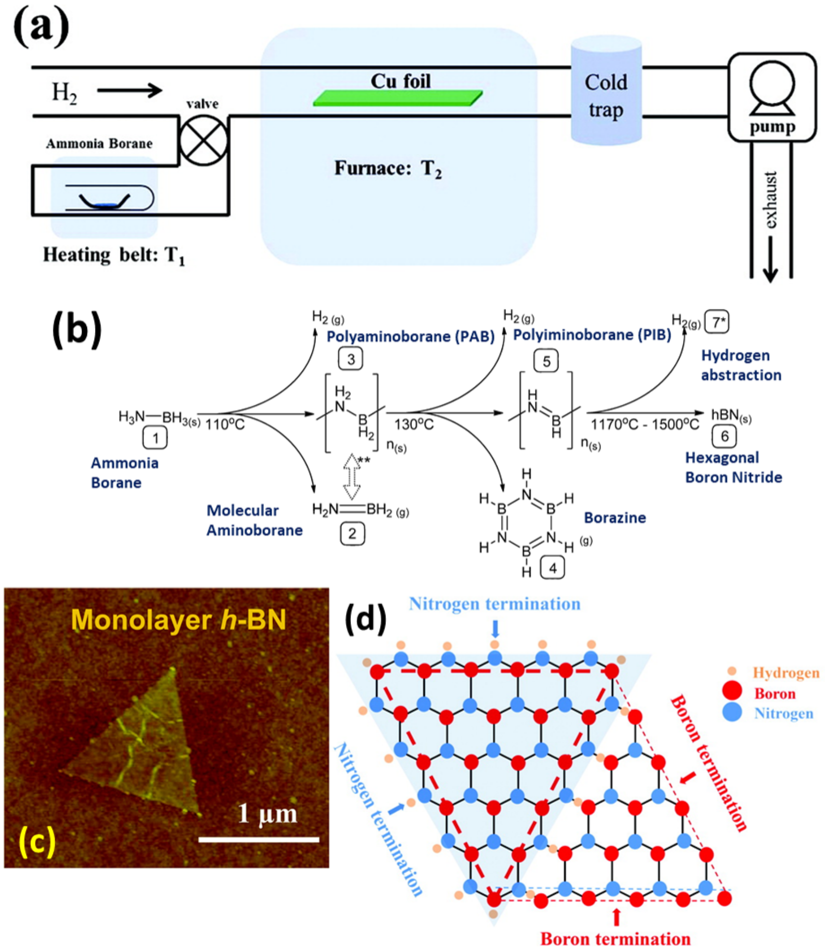

Figure 2.4: Figure showing the h-BN growth furnace from [64]. a) The growth chamber commmonly used for h-BN synthesis, b) Experimentally observed chemical pathways in the pyrolytic decomposition of ammonia borane to h-BN: species found to be involved in ammonia borane pyrolysis: [1] Ammonia Borane; [2] Molecular Aminoborane; [3] Polyaminoborane (PAB); [4] Borazine; [5] Polyiminoborane (PIB); [6] Semi-Crystalline P63/mmc (hexagonal) boron nitride; [7] Hydrogen abstraction by the evolution of molecular hydrogen at high temperature [137], c) Shows triangular shaped monolayer h-BN, d) A schematic showing nitrogen-terminated triangular-shaped h-BN [64]. (a) Reprinted with permission from [64]. Copyright 2012 American Chemical Soceity. (b) Reprinted with permission from [137]. Copyright 2011 American Chemical Society. (c-d) Reprinted with permission from [64]. Copyright 2010 American Chemical Society.

2.5.1 Growth on Cu

The growth of h-BN on Cu has been extensively investigated by our research group and others [58,64,66,67,68,69,71,115,122,123,126,140,141,142,158,159,160,161,162,163,164,165,166,167] because of the ability to grow monolayer graphene enabling future epitaxial growth of graphene and h-BN heterostructures [28,112,168,169]. The initial work was done by Song et al [58] demonstrating the synthesis of few layer h-BN films using APCVD and ammonia borane precursor. Extensive optical and mechanical characterization revealed that the electronic and structural integrity of the h-BN films grown was of high quality. Monolayer h-BN growth on Cu was demonstrated by Kim et al using LPCVD and ammonia borane as the precursor [64]. Extensive characterization using AFM, TEM and electron energy loss spectroscopy (EELS) suggested that the monolayer h-BN growth is surface mediated [64]. The subsequent work beyond these two reports has been to reduce the impurity density from the precursor [140, 161], and improve the surface morphology of Cu substrate [66, 69]. Sridhara et al reported a surface preparation technique using thermal annealing and electropolishing that led to a roughness of $\approx$1.1 nm [69]. There were also efforts to understand the role of Cu grain orientation on h-BN growth [68, 163]. While these are major advancements, the controlled layer-by-layer epitaxial growth still eludes the community. In recent years, Lin et al synthesized wafer-scale h-BN films with monolayer thickness control [71]. They demonstrated this by having a variable pressure CVD growth chamber. By altering the pressure, the CVD growth can be changed from LPCVD and APCVD, and thus n-layer h-BN film growth was demonstrated on Cu.

2.5.2 Growth on Ni

Ni remains a popular substrate, after Cu, for the growth of h-BN [57, 63, 65, 114, 116, 121, 143, 145, 170]. The use of Ni for h-BN growth is justified by the observation of graphene growth on Ni. Large area h-BN films (5-50 nm thickness) on polycrystalline Ni was demonstrated using borazine as the precursor with an APCVD furnace [57]. From the optical micrographs and AFM images, complete and uniform coverage of h-BN film was reported. However, the film was reported to be thicker along the Ni substrate grain boundary than on the grain center [57]. In other reports [65], h-BN grown using LPCVD on polycrystalline Ni showed a strong Ni grain orientation dependency as assessed using EBSD on polycrystalline Ni substrate with h-BN and Raman spectra of h-BN. Ni(100) grains had thicker films indicating a faster growth orientation. However, Ni(111) had little or no detectable h-BN, indicating a slow growth orientation. As the surface morphology and grain orientation of the Ni substrate are the two primary contributing parameters, Cho et al also assessed the role of the Ni grain orientation on h-BN growth rate [63]. The group used electrochemical polishing to suppress the role of the surface and thermal annealing to expose the pristine Ni surface. After performing EBSD and SEM post-growth on the surface finished Ni substrate, the h-BN growth rate on {100} and {110} orientations had much higher growth rate owing to higher surface energy [63]. Besides polycrystalline Ni substrates, h-BN was also grown on single crystal Ni(111) to assess the stacking of h-BN [114] and to assess the dehydrogenation reaction process of ammonia borane and borazine [143]

2.5.3 Growth on Pt

After the successful demonstration of graphene growth on Pt [61,171,172,173], h-BN was also grown on Pt using CVD [62, 134, 144]. Similar to Cu, h-BN growth on Pt was strongly dependent the chamber pressure and precursor amount. Lower pressure led to the growth of monolayer h-BN due to self-limiting h-BN growth and ambient pressure led to the growth of few-layer h-BN films. In this work, Gao et al [62] have reportedly been able to grow mono, bi and few-layer h-BN films just by tuning the precursor concentration in ambient pressure. Additionally, after transferring the h-BN films using electrochemical bubble method, they have reported that the h-BN films can be repeatedly grown on the same substrate without having to sacrifice the expensive Pt substrate during the transfer process. This remains one of the major advantages of h-BN growth on Pt, which has not yet been reported for Cu or Ni substrates.

2.5.4 Growth on Fe

As h-BN is an insulator with a band gap of $\approx$5.9 eV, it makes for a good tunnel dielectric for magnetostrictive devices such as magnetic resistive random-access memory (MRAM) [174, 175, 176, 177, 178, 179]. Unlike Cu, Ni and Pt, Fe and Co are ferromagnetic, and hence can be used as a substrate and contact to demonstrate MRAM devices with h-BN as the dielectric. Fe was the earliest substrate on which CVD h-BN films were demonstrated by Takahashi et al in

1979 [96] and was revisited again by Kim et al in 2015 [112]. h-BN films of variable thickness has been grown on Fe using CVD using borazine vapor and H_2 at $\approx$1100°C [112]. The thickness of the film was reportedly dependent on the cooling rate of the sample, where a fast cooling rate (30°C/min) led to thinner films ($\approx$12 nm thickness) and slower cooling rate (5°C/min) led to thicker films ($\approx$18 nm thickness). The h-BN film growth on Fe is understood to be via both surface-mediated and precipitation from the experimental results [89, 112]. Besides few layer h-BN growth, monolayer h-BN growth has also been demonstrated on Fe using CVD by Caneva et al [111]. This was achieved by exposing the Fe substrate to NH_3 during the pre-anneal step before growth [111]. This limited the intake of B and N species into the bulk of the Fe substrate, enabling the growth of monolayer h-BN, leading to film layer number control and greater film homogeneity [89, 111].

To-date, most efforts to synthesize h-BN films on Cu are achieved using large-area continuous monolayer films using CVD [180], which have been demonstrated successfully. However, uniform growth and larger single crystal growth of h-BN have not been thoroughly investigated in these efforts. This work therefore utilizes numerous surface preparation techniques such as electropolishing to alter the Cu substrate to facilitate larger single crystal growth, along with uniformity by controlling the nucleation sites, surface roughness and the grain size of the Cu substrate [69, 126]. The electrochemical polishing approach has also led to an increase of h-BN crystal size and reduction in density of h-BN crystals [69, 126]. While each of the transition metal substrate offers an advantage, using a combination of transition metals, namely alloys might provide combinatorial advantages. The primary advantages of using an alloy is to control the catalytic rate (precursor breakdown rate) and nucleation site density. With this idea, both graphene and h-BN growth on transition metal alloys have been demonstrated.

2.6 h-BN growth on metallic alloys

Some of the earlier works on the growth of 2D materials on binary Cu-Ni alloys have been on graphene [115, 181, 182, 183, 184, 185, 186, 187, 188]. The Cu-Ni alloy substrates are promising as large single crystal growth of h-BN on Cu-Ni alloys was reported. The work by Lu et al. [156], demonstrated single crystals of h-BN as large as 7500 µm^2 on Cu-Ni alloy and with a composition of 20% Ni [156]. Figure 2.5a shows the Cu-Ni alloying process and Figure 2.5b shows h-BN crystals (triangular-shaped) grown on the Cu-Ni alloys [156]. This approach was claimed to reduce the number of nucleation sites on the substrate to facilitate large single crystal growth as shown in Figure 2.5d. With the introduction of Ni in Cu, the number of h-BN nuclei dropped from 10 at.% Ni to 30 at.% Ni with 20 at.% Ni concentration showing the largest h-BN crystal. However, upon further increasing to 30 at.% and 50 at.% Ni concentration, there was little or no growth of the h-BN crystal, respectively. The growth rates were also reported to drop in 30 at.% Ni concentration samples from 0.3 µm·min^{-1} to 1.2 µm·min^{-1} in 20 at.% Ni concentration.

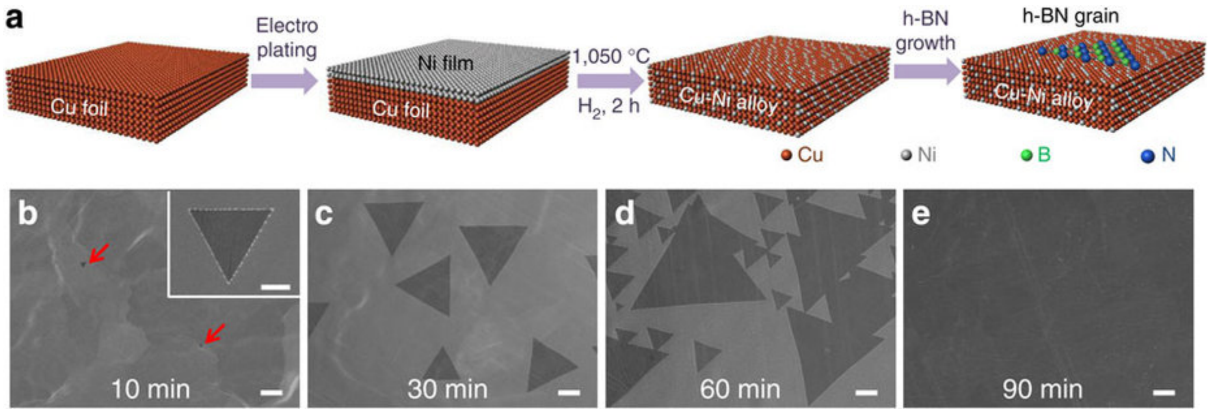

Figure 2.5: a) Schematic illustration showing the procedure of h-BN growth. b-e) Typical SEM images of h-BN grains grown on Cu-Ni alloy foils with 15 atom % Ni at 1085 °C for 10, 30, 60 and 90 mins, respectively. The red arrows in (b) show the sites of the h-BN grains, while the inset shows the enlarged image of one as-grown h-BN grain. The scale bars in (b-e) are 20 µm, and in the inset in (b) is 2 µm [156]. Figure obtained with permission from [156]. Copyright 2015 Springer Nature.

Despite showing promising results of large single layer h-BN crystal on Cu-Ni alloys [156], there was no discussion presented on how the substrate surface morphology played a role in facilitating large single crystal growth. There have been recent reports of improved crystal growth with better surface preparation [63, 69, 126], which remains unaddressed in this body of work. The large drop in growth rate on Cu-Ni substrates with Ni concentration changing from 20 at.% to

30 at.% was also not substantiated and requires further examination as the large h-BN crystal size could be due to the surface morphology of the alloy surface. A brief discussion was presented on growth rates on 20 at.% Ni concentration and 30 at.% Ni concentration samples calculated from h-BN crystal size/growth time relation. However, a comprehensive growth rate study showing the change in h-BN crystal size at every growth time step, especially in comparison with Cu (control sample), remains missing [156]. There have also been a graphene/h-BN device fabricated showing an electron mobility of 10,000 cm^{2}V^{-1}s^{-1} to attest the quality of h-BN [156], which is on the lower end of the expected range from 20,000 to 80,000 cm^{2}V^{-1}s^{-1} [24]. Nevertheless, this remains the most promising report to date of large area single crystal h-BN grown on Cu-Ni alloy.

There are several challenges unaddressed in this work by Lu et al [156] which present an opportunity for further in-depth inquiry on the growth of h-BN on Cu-Ni alloys. While this dissertation overlaps with this report by Lu et al [156], it expands on the following. h-BN is grown on the Cu-Ni binary alloys at every 10 wt.% using APCVD. The growth pattern of h-BN on the complete set of Cu-Ni binary alloys is shown and discussed. The role of the alloy substrate preparation on improving the h-BN morphology is presented. Finally, the contribution of alloy surface and the microstructure in dictating h-BN growth is addressed in this dissertation (refer Section 5).

The purpose of this section is to discuss the different experimental methods that were used for the study. Figure 3.1 summarizes the general experimental methodology that were employed for this study. The first two subsections of this section will be focused on the preparation of Cu samples, and electrochemical polishing of Cu. The rest of the subsections will discuss the preparation of Cu-Ni alloys. This includes brief overview of electroplating, initial attempts to prepare binary Cu-Ni alloy using electroless plating, preparation of Cu-rich and Ni-rich alloys using electroplating, and mechanical polishing of Cu-Ni alloys. Finally, the h-BN growth conditions, the APCVD reactor setup and the subsequent characterization conditions are discussed.

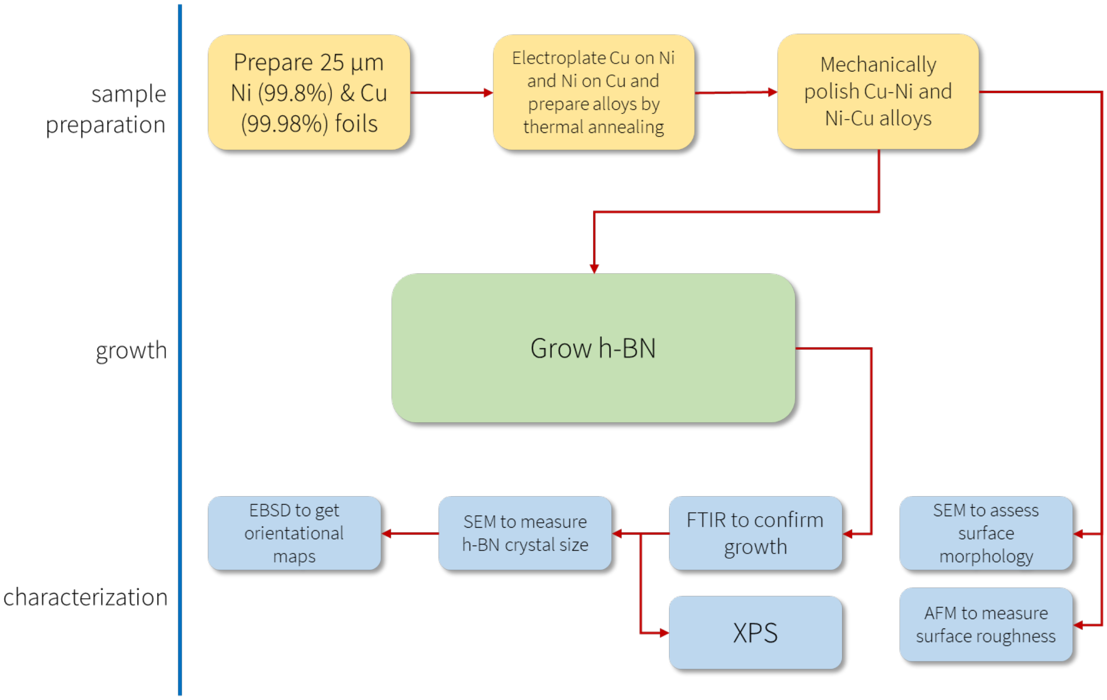

Figure 3.1: The general experimental methodology for this work.

3.1 Preparation of Cu samples

Cu foils of two purities were obtained from the vendor, Alfa Aesar with the following concentrations, Low purity Cu (99.98% pure) and high purity Cu (99.999% pure). Low purity Cu was used for the preparation of Cu-Ni alloys, which is discussed subsequently. High purity Cu was the primary substrate that was used to grow and study the h-BN growth morphology. The preparation methods described in this subsection are for high purity Cu. The as received Cu were cut into strips of $\approx$7 mm $\times$ 30 mm. These strips were annealed in reduction environment with H_2/N_2 gases flowing at 200 sccm to 500°C to soften the foils and enlarge the Cu grain size [189, 190, 191, 192]. After the foils were annealed, they were cut into smaller pieces of $\approx$ 7 mm $\times$ 7 mm into right trapezoidal shape as shown in Figure 3.2. Such a shape creates a one-fold symmetry, and the front (the growth face) and the back faces can be identified. The foils were then pressed to $\approx$0.35 GPa in between two stainless steel anvils using a hydraulic press to induce plastic deformation. The plastic deformation promotes Cu grain enlargement during following thermal annealing [189] detailed in the succeeding subsections. After the plastic deformation pressing process, the samples were placed in a plastic container and stored in a nitrogen-ambient cabinet .

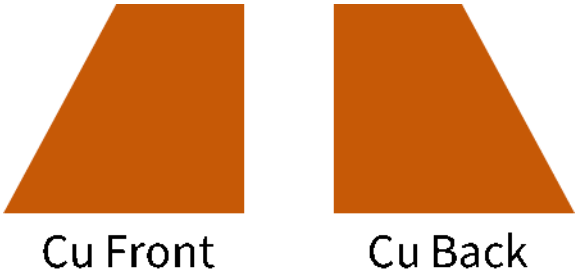

Figure 3.2: Schematic of the trapezoidal cut of Cu samples showing front and back side.

3.2 Electrochemical polishing of Cu

Electrochemical polishing (EP) is used in this work for surface finishing of high purity Cu samples that have been plastically deformed using the hydraulic press, and a brief introduction to EP is necessary. EP is an electrochemical technique that involves selective etching of metal surfaces in a chemical bath in a controlled manner [193, 194, 195, 196, 197, 198, 199]. The control is achieved by selection of electrochemical baths (commonly acids) and electrode potentials that actively take part in the controlled dissolution of metal atoms from the anode (positive electrode). During the dissolution process, the anode undergoes surface smoothening and brightening (removal of microscopic features) as part of the anodic reaction process [193,194,195,196, 197, 198, 199].

Electropolishing takes place in an electrochemical cell, as shown in Figure 3.3a, consisting of an anode (positive, working electrode), cathode (negative and counter electrode), and an electrochemical bath. A reference electrode is used optionally. The pH of the bath and the potential energy applied across the working electrode (anode) will dictate if the working electrode undergoes electropolishing. It can be determined by a Pourbaix diagram. The anodic reaction process is governed by the following half-cell reaction process: $\mathrm{Cu} \longrightarrow \mathrm{Cu}^{2+} + 2\,e^-$ and the oxidation cell potential is E = -0.339 V [199, 200]. The surface morphology of the Cu anode consists of high regions (hills) and low regions (valleys), which create a concentration gradient of Cu when a potential is applied. The concentration gradient (hills) creates high chemical resistive regions, which are selectively etched away during the electropolishing process, leading to a smooth or uniform surface finish of the Cu substrates [193,197]. For this work, a recipe was developed with phosphoric acid (50 ml), ethylene glycol (25 ml) and acetic acid (25 ml) in a 100 mL solution (2:1:1 ratio) [48, 69]. The applied potential on the Cu anode varies from sample to sample in 2.5-3.5 V range. The electropolishing setup is shown in Figure 3.3a and 3.3b. The details of the electropolishing recipe for Cu has been reported in the following literature [48, 69].

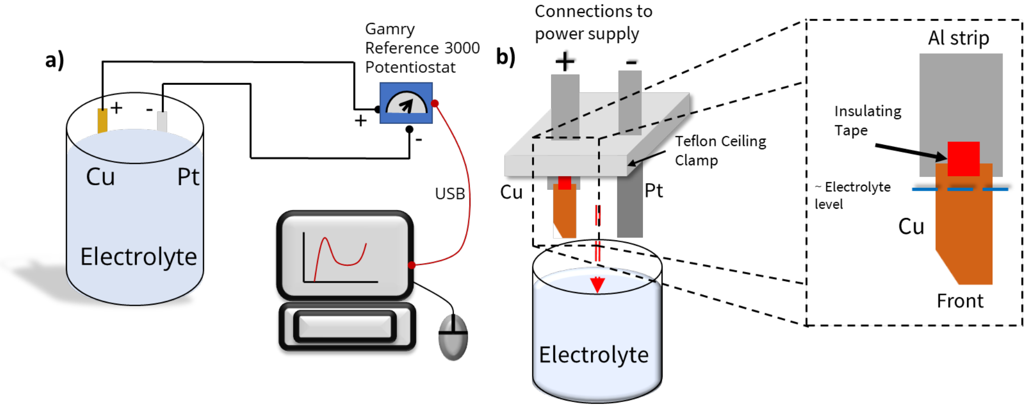

Figure 3.3: a) Electrochemical cell used for electropolishing of Cu. The working electrode (anode) is Cu and the counter electrode is Pt. The electrolyte composes of Phosphoric acid (H_3PO_4), ethylene glycol, and acetic acid in a 2:1:1 ratio. b) Shows how the electrodes are mounted and inserted into the electrolyte.

3.3 Introduction to electroplating

Electroplating is an electrochemical technique that involves deposition of metal atoms, which are transported via an electrolytic bath, from the anode to a cathode [201]. As the mass transport involves electrochemical dissociation of molecules at the anode and deposition on a cathode, the electroplating process is predominantly used to deposit metals on conductive surfaces. Electroplating is governed by both anodic and cathodic half-cell reactions: $\mathrm{Me\,(s)} \longrightarrow \mathrm{Me^{+}\,(aq)} + \mathrm{e^{-}}$ (Anodic reaction) and $\mathrm{Me^{+}\,(aq)} + \mathrm{e^{-}} \longrightarrow \mathrm{Me\,(s)}$ (Cathodic reaction), where Me is the metal ion in solid (s) and aqueous (aq) form and $\mathrm{e^{-}}$ is the electron [199, 200, 201]. Electroplating of metals such as Cu, Ni, Cr, and Al have been studied extensively for research and industrial applications such as coatings [199, 201, 202, 203, 204].

3.4 Preparation of binary Cu and Ni-based alloys

During the preliminary stages of this work, Cu-rich (Cu-Ni) alloys were prepared by electroless plating of Ni on Cu foils. The electroless plating was performed first by placing a Cu substrate foil in Transene Ni Strike bath and heated to ≈60-65°C on a hot plate, which deposits a thin Ni seed layer across the foil surface. This step was followed by heating the samples in Nickelex to ≈90-95°C on a hot plate. The temperature was measured using a mercury probe thermometer.

Numerous samples with varying weight percentages (10-25 wt.%) of Ni on Cu were prepared using this electroless method. The samples were annealed to 1030°C in H_2/N_2 gas with a flow of 200 sccm. However, after the annealing procedure the samples became very porous. Upon further investigation using XPS, there was up to 10 wt.% of phosphorous deposited in the Ni coating with the electroless method. The material safety data sheet of the electroless plating solution revealed a presence of phosphorous in the solution. Phosphorous was also involved in the alloying process creating a Cu-Ni-P complex alloy, and during the alloying process, phosphorous evaporated leading to porous samples . Therefore, this method was deemed unsuitable for preparing CuNi alloys and was abandoned. Instead, electroplating of Ni on Cu was utilized for preparing the CuNi alloys.

A surface preparation technique different from the method described above was developed and resulted in controlled Ni electroplating of Cu foils. The new process involved using electroplating and thermal annealing of the electroplated foils to prepare the Cu-Ni isomorphous alloys. Specifically, the work involves preparation of Cu-rich ($Cu_{1-x}Ni_x$) and Ni-rich ($Ni_{1-x}Cu_x$) alloys, two different electroplating techniques have been used to quicken the alloy preparation. For Cu-rich (CuNi) alloys, Ni electroplating of Cu is used. For Ni-rich (NiCu) alloys, Cu electroplating of Ni was used. The details of the Cu-based (CuNi) and Ni-based (NiCu) alloy preparation procedure is discussed in the subsequent subsections.

3.5 Preparation of CuNi alloys

Cu-rich (CuNi) alloys were prepared by electroplating Ni on Cu foils and then thermally annealed at 1030°C in reduction environment (H_2/N_2 flow at 200 sccm) to induce diffusion of Cu and Ni atoms for >5 hours and to remove the native oxide on the metal surface. The low purity Cu foils (99.98% pure), which were purchased from Alfa Aesar, were cut into smaller pieces $\approx$35 mm $\times$ 35 mm size. The mass of each of these pieces of Cu foil is recorded before Ni electroplating. The Cu foils were cleaned with Acetone and Isopropyl Alcohol (IPA) and dipped in 50% diluted (by volume) hydrochloric acid (HCl) for 2 minutes to remove stray metallic contaminants. The Cu foils were then mounted on Teflon sheet similar to the electropolishing setup

(Figure 3.3b). A two-electrode setup is used where a Ni foil (99.98% pure) acts as an anode and the cleaned Cu foils act as a cathode. The Ni electroplating setup is schematically illustrated in Figure 3.4. A Transene Watts bath ($NiSO_4 \cdot 6\,H_2O$ + $NiCl_2 \cdot 6H2O$ + H_3BO_3; 200 g/L + 100 g/L + 45 g/L, respectively) is used as an electrolyte [201, 203, 204]. A Gamry Reference 3000 potentiostat is used for monitoring the voltage change during Ni electroplating and apply constant current over a very specific time. A constant current density of 0.19 A/cm^2 is applied to the electrodes using an electrochemical technique, chronopotentiometry, while recording applied potential and time. The electroplating run varied for each, and the average electroplating time for each weight percent is provided in the Table 3.1.

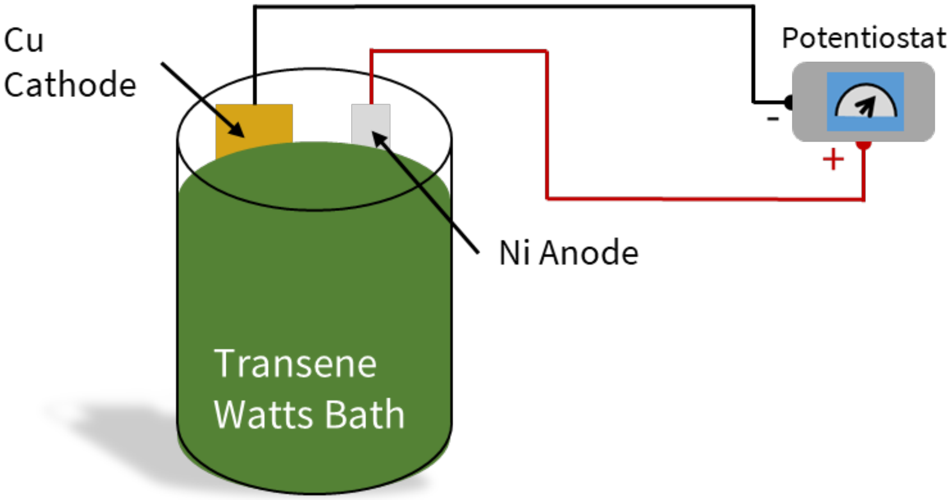

Figure 3.4: Setup for Ni electroplating. The two-electrode setup consists of Cu cathode and Ni anode with a commercial Transene Watts bath used an electrolyte.

Table 3.1: Ni weight percent and average deposition time.

Ni weight percent (wt. %)	Average deposition time (in mins)
10 wt. %	18
20 wt. %	27
30 wt. %	57
40 wt. %	80
50 wt. %	130

Figure 3.5 shows the Ni electroplated Cu foils before thermal annealing process. The weight of the Cu foils is measured before and after Ni electroplating. The Ni weight percent on Cu is calculated using the relationship below:

$$wt.\% = \frac{Wt_{after} - Wt_{before}}{\text{Total weight of plated foil}} \times 100 \tag{3.1}$$

where Wt_{after} is the weight of the foil after Ni electroplating, Wt_{before} is the weight of foil before Ni electroplating and the total weight of the plated foil, which is the same as weight of electroplated foil.

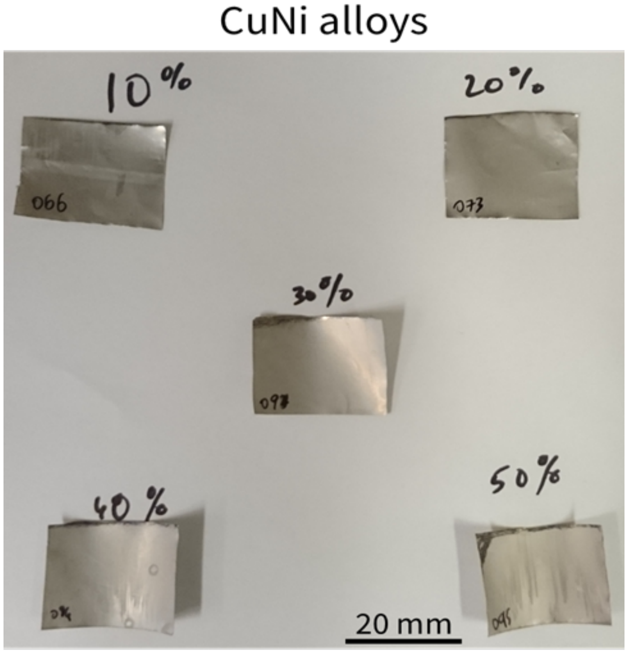

Figure 3.5: Ni electroplated Cu foils of various weight percentages before thermal annealing.

Various weight percentages (Table 3.2), ranging from 10 wt.% to 50 wt.% of Ni were deposited on Cu using this technique. After electroplating Ni on several Cu samples, only samples that were within ±1 wt.% of the desired wt.% were used for alloying. The alloying of these Ni electroplated Cu foils takes place in a reduction environment with a $\approx$200 sccm flow of H_2/N_2 gas at 1030°C for >5 hours. The weight of the alloyed foils was measured before and after alloying to ensure the weight has not changed. None of the samples showed a weight change after alloying. Table 3.2 shows the alloy compositions (wt.%) that were prepared using this method for the study and the naming convention that was used throughout this study.

Table 3.2: Table of all the Cu-rich alloys used for this work.

Alloy composition ($Cu_{1-x}Ni_x$)	Naming convention ($CuNi_x$)
$Cu_{90}Ni_{10}$	CuNi10
$Cu_{80}Ni_{20}$	CuNi20
$Cu_{70}Ni_{30}$	CuNi30
$Cu_{60}Ni_{40}$	CuNi40
$Cu_{50}Ni_{50}$	CuNi50

3.6 Preparation of NiCu alloys

Ni-rich (NiCu) alloys were prepared by electroplating Cu on Ni foils and then thermally annealed in reduction environment similar to CuNi alloys. The Ni foils (99.8% purity), which were purchased from Alfa Aesar, were cut into smaller pieces of ≈30 mm × 25 mm and rinsed off with Acetone and IPA. The foils were then mounted on a Teflon sheet, which was then put into the electroplating bath; the setup, which is similar to Ni electroplating, is shown in Figure 3.6. Electroplating Cu on Ni takes place in a bath composed of 0.15 M of $CuSO_4$ and 1 M of H_2SO_4. In this two-electrode setup, Ni is the cathode (working electrode) and low purity Cu (99.98%) is the anode (counter electrode). A reference electrode is not utilized throughout the course of the work for Cu electroplating.

A Gamry Reference 3000 potentiostat is used to apply a constant current (chronopotentiometric mode) and monitor the voltage changes over time. The electroplating current density is kept constant at 40 mA/cm^2. After numerous trials with different current densities, a value of 40 mA/cm^2 was used, which gave a visually smoother electroplating finish. The optimum time varied for each run, and therefore, average electroplating time for each weight percent is provided in the Table 3.3. By varying the electroplating time, different weight percentages of Ni foils were electroplated with Cu as listed in Table 3.4.

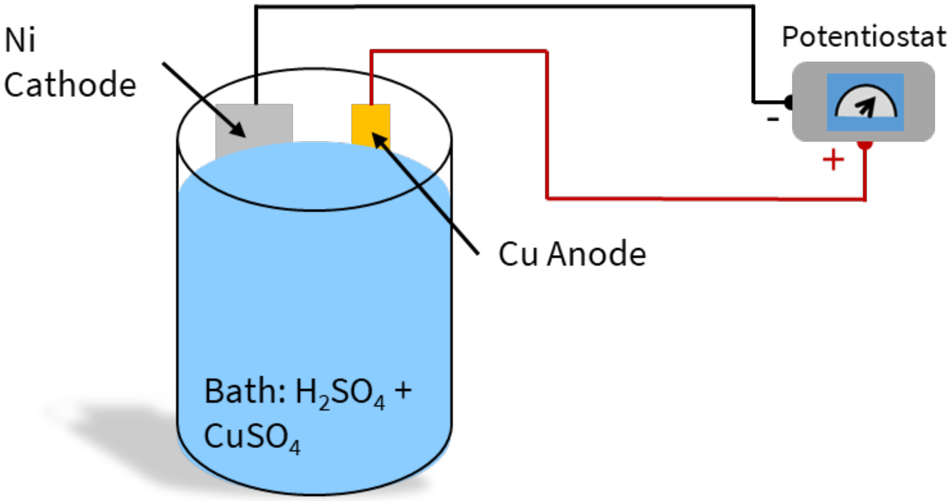

Figure 3.6: Setup for Cu electroplating. The two-electrode setup consists of Cu anode and Ni cathode. The electrolyte bath is composed of 1 M H_2SO_4 and 0.3 M of $CuSO_4$.

Table 3.3: Cu weight percent and average deposition time.

Ni weight percent (wt.%)	Average deposition time (in mins)
10 wt.%	26
20 wt.%	46
30 wt.%	75
40 wt.%	105
50 wt.%	125

The weight of the Ni foils was measured before and after electroplating to determine the weight of Cu deposited. The weight percentage of Cu on Ni is then calculated using the relationship:

$$wt.\% = \frac{Wt_{after} - Wt_{before}}{\text{Total weight of plated foil}} \times 100 \tag{3.2}$$

where Wt_{after} is the weight of the foil after Cu electroplating, Wt_{before} is the weight of foil before Cu electroplating and the total weight of the plated foil is the same as Wt_{after}. Figure 3.7 shows the Cu electroplated Ni foils before alloying them during thermal annealing process.

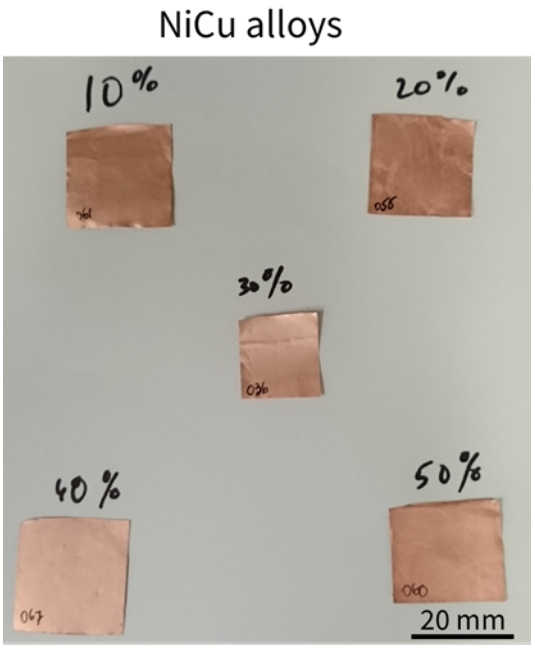

Figure 3.7: Cu electroplated Ni foils of various weight percentages before thermal annealing.

Only the electroplated Ni foils with Cu weight percentages within $\pm$1 wt.% were used to prepare NiCu alloys. After careful selection of these electroplated foils, they were thermally annealed in reduction environment with H_2/N_2 gas flowing at $\approx$200 sccm at 1030°C for >5 hours. The foil weight was measured before and after thermal annealing to ensure no weight change. None of the samples showed a weight changed after alloying. Table 3.4 shows the various NiCu alloy compositions that were prepared and the naming convention that was used throughout this study.

Table 3.4: Table of all the Ni-rich alloys used for this work.

Alloy composition ($Ni_{1-x}Cu_x$)	Naming convention ($NiCu_x$)
$Ni_{90}Cu_{10}$	NiCu10
$Ni_{80}Cu_{20}$	NiCu20
$Ni_{70}Cu_{30}$	NiCu30
$Ni_{60}Cu_{40}$	NiCu40
$Ni_{50}Cu_{50}$	NiCu50

3.7 Mechanical polishing of alloys

Electropolishing using the recipe created for Cu (as was described in Section 3.2) was used to prepare the surface of alloys samples. However, electropolishing led to selective etching of Cu in both the CuNi and NiCu foils. The technique was abandoned. Instead mechanical polishing was chosen as it was shown that mechanical polishing does not preferentially etch Cu or Ni species in the alloy samples like electropolishing [202,205] and allows to prepare smooth surface of the alloyed foils. After the alloying process, both CuNi and NiCu foils were cut into smaller ≈6 mm × 6 mm in a trapezoidal shape, similar to Cu samples. The corners of the trapezoidal-shaped samples were cut to be able to distinguish the alloy composition with a naked eye. The shapes of the CuNi and NiCu alloyed foils are shown in Figure 3.8.

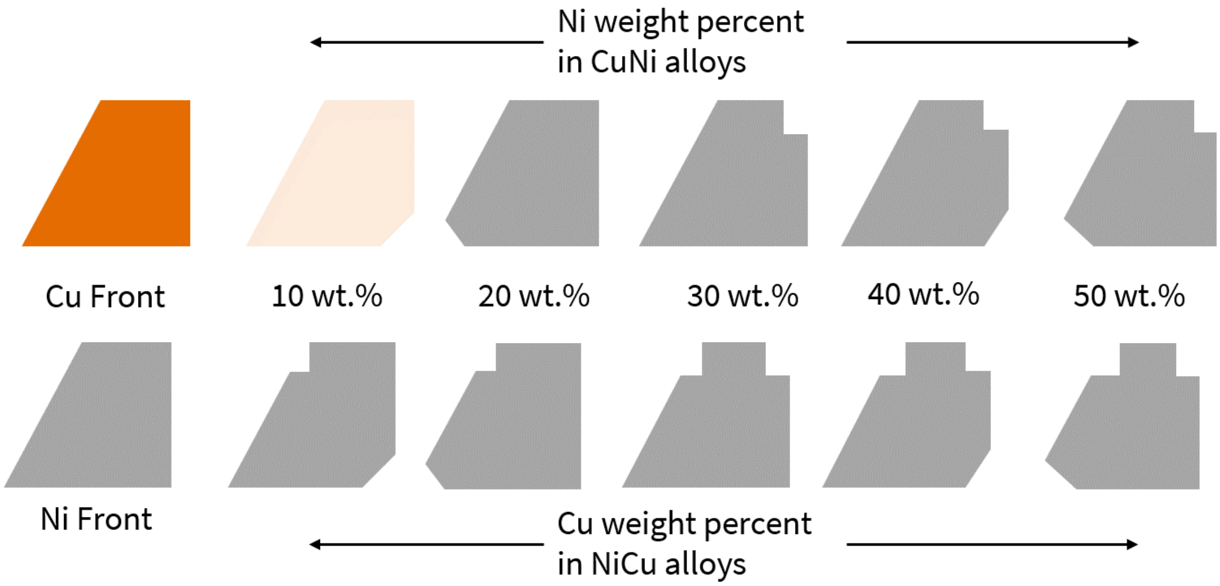

Figure 3.8: Sample shapes of Cu and the alloys. The cuts indicate the specific composition of the alloy sample.

The cut samples were pressed using a hydraulic press (≈0.35 GPa) to flatten the samples and to induce plastic deformation. The flattened samples were then mounted on a double-sided scotch tape and attached on a metal chuck as shown in Figure 3.9. Numerous chucks were used depending on the number of samples. Generally, 10 and 20 wt.% of CuNi and NiCu and 30-50 wt.% of CuNi and NiCu were placed on separate chucks. A Buehler Vibromat vibratory polisher was used for mechanical polishing. A slurry (details below) was prepared and dispersed into the vibratory polisher after a fresh polishing pad (Allied High Tech) was placed. The metal chucks with the CuNi and NiCu samples mounted were then inserted into the slurry and the polishing procedure was started.

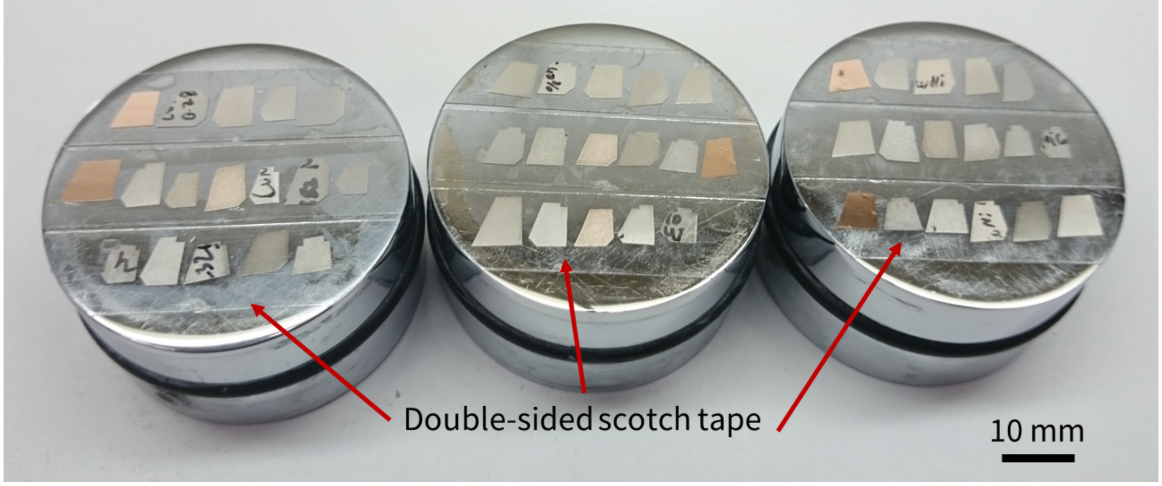

Figure 3.9: CuNi and NiCu samples mounted on metal chucks for mechanical polishing. A double-sided scotch tape is used to hold the samples to the metal chuck.

Three different slurries were used with varying results: a colloidal Silica slurry (0.05 µm) had a pH of $\approx$8-9 and led to mild corrosion on the edges of the samples; Diamond nanoparticle slurry (1 µm and 0.05 µm) was too hard and would embed itself into the alloy; an agglomerated α-Al_2O_3 (1 µm) was better of the three, but would occasionally embed itself as lumps into the sample. To ensure both grinding and polishing of the sample surface took place, two different polishing steps were used to qualitatively attain a very smooth surface finish.

For the grinding step, a 1 µm deagglomerated α-Al_2O_3 powder (Allied High-Tech Products) of $\approx$50 g was poured into the fresh clean polishing pad. DI water was then poured into the polishing pad and the polisher was set to 100% vibrating intensity until the alumina powder was completely dispersed. Then, the metal chucks were placed onto the polishing pads at 30% vibrating intensity and polished for 10-16 hours. The quality of the grinding step was assessed every two hours using a metallurgical optical microscope with Nomarski. When the samples appeared smooth, the final polishing step was used to further polish the surface. For the final polishing step, a 0.050 µm deagglomerated α-Al_2O_3 powder (Allied High-Tech Products) with DI water was used as a slurry and prepared similar to the grinding slurry. After the grinding step, the samples were transferred into the polishing slurry and were set to be polished for 2-3 days at 30% vibrating intensity. The samples were examined every 3-4 hours to assess the polishing quality. Figure 3.10 shows samples while still mounted on the polishing chuck before removal.

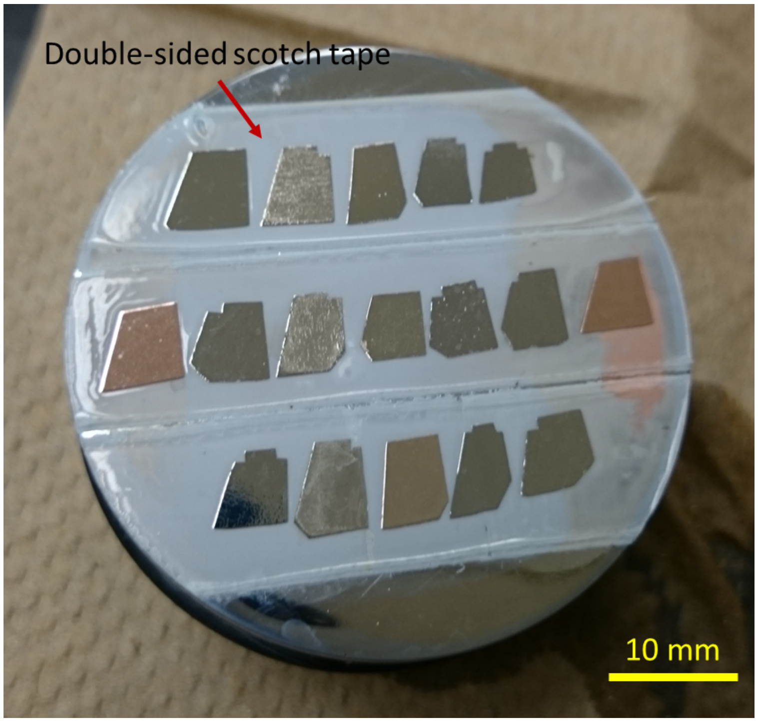

Figure 3.10: Polished alloy samples mounted on polishing chuck before removal.

After the samples were polished, IPA was sprayed onto the samples while they were on the polishing chuck and soaked for about 30 secs. A blade was used to gently dislodge the samples from the double-sided scotch tape in a slicing action, while IPA was still on the tape. After all the samples were dislodged, they were ultrasonicated with Acetone and IPA for 10 minutes in each solvent. The cleaning procedure was repeated twice to ensure complete removal of residual scotch tape glue. DI water was not used in the rinsing step as some of the samples corroded in several days after water rinsing. The samples were then dried by blowing nitrogen to remove the residual IPA. The samples were placed in a plastic container and stored in a nitrogen storage cabinet.

3.8 h-BN growth on metal substrates

Following the surface preparation of the Cu and alloys, the samples were placed in a pyrolitic boron nitride (PBN) crucible for h-BN growth on Cu (Figure 3.11a) and alloyed samples (Figure 3.11b). The crucible with multiple samples is loaded into the home-built vertical APCVD reactor and pumped down to a pressure of 10^{-2} Torr (Figure 3.12). The vertical reactor enables h-BN growth on several samples in the same growth run.

The samples were thermally annealed in a reducing environment at 1030°C under a flow of 180 standard cm^3 min^{-1} (sccm) of N_2 and 20 sccm of H_2 for $\approx$5 hours to remove native oxide from the surface and to cause the Cu grain recrystallization. h-BN is then grown in atmospheric pressure (1.1 PSIG) using ammonia borane (H_3NBH_3, BoroScience International, Inc. 99.9% purity) as a precursor. The precursor is sublimated upstream at temperatures of 60-90°C and transported by 1.1 PSIG (816 Torr) of a carrier gas (mixture of 840 sccm of N_2 and 20 sccm of H_2) to the reactor. Different growth times were used for the following studies: 1) For h-BN morphology studies, h-BN was grown for 30 mins with a carrier gas flow rate of 850 sccm. 2) For electropolishing studies, h-BN was grown for 20 mins with a flow rate of 850 sccm. 3) For h-BN growth dependency on Cu microstructure studies, a growth time of 20 mins with a flow rate of 960 sccm was used. 4) For h-BN growth on alloys, a growth time of 60 mins with a flow rate of 740 sccm was used. After CVD growth, the samples were cooled down at $\approx$100°C/hr and removed from the furnace for further characterization.

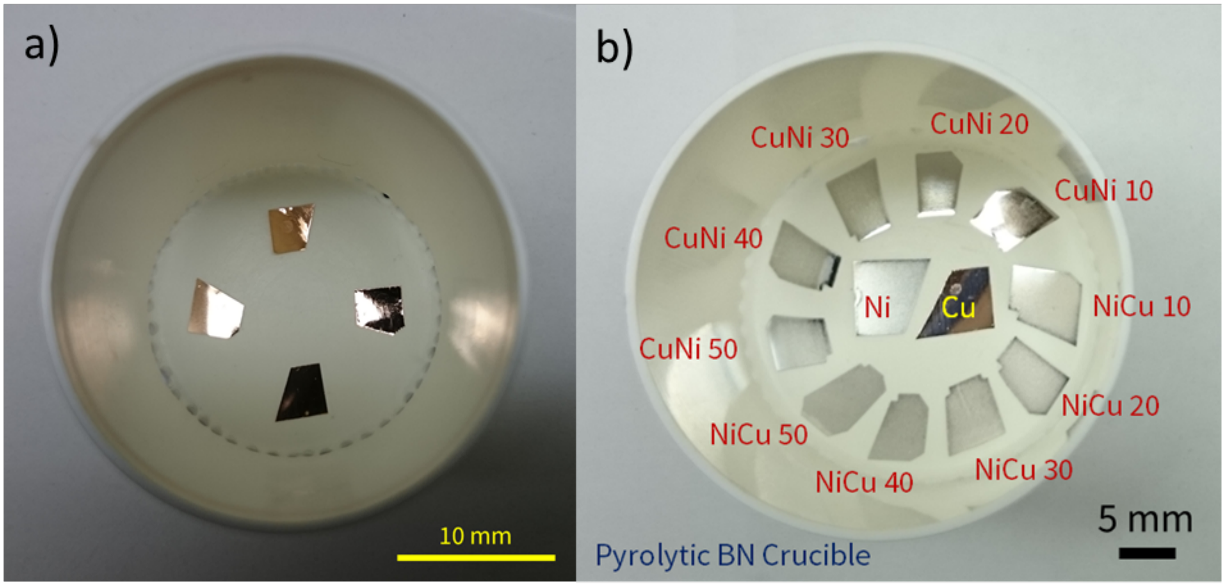

Figure 3.11: Sample placed in a pyrolytic BN crucible. a) Cu samples in the crucible before growth. b) Alloyed samples with control samples Ni and Cu in crucible before growth.

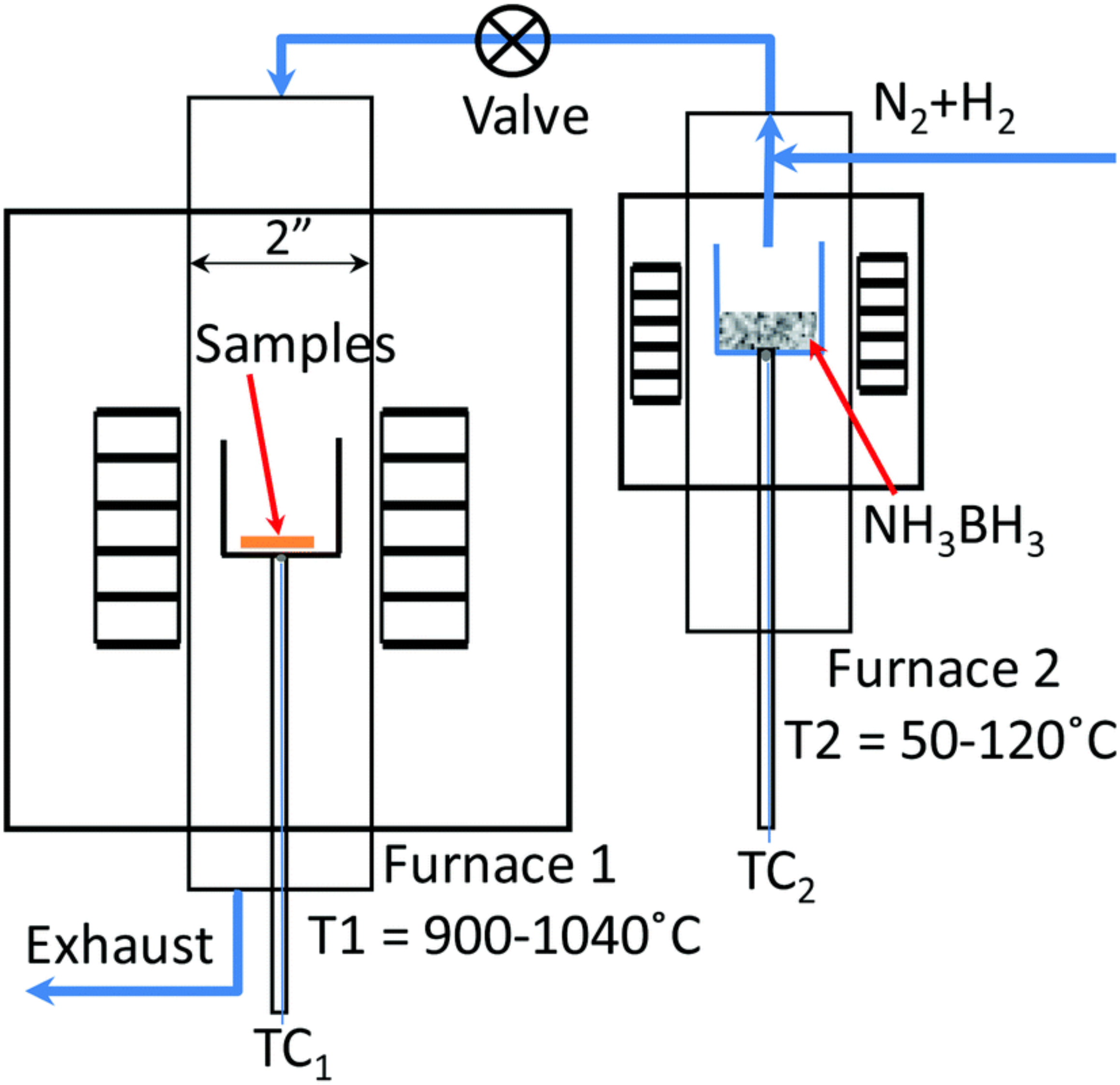

Figure 3.12: Vertical APCVD reactor for growing h-BN. Reprinted with permission from [67]. Copyright 2015 Royal Society of Chemistry.

3.9 Characterization conditions

The characterization conditions and methods employed to study the h-BN growth, Cu and Cu-Ni alloy substrates is as follows. Fourier transform infrared reflection absorption spectroscopy (FT-IRRAS) was used to confirm the growth of h-BN on Cu surface. A Thermo Scientific Nicolet 8700 spectrometer with a grazing-angle accessory from Harrick Scientific Products was used to perform FT-IRRAS. The incidence angle was 75°, and the spectra were obtained in p-polarization.

A liquid nitrogen cooled HgCdTe (MCT-B) detector was used and the data obtained was averaged over 1000 scans at 4 cm^{-1} resolution.

SEM was used to assess the lateral growth and nucleation density of h-BN on Cu. SEM was performed using a JEOL SEM with 5 keV accelerating voltage and 83 µA of probe current. All the SEM images were obtained in both in-lens and secondary electron modes.

Tapping mode AFM (Veeco D5000) with phase imaging was also performed directly on Cu foils after growth to confirm the thickness of h-BN and to assess the lateral sizes of h-BN crystals. An AFM tip (Budget Sensors Tap150-G) with a tip radius of <10 nm was used, and the AFM images were obtained with a scan rate of 1 Hz. Contact mode AFM (CM-AFM) was performed on Veeco D5000 with lateral force microscopy (LFM) enabled. The tips were obtained from Bruker (MSNL-10), which has several rectangular and triangular cantilevers. The 'F' triangular cantilever tip with a spring constant of 0.6 N/m was used for contact mode imaging.

STM was performed using a freshly cut tungsten (W) tip, which was etched in diluted nitric acid and hydrochloric acid to remove metal contaminants. The tip was finally rinsed off with acetone, isopropyl alcohol (IPA) and deionized (DI) water. STM was performed in room temperature on an Omicron Nanotechnology UHV-VT-STM with Nanonis SPM Controller. All the STM images were performed in constant voltage mode to ensure that the tip does not crash into the sample. To find the optimum potential that gives the best STM image, images were obtained at various voltages ranging from -4 V to 4 V at every 1 V step. A tip potential of -1 V was used, which had the least amount of noise in the image.

4. APCVD GROWTH OF H-BN ON POLYCRYSTALLINE CU SUBSTRATES

This section is divided into three subsections, which will discuss the growth morphology of h-BN on Cu, the effect of Cu surface preparation and the Cu grain orientation. The first subsection (Section 4.2) will discuss the growth morphology of h-BN on an unprepared polycrystalline Cu substrate and its assessment using scanning probe microscopy (SPM). The next subsection (section 4.3) explains the effect of Cu surface preparation technique, where the h-BN domain size increases, and the secondary nucleation on continuous h-BN films are minimized. Graphene is also grown on surface-prepared Cu as a testbed to demonstrate the benefits of Cu surface preparation. The last subsection (Section 4.4) explores the explores the dependency of Cu grain orientation on h-BN crystal nucleation density.

4.1 Introduction

Large-scale commercialization of 2D material devices relies on understanding the nature and growth morphology of CVD grown h-BN on polycrystalline Cu using various spectroscopic and electron microscopic techniques. The growth morphology encompasses crystal size, shape, and texture of h-BN on Cu. At the time of publication, there is limited literature on the morphology of CVD-grown h-BN on Cu [206, 207, 208, 209]. This work utilizes ultra-high vacuum STM, ambient AFM and SEM to assess the morphology of the CVD grown h-BN films to provide a preliminary insight into the growth mechanism and the influence of Cu substrate on h-BN growth. Since CVD growth of h-BN is self-limiting on Cu, the Cu surface features are expected to influence and potentially dominate the h-BN growth mechanisms. Hence, there is a need for ultra-smooth and morphologically homogenous starting Cu surface to allow for deliberate control of h-BN crystal quality. Additionally, as the growth of h-BN takes place on polycrystalline Cu, the impacts of polycrystalline Cu grain orientation on h-BN is also studied.

4.2 Growth morphology of h-BN on Cu

4.2.1 FT-IRRAS characterization of h-BN

FT-IRRAS is used to confirm the growth of h-BN on Cu [67, 68, 69] by using the characteristic vibrational modes of h-BN. Figure 4.1a shows a typical FT-IRRAS spectrum of h-BN on a Cu foil substrate, which shows the position of primary vibrational modes [67]. Only the out-of-plane A$_{2u}$ (LO) IR-active vibrational modes can be observed using FT-IRRAS (Figure 4.1a). The in-plane vibrational modes, E$_{1u}$ (TO) at 1368 cm^{-1} and E$_{1u}$ (LO) at 1610 cm^{-1} are IR-active modes, which measure extremely weakly on FT-IRRAS. The Raman peak of h-BN E$_{2g}$ (TO) at 1368 cm^{-1} is also weak, Raman spectroscopy is not a technique of choice used for rapid confirmation of h-BN films (1-2 monolayers) grown on metal substrates [67, 210].

As the A$_{2u}$ peak (823 cm^{-1}) is the most active peak of h-BN, higher resolution scans were collected to differentiate h-BN growth on various samples (Figure 4.1b). The A$_{2u}$ peak can shift depending on the interaction with the substrate (Figure 4.1b) for both polycrystalline Cu and Ni samples, shown from the same growth run [67]. Both the Cu and Ni samples exhibit the A$_{2u}$(LO)1 (819 cm^{-1} for Cu and 815 cm^{-1} for Ni) and A$_{2u}$(LO)2 (823 cm^{-1}) bands, where A$_{2u}$(LO)1 indicates regions in the sample with stronger h-BN-substrate interaction (Figure 4.1b). The results (Figure 4.1b) also show that Ni substrate induces stronger h-BN coupling to the substrate than Cu, which can be inferred from the lower wavenumber (815 cm^{-1}) on Ni substrate in comparison to Cu (818.3 cm^{-1}) [67, 158, 211]. The A$_{2u}$(LO)2 peak indicates presence of the h-BN regions with weaker substrate interaction and appear at a similar wavenumber for both Cu and Ni.

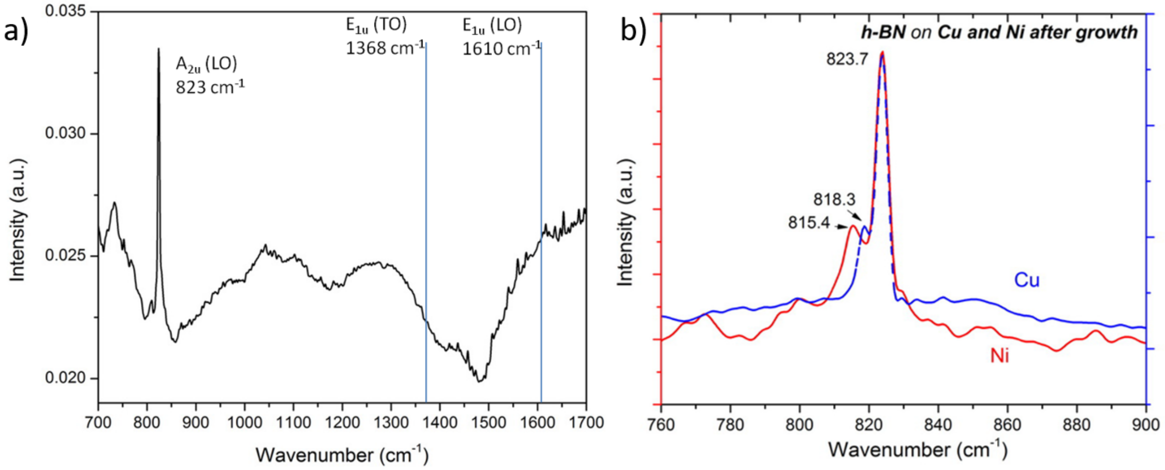

Figure 4.1: a) Typical FT-IRRAS spectrum for a 2D h-BN film on Cu [67], b) Representative spectra of different alternatives found within FT-IRRAS of 2D h-BN film on Cu and Ni for A$_{2u}$ (LO) vibration with two sub-bands: A$_{2u}$(LO)1 and A$_{2u}$(LO)2. (a-b) Reprinted with permission from [67]. Copyright 2015 Royal Society of Chemistry.

4.2.2 SEM characterization of h-BN

SEM shows any structural abnormalities in h-BN crystal or film that indicate suboptimal growth conditions, thus lending itself as a reliable technique to assess the h-BN nucleation density, distribution and film morphology. There are two primary crystal shapes of h-BN: triangular and hexagonal (Figure 4.2). The triangular crystal shape is an indication of N-termination at the h-BN crystal edge, while the hexagonal shape indicates B-termination at the edges [57, 157]. The N-termination is thermodynamically more favorable and stable h-BN crystal shape, and B-termination indicates a metastable h-BN shape. Other, less defined, crystal shapes such as “star-shaped” (Figure 4.2a) and poorly defined rhombohedrals are also present, and is considered as an extension of the triangular shape [57, 157]. Any crystal shape other than triangular indicates non-uniform growth rates on the edges of h-BN crystal, leading to anomalous crystal shapes (Figure 4.2c and 4.2d) [57, 157] that are sub-optimal for monolayer growth. The SEM micrographs also show that h-BN nucleation occurrs frequently from a site at the center of the h-BN crystal similar to graphene [212]. The potential nucleation site (Figure 4.2a) can also be observed in Figure 4.2d.

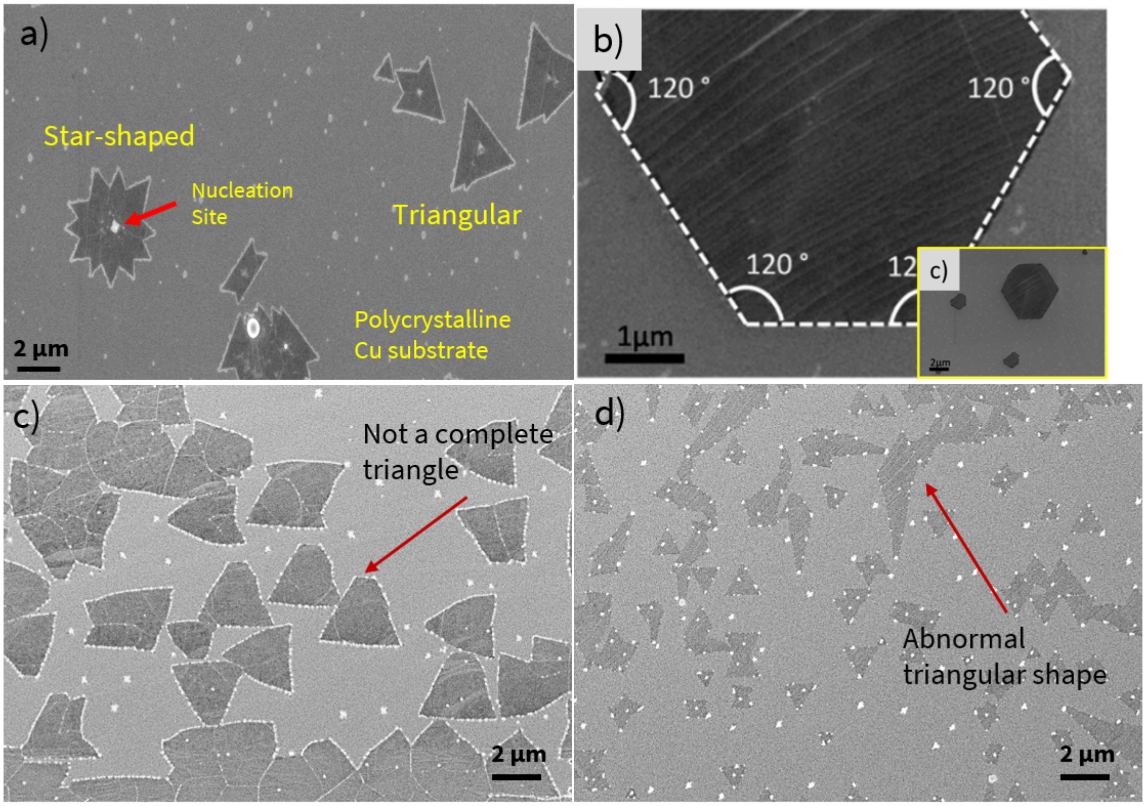

Figure 4.2: SEM micrographs of various h-BN crystal shapes formed using CVD. a) Star-shaped and triangular shaped are indicated, b) hexagonal shaped h-BN crystal [66], c) and d) h-BN crystals grown in sub-optimal conditions. (b) Reprinted with permission from [66]. Copyright 2014 American Chemical Society.

4.2.3 Characterization of h-BN morphology on Cu using scanning probe microscopy

Scanning probe microscopy (SPM) techniques, AFM (Tapping and Contact mode), and STM is used to further assess the h-BN crystal and film morphology on Cu. Tapping Mode AFM (TM-AFM), with phase imaging enabled, probe the surface topography of h-BN films grown on Cu at two different scan sizes: 10 µm × 10 µm and 5 µm × 5 µm (Figure 4.3). One of the key expectations of h-BN is to have a smooth topography with low surface roughness that will act as an excellent substrate to grow other 2D materials such as graphene and h-BN. However, from the topographic AFM scans (Figures 4.3a and 4.3c), the surface is observed to be extremely corrugated with ridge-like features. Phase imaging provides information on the surface adhesion due to changes in material composition [213], and it confirms that the topography is not an artifact (Figures 4.3b and 4.3d). Although the figures do not explicitly distinguish between material composition, they reveal the variation in phase arising from ridges (Figure 4.3d) as ascribed to the ridged nature of the h-BN on Cu.

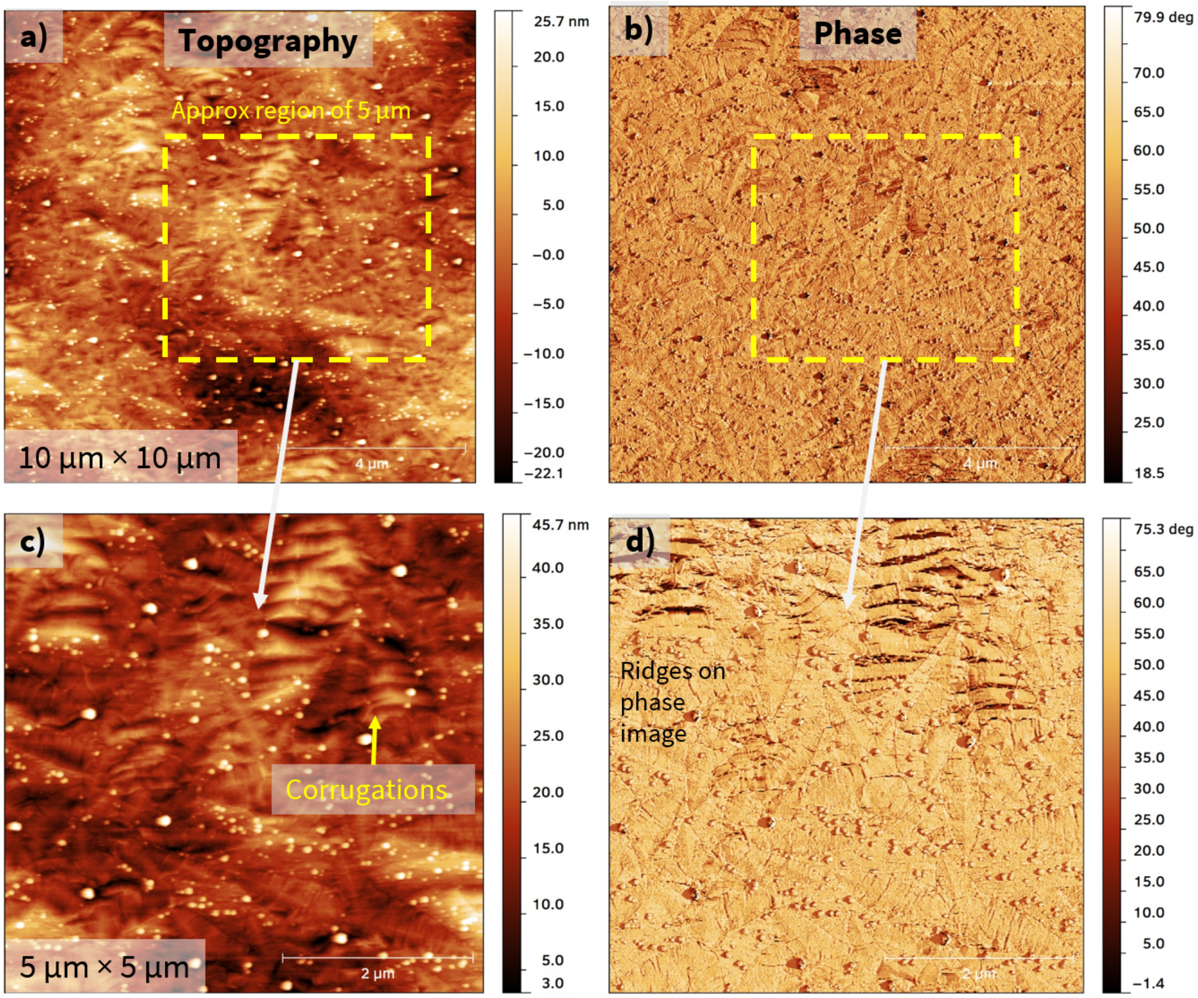

Figure 4.3: a and b) Tapping mode AFM images of h-BN film on polycrystalline Cu using topography and phase imaging modes, respectively. c and d) enlarged images of the topography and phase imaging modes shown in images a and b, respectively.

A TM-AFM scan of higher magnification quantified the variation in the ridges on the surface to better resolve these features. A 2 µm × 2 µm AFM scan with the same tip velocity on the same region as Figure 4.3c shows much better resolution of the ridged features (Figure 4.4a). The ubiquitous bright white spots in Figure 4.4a are confirmed to be the nucleation sites. Although not much additional information is deduced from the phase image (Figure 4.4b), it still illustrates inhomogeneities on the sample that a phase change indicates. Figure 4.4c provides a three-dimensional representation of topography image from Figure 4.4a. The topographical scan provides three height profiles: vertical, horizontal and diagonal (Figure 4.4d, 4.4e, and 4.4f, respectively). The height profiles show variations of $\approx$12 nm on nearly all the samples. While, there is convincing evidence that the ridges or corrugations are real, the source of corrugations remain unclear.

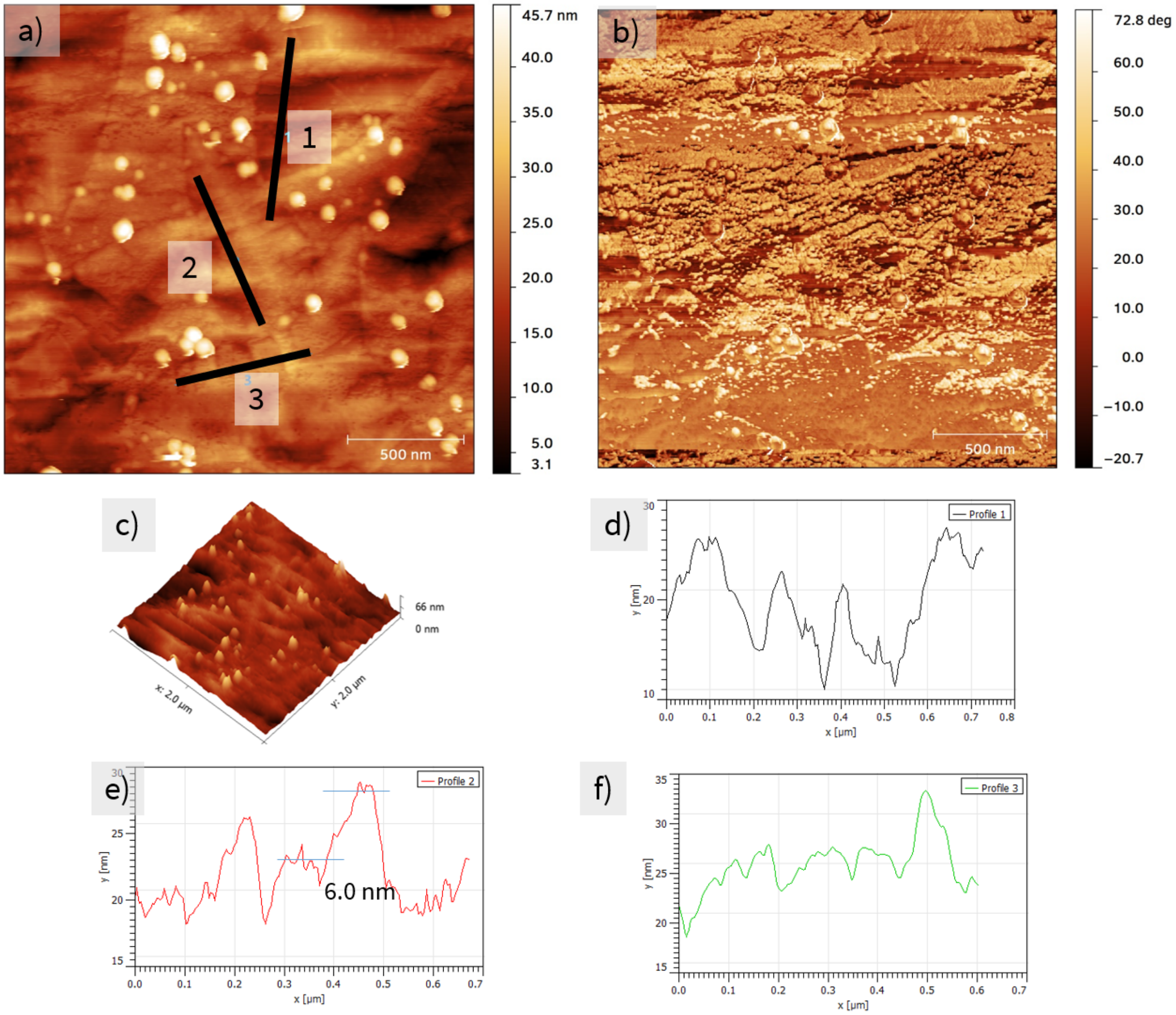

Figure 4.4: Tapping mode AFM and height profiles of a smaller (2 µm × 2 µm) scan of Figure 4.3c. a) Topography and b) Phase image, c) 3D image of topography, d) height profile of 1, e) height profile of 2, f) height profile of 3.

As these corrugations appear in both topography and phase image on a complete h-BN film, contact mode AFM (CM-AFM) of h-BN crystals on Cu is performed to assess the topography of h-BN and Cu after growth. A soft AFM cantilever probe in CM-AFM is brought into the repulsive regime of the surface to increase the resolution of the topographical features [213] and to ensure the tip does not damage or distort the topography of h-BN on Cu. CM-AFM also has a secondary imaging mode known as lateral force microscopy (LFM) or frictional force AFM, which provides the variation in friction of h-BN and Cu surfaces.

Figure 4.5 shows a summary of CM-AFM results of h-BN crystals on Cu. Triangular-shaped h-BN crystals are clearly found in both topography and friction images (Figure 4.5a and 4.5b, respectively). The topographical features, mainly the height and the presence of corrugations, are consistent with those observed for the same sample using tapping mode AFM (Figures 4.3 and 4.4). However, LFM resolved the corrugations in much greater detail, appearing to be unidirectional irrespective of the h-BN crystal orientation. The height profiles are consistent with values obtained using tapping mode AFM for both the horizontal and vertical profiles on Cu and h-BN.

The line profiles of h-BN on Cu (Figure 4.5a) are much more well resolved on contact mode AFM than on tapping mode AFM (Figure 4.4a). There is a noticeable difference in the variations of height on h-BN on Cu and Cu substrate; Cu appears to have lower peak-to-peak variations in the line profile than h-BN indicating that Cu has greater smoothness. The frictional force signal showed a greater than 2 × difference in friction between h-BN and Cu, 20 mV and 8 mV, respectively. The AFM results, both TM-AFM and CM-AFM, raise an important question whether h-BN is exhibiting corrugation because it is reflecting the Cu surface, or it forms ripples on a smooth Cu surface?

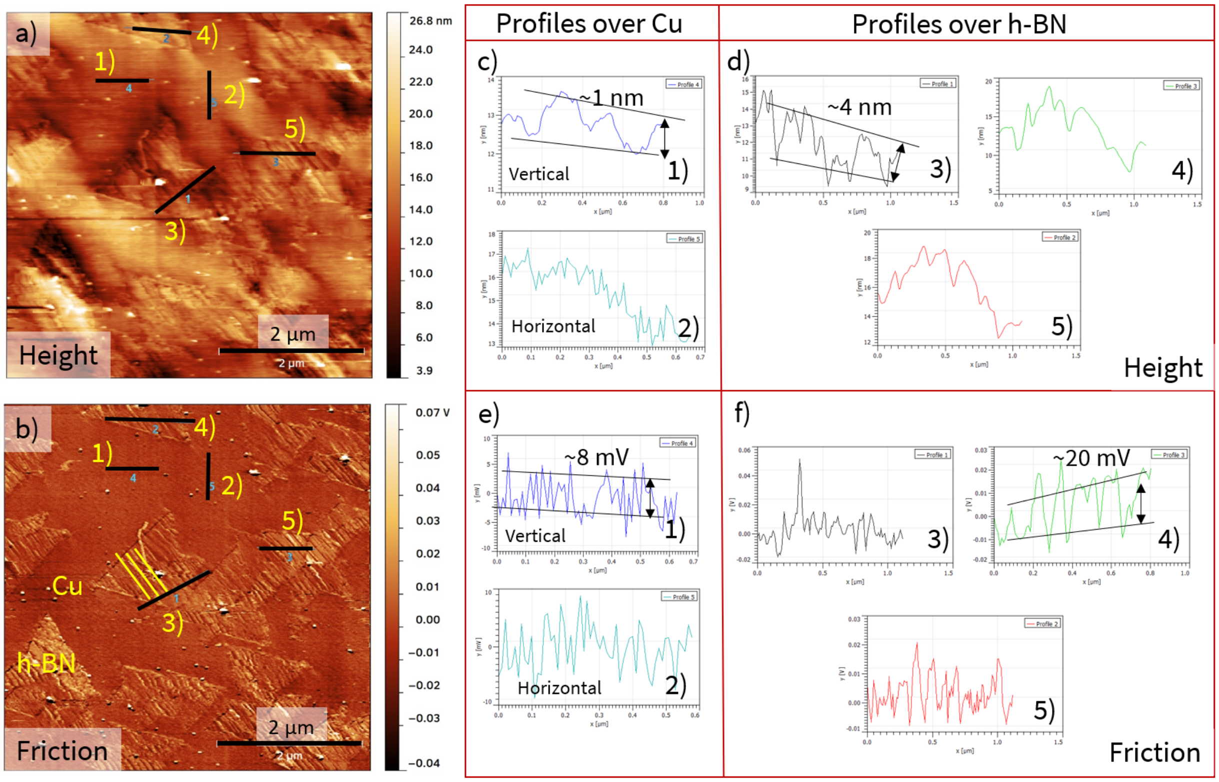

Figure 4.5: Contact mode AFM images of h-BN crystals on Cu, a) Height image and b) Friction image. The line profiles on Cu and h-BN for height are shown in c) and d), respectively. The line profiles on Cu and h-BN for friction are shown in e) and f), respectively.

Both TM-AFM and CM-AFM imaging are performed at room temperature in ambient pressure conditions. These conditions lead to water meniscus forming at the tip [214], which reduces the resolution of AFM images, and the subtleties of the corrugations cannot be well understood. To mitigate ambient effects and confirm the findings from CM-AFM, ultrahigh vacuum (UHV) scanning tunneling microscopy (STM) is performed. Figure 4.6 shows a summary of STM images of the same h-BN crystal on Cu at various probe potentials. Since the h-BN crystal appears well resolved and with -1 V probe potential showing low susceptibility to noise, a tip potential of -1 V is used for subsequent STM.

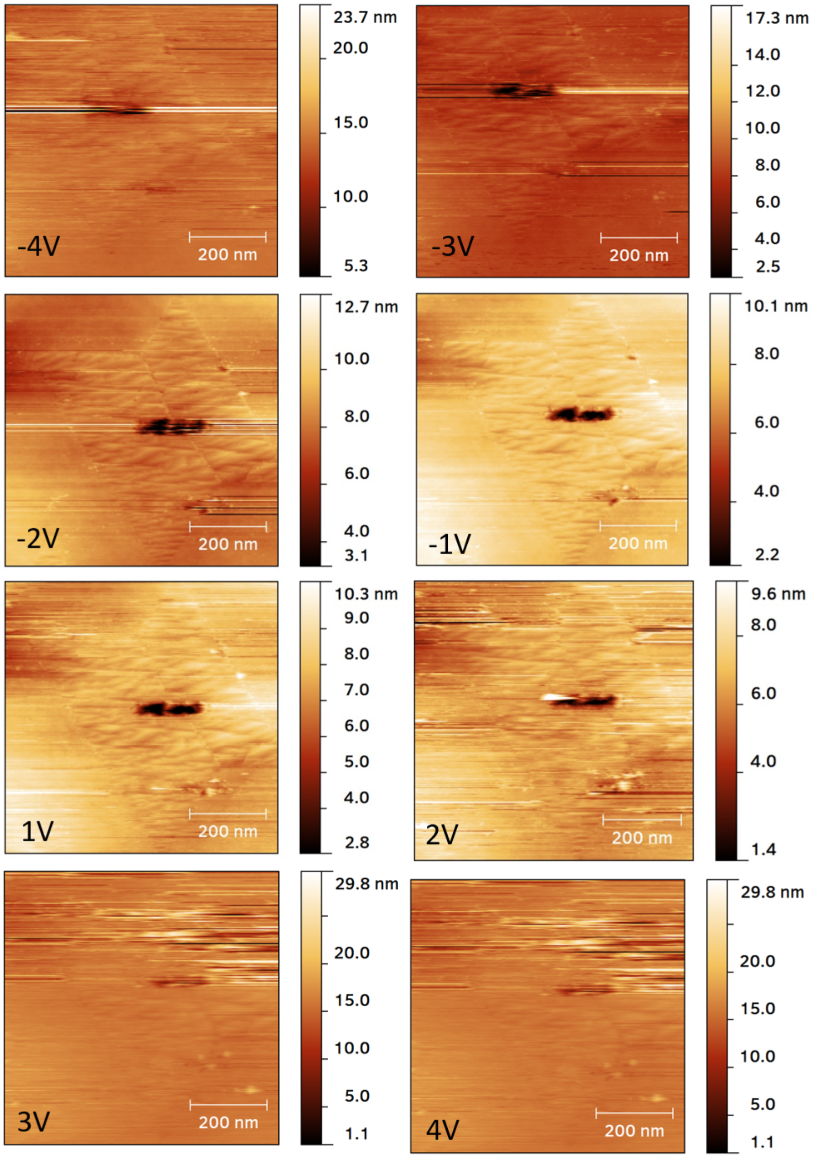

Figure 4.6: STM images of h-BN crystal on Cu taken at various tip potentials.

STM images are obtained at -1 V across various regions until an isolated h-BN crystal can be found. Smaller 500 nm × 500 nm STM scans at both 0°and 90°scan angles (Figure 4.7a and 4.7b, respectively) confirm that the corrugations on h-BN are real and not artifacts. These results are also in congruence with the TM-AFM and CM-AFM results. However, the Cu surface appeared comparatively smoother than h-BN (Figure 4.7c) in the 3D representation of STM image at 90°scan angle. As discussed previously, this raises two possible scenarios for the corrugations of h-BN: i) folds in the h-BN crystal due to reflections of Cu surface (Figure 4.7d), or ii) due to difference in thermal expansion of h-BN and Cu (Figure 4.7e). As the corrugations on both the scan angles are identical, this effectively ruled out the case where h-BN is free-floating (Figure 4.7d), as free-floating h-BN will be perturbed when an STM tip is scanned in very close quarters.

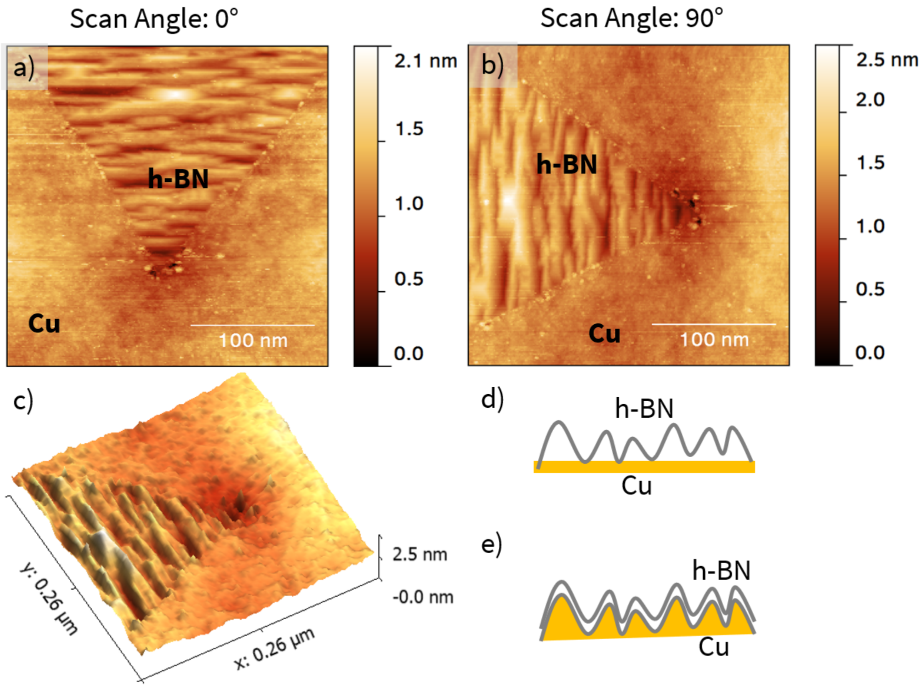

Figure 4.7: STM images of h-BN crystals on Cu at a) 0-degree scan angle and b) 90°scan angle, c) 3D image of 90°scan angle, d) Proposed schematic of h-BN independent of Cu surface profile, e) Proposed schematic of h-BN following Cu surface profile.

SEM, both in-lens and secondary electron mode, is used to assess the morphology of h-BN crystals on Cu. In-lens imaging is more sensitive to surfaces and therefore can resolve h-BN and Cu regions, which have different work functions. The secondary electron mode can provide topographical information of the same region. These two SEM imaging modes are used to correlate regions where h-BN crystals and Cu regions are present. Figure 4.8 shows SEM micrographs of h-BN crystals on Cu at various magnifications on a single Cu grain (Figure 4.8a-d) and across neighboring Cu grains (Figure 4.8e-f). The corrugations appeared only in the regions where h-BN crystal is located (Figure 4.8b and d). Corrugations in varying directions can be seen on h-BN crystals grown across neighboring Cu grains (Figure 4.8e-h). This indicates that the corrugations are a reflection of the Cu surface and corrugations appear only where h-BN crystal forms on the Cu surface.

In agreement with AFM and STM results, SEM micrographs reveal a smooth Cu surface wherever h-BN crystals are not present. The corrugations appeared only in the regions where h-BN crystal was located (Figure 4.8b and 4.8d). Leon et al also discussed the extremely low roughness of native oxide of Cu, where they reported a roughness of <1 nm using an AFM on a 700 nm $\times$ 700 nm scan [215]. Roos and Rauh reported a low surface roughness of Cu native oxide [216, 217], which was assessed using profilometric and ellipsometric methods. In comparison, the Cu roughness is $\approx$ 2-3 nm as obtained from AFM image on a 5 µm $\times$ 5 µm size from the AFM and STM characterization in this study. Additionally, Ibrahim et al also reported the observation of corrugated regions for graphene on Cu [218]. They also reported that graphene promotes reconstruction of Cu surface leading to step bunching, by preventing the evaporation and diffusion of Cu atoms. Hayashi et al also discussed corrugated nature or observance of step bunching on Cu surface after graphene growth [219].

As the h-BN growth mechanism is similar to graphene on Cu foil substrates, h-BN also promotes surface reconstruction of Cu surface. This means that h-BN is preserving the Cu surface morphology from native oxide formation on Cu surface thereby reflecting the corrugated Cu surface. The oxidation prevention property of h-BN was also reported for CVD-grown h-BN films in the literature [220, 221, 222]. The regions where no h-BN crystals are present on the Cu surface, the exposed Cu surface forms a native Cu oxide. This results in a smooth appearance of Cu surface and corrugations on h-BN when observed under STM and SEM.

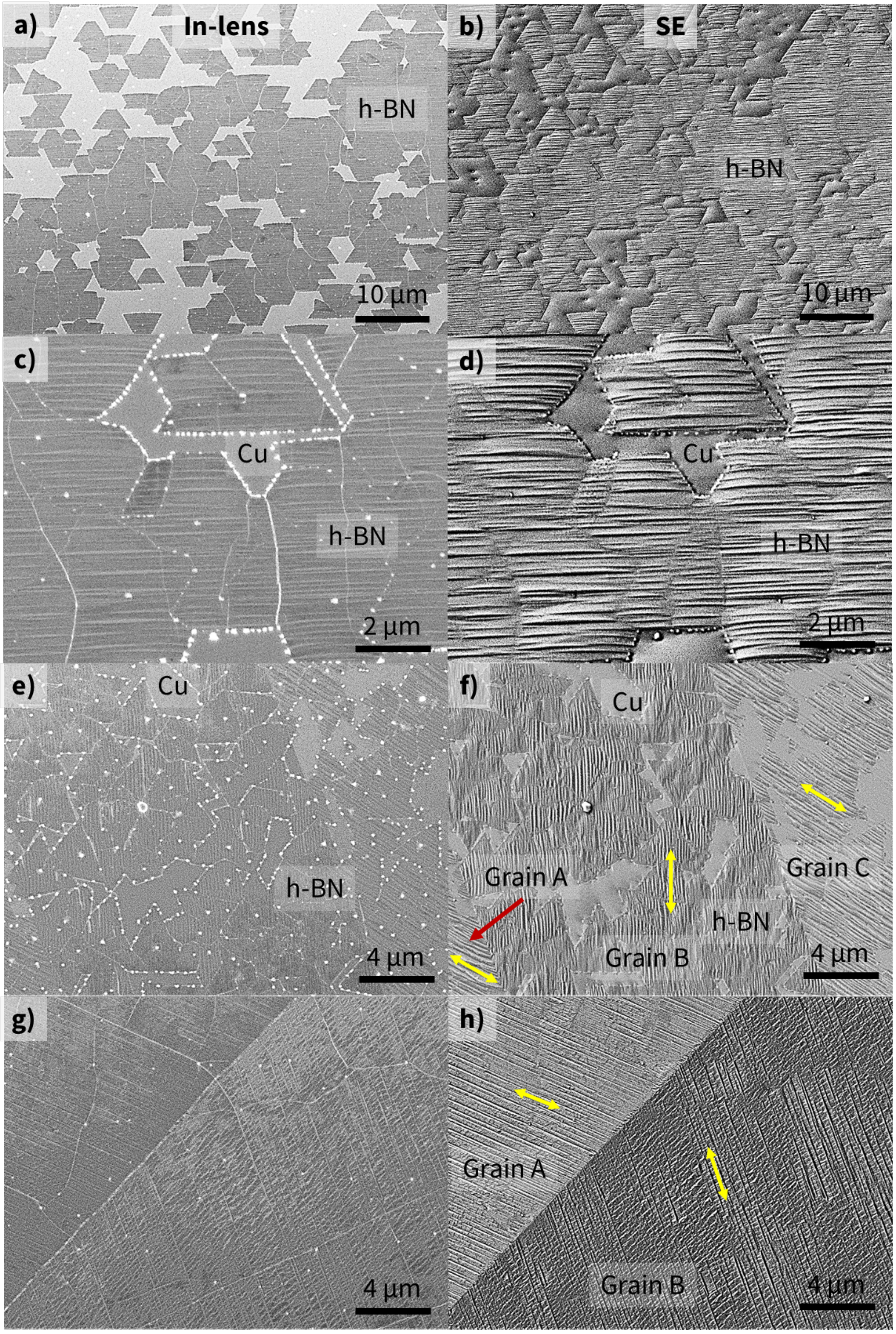

Figure 4.8: Tableau of SEM micrographs of h-BN crystals growing on Cu at two different magnifications: a) In-Lens detector at 2000X magnification, b) Secondary Electron detector at 2000X magnification, c) In-Lens detector at 10KX, d) Secondary Electron detector at 10kX magnification. Images (a-d) are from the same Cu grain. e) In-lens detector image at 5000X magnification, d) Secondary Electron detector at 10kX magnification, g) In-lens detector image at 5000X magnification, h) Secondary Electron detector at 10kX magnification. Images (e-h) are across neighboring Cu grains. The orientations of h-BN corrugations on each Cu grain is indicated in (f) and (h).

4.2.4 Coalescence of h-BN on Cu

A closer observation of the quasi-film of h-BN (Figure 4.8) reveals the polycrystalline grain boundary of the h-BN film, indicated by the bright white outline at the edges of the h-BN grain. STM is performed on neighboring h-BN crystals to assess the coalescence of h-BN. STM offers a much higher resolution than TM-AFM and CM-AFM because the resolution of these modes are limited by the tip radius [213] and the resolution can deteriorate further because of water meniscus on the tip [214]. STM images reveals the variations in crystal merging at the nanoscale (1-10 nm) level (Figure 4.9). Two different neightboring h-BN crystals are imaged with a scan size of 1 µm and 2 µm (Figure 4.9a and 4.9b) and their topographical profiles are shown in Figure 4.9c and 4.9d, respectively. The line scan reveals a gap of ≈50 nm between the neighboring crystals, which is characterized by the presence of a void or trench-like structure obtained from the line scan (Figure 4.9c). The void between the crystals can be observed horizontally (Figure 4.9c) and vertically (Figure 4.9d). The height profiles showed a similar gap in-between h-BN crystal, indicating that the voids are real features. Thus, STM imaging demonstrated that h-BN films grown on Cu do not fully coalesce, which is essential for h-BN film continuity.

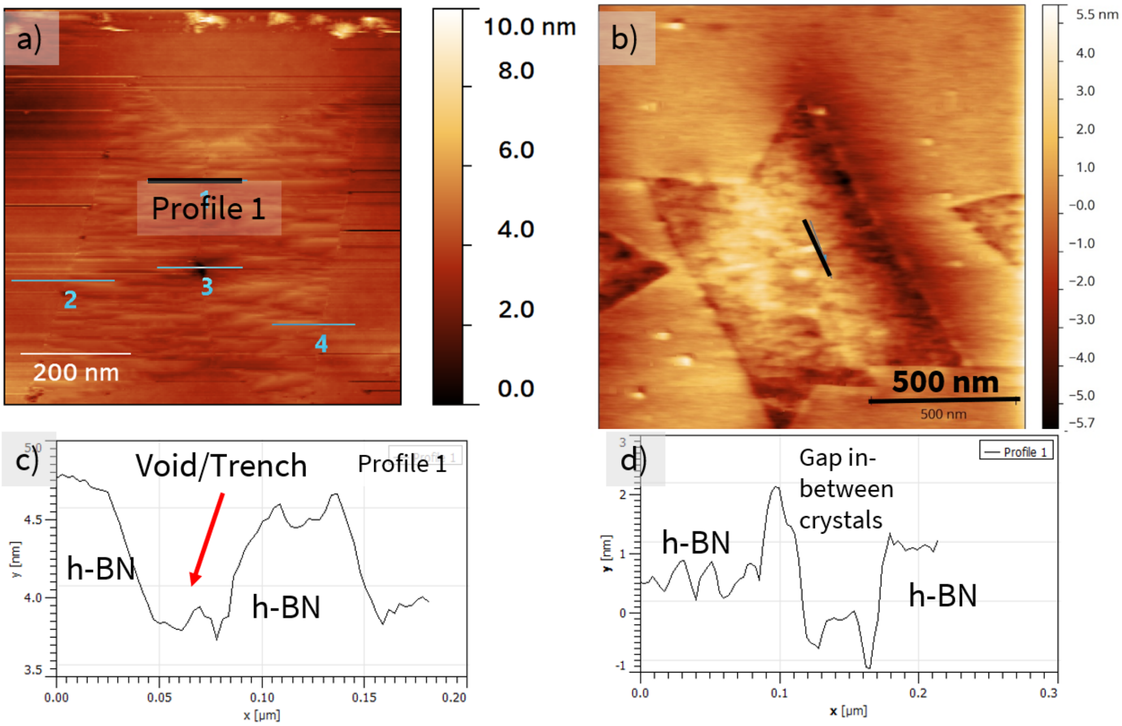

Figure 4.9: STM images of two h-BN neightboring crystals. a) STM image with a 1 µm × 1 µm scan size, b) STM image with a 2 µm × 2 µm scan size. The height profiles shown in c) and d) are indicated in (a) and (b), respectively.

4.2.5 Summary

FT-IRRAS offers a method to quickly confirm the growth and to assess the h-BN-substrate coupling from the peak shifts of the A_{2U} (823 cm^{-1}) vibrational mode. The AFM, STM and SEM characterization results (Figures 4.4-4.8) establish that h-BN is following the surface profile of the Cu substrate, while simultaneously protecting the Cu surface from oxidation. This also reveals that the Cu surface is extremely rough and not ideal for the growth of a 2D material like h-BN. In addition, h-BN film appeared to have poor coalescence as there is a noticeable gap of about 50 nm measured between h-BN neighboring crystals using STM. To mitigate these problems, there is a need for a surface preparation technique to smoothen the Cu substrate before h-BN growth [206, 207, 208, 212, 218, 223, 224].

4.3 Influence of Cu surface preparation on h-BN and graphene growth

To better understand the role of Cu surface on h-BN growth, it is important to assess the Cu foils as supplied by the vendors such as Alfa Aesar and Sigma Aldrich. The first step of the process is to cold roll the Cu ingots into two metal rollers (Figure 4.10) at room temperature and ambient pressure [225, 226]. Multiple studies have demonstrated that this method leads to a smaller Cu grain size, as well as transfer of imperfections and impurities from the metal rollers to the imprinted Cu foil (Figure 4.10b and 4.10c) [212,227,228]. The smaller grains also contribute to an overall increase in the amount of grain boundary perimeter, which act as a potential nucleation site that limit the areal growth of h-BN. Additionally, it is shown the impurities that embed themselves during the cold rolling process also act as potential nucleation site, disrupting the continuity of 2D film growth [212]. The surface also has a high amount of oxide (CuO$_x$), which reduces the overall catalytic properties of Cu [100]. This makes the Cu surface extremely unsuitable for the growth of atomically thin 2D materials.

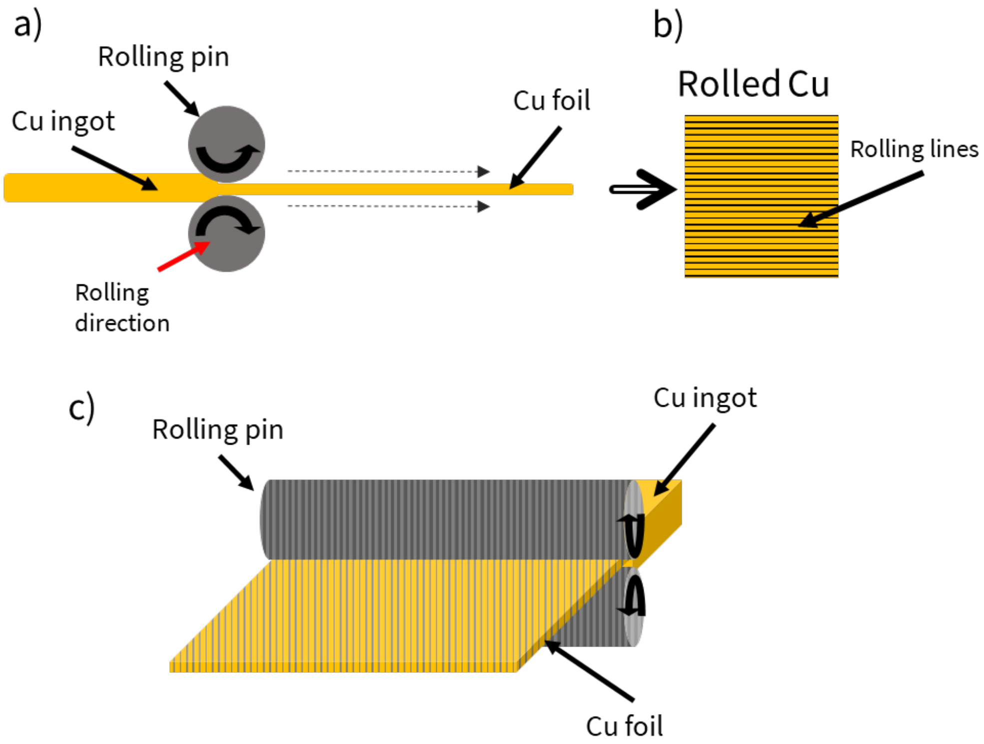

Figure 4.10: Cold rolling process of Cu. a) Cu ingot is fed into rolling pins and Cu foil comes out, b) Morphological state of rolled Cu foil, c) Rolling pins imperfections imprinted on Cu foils. Image obtained and modified from [48].

Various methods were reported [100] to mitigate these issues such as etching in diluted Ni and acetic acid [229, 230, 231], thermal annealing in H_2/N_2 environment [191, 230, 232, 233, 234, 235, 236], and mechanical polishing [237]. While these methods offer improvements over native substrates, there remain secondary issues such as etch pits and acid residue on the surface. Thermal annealing in a reduction environment was reported to enlarge grains through recrystallization [192, 232, 233], while also removing the native oxide [234, 235, 236] on Cu surface. However, thermal annealing also introduces surface defects such as step edges that became more prominent [238]. Based on extensive literature review, there appears to be no comprehensive solution reported to facilitate large Cu grains, with no native Cu oxide and atomically smooth surface roughness. This work employs a two-step process to address these issues: thermal annealing and electropolishing. Thermal annealing increases the Cu grain size, removes the Cu oxide and smoothens the Cu foil (Figure 4.11). A two-additive electropolishing was developed to further smoothen and brighten the Cu surface, leaving a Cu surface that was ideal for 2D material growth [48].

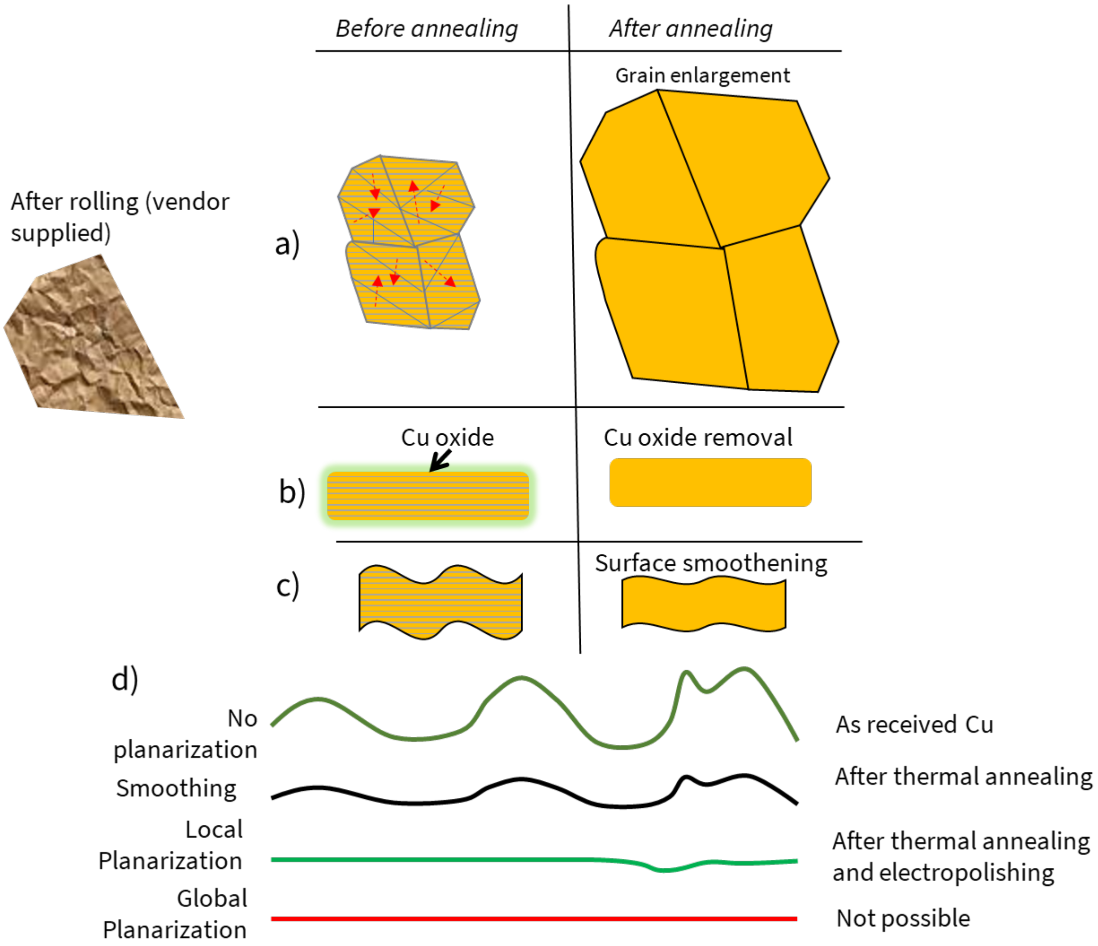

Figure 4.11: Schematic illustration of surface improvement after thermal annealing and electropolishing process. a) Recrystallization of Cu grains leading to larger grains after thermal annealing, b) Cu native oxide removal and c) Cu surface smoothening during thermal annealing in reduction environment, d) Cross-sectional view of the evolution of Cu surface with different processing conditions. Image obtained and modified from [48].

SEM reveals that the Cu surface is riddled with features such as rolling lines, step edges, grain boundaries, and impurities, necessitating a discussion on the state of the vendor supplied Cu foil. Figure 4.12 shows the SEM micrographs using both in-lens and SE mode and with two different magnifications (500X and 2000X) of the Cu surface. The result of cold rolling process is evident in the micrographs in the presence of the smaller grains that are clearly visible from different contrasting region in the SE mode micrograph (Figure 4.12b). The metal rolling pins that imprint rolling lines on the Cu foil are visible at both the magnifications (Figures 4.12b and 4.12d) but are more evident under the SE mode (Figure 4.12d). The surface morphological analysis using SEM conveys the poor state of Cu surface that makes it unsuitable for 2D material growth

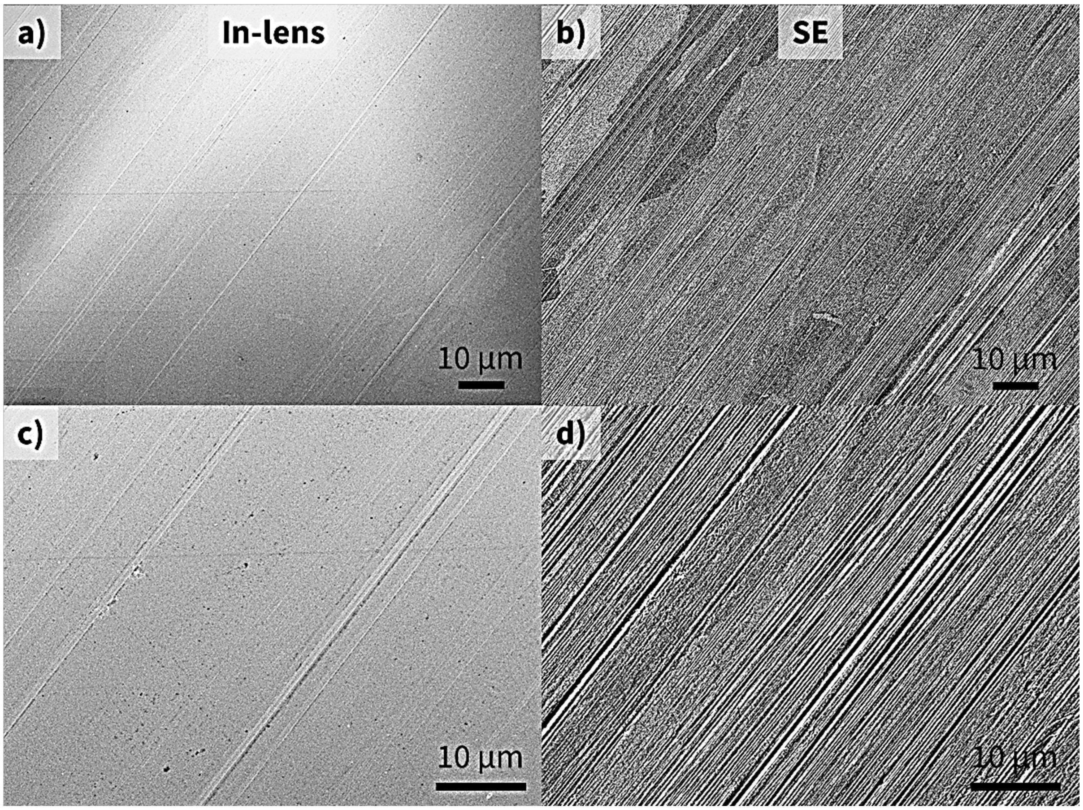

Figure 4.12: SEM micrographs of Cu surface a) In-Lens at 500X magnification, b) secondary electrons at 500X magnification, c) In-Lens at 2000X magnification, d) secondary electrons at 2000X magnification.

The aforementioned two-step thermal annealing and two-additive electropolishing step overcomes the imperfections of the Cu foil. The details of the two-step method are discussed in Section 3.2 and the development of the method is reported in [48, 69]. The thermal annealing step reduces the native Cu oxide, leading to Cu grain enlargement and surface smoothening.

This involves annealing the Cu sample at 1030°C for >5 hours in H_2/N_2 (20/180 sccm) environment under atmospheric pressure. The electropolishing step further removes the native oxide, surface defects, and planarizes the Cu sample. As described in the experimental section (Section 3.2), the electropolishing setup has a Cu anode, Pt cathode, and an electrochemical bath solution. Utilizing pure phosphoric acid to electropolish the Cu foil causes the formation of etch pits caused by oxygen bubbles [239, 240, 241, 242, 243, 244]. This is overcome by making an etchant composed of phosphoric acid, acetic acid, and ethylene glycol in a 2:1:1 ratio by volume. This decreases the current density and slows down the release of oxygen bubbles at the Cu anode [239, 240, 241, 242, 243, 244].

Figure 4.13 shows optical micrographs as well as Nomarski images of the Cu surface after each processing step. Following the cold rolling process described above, the Cu surface is filled with rolling lines as seen in the optical micrograph (Figure 4.13a). After thermal annealing, the optical micrograph shows the Cu surface smoothens as expected (Figure 4.13b). The Nomarski image (Figure 4.13e) reveals variations such as step edges on the Cu surface. After electropolishing, the Cu surface is free of these surface defects and appears extremely planarized (Figure 4.13c). The Nomarski image shows a wavy nature of the Cu sample, which could have formed during sample handling as the Cu sample is measured to be only $\approx$18 µm thick after electropolishing. The surface smoothness of the Cu foil substrate after the two-step process makes it suitable for 2D material growth.

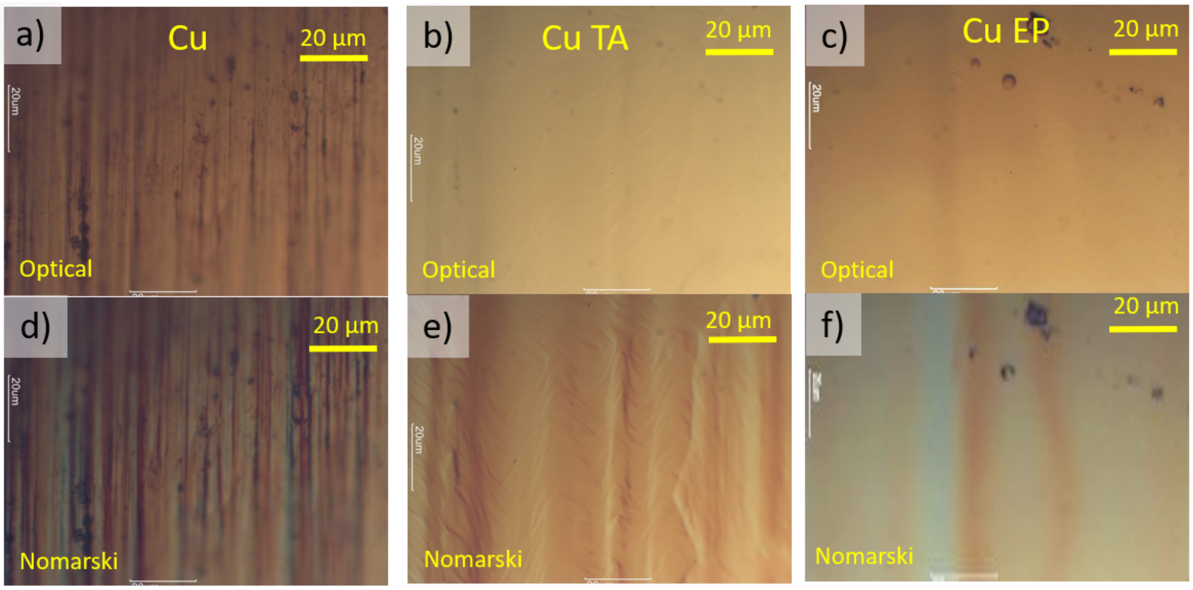

Figure 4.13: Optical micrographs of Cu surface after each processing step a) Vendor supplied Cu, b) Cu thermally annealed, c) Cu thermally annealed and electropolished. Nomarski image of d) Cu, e) Cu thermally annealed, f) Cu thermally annealed and electropolished. Image obtained from [48].

Figure 4.14 shows topographical information from the SEM micrographs for the Cu substrates after various stages of the surface treatment process. Consistent with the optical images from Figure 4.13, the vendor-supplied Cu ingot is rough with rolling lines and small Cu grains (Figure 4.14a). Thermal annealing increases the grain size of Cu from ≈5-10 µm to >100 µm and the rolling lines are noticeably absent after this process (Figure 4.14b). Further electropolishing of the thermally annealed sample smoothens and planarizes the Cu sample allowing the Cu grains to become clearly visible (Figure 4.14c).

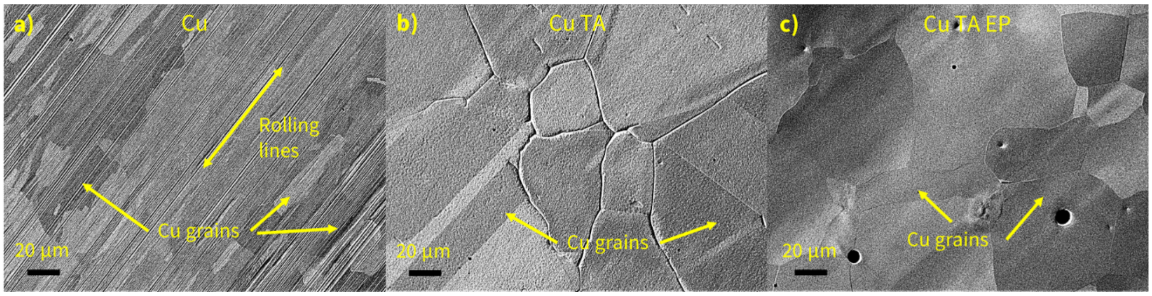

Figure 4.14: SEM micrographs of Cu samples in secondary electron imaging mode. a) Vendor supplied Cu, b) Cu thermally annealed, c) Cu thermally annealed and electropolished.

4.3.1 The effects of Cu surface preparation on h-BN growth

To assess the influence of surface preparation on h-BN crystal growth, h-BN is grown on two sets of Cu samples: vendor supplied Cu, and thermally annealed and electropolished Cu. h-BN is grown on all Cu substrates under identical conditions, as described in Section 3.2. Figure 4.15 shows the SEM micrographs of h-BN crystals on unpolished Cu (Figure 4.15a) and polished Cu (Figure 4.15b) . The unpolished Cu substrate features a high density of h-BN crystals with a size of $\approx$1 µm. The density is calculated to be $\approx 38\times10^6/\mathrm{cm}^2$ from counting the number of h-BN nucleates ($\approx$178 crystals) in the SEM image and dividing the value by the area of the SEM image. On the polished Cu substrate, there is significant decrease in the density of h-BN crystals but with an increase in crystal to $\approx$4 µm. The h-BN crystal density is calculated to be $\approx 38\times10^6/\mathrm{cm}^2$ from the number h-BN nucleates ($\approx$15 crystals). The decrease in density of h-BN crystals and increase in crystal size demonstrates the impact of thermal annealing and electropolishing processing technique in the reduction of nucleation site density of h-BN.

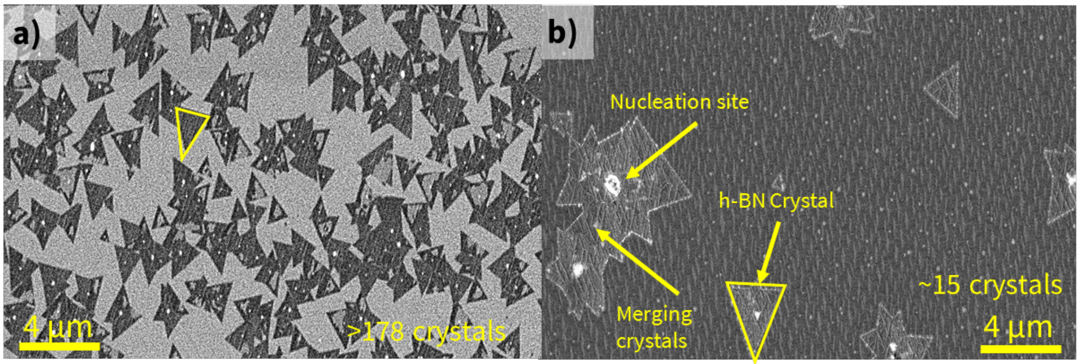

Figure 4.15: SEM micrographs of h-BN crystals grown a) unpolished Cu, b) thermally annealed and electropolished Cu. The two-step annealing, electropolishing results in the reduction of density of h-BN crystals and increase in crystal size. Reprinted with permission from [69]. Copyright 2017 American Chemical Society.

h-BN film is grown on vendor supplied Cu and Cu prepared with the two-step surface preparation technique to assess the influence of surface preparation of the film quality. Figure 4.16 shows the SEM micrographs of h-BN films grown on Cu and surface prepared Cu substrates under identical growth conditions. The SEM micrographs taken at 2000X and 5000X magnification (Figures 4.16a and 4.16b) show that the h-BN film on Cu is frequently riddled with secondary nucleation, which is an agglomeration of more than one layer of h-BN with lateral sizes in hundreds of nanometers. It is commonly observed at or near the spike-like nucleation sites, h-BN films close to Cu grain boundaries and at the polycrystalline h-BN film grain boundaries. The existence of secondary nucleation is undesirable as it reduces the overall film uniformity. As h-BN film is also grown on electropolished Cu, the role of impurities is expected to be minimized leading to better film uniformity. The absence of observable secondary nucleation on the h-BN film grown on electropolished Cu (Figure 4.16c and 4.16d) demonstrates that the Cu foil substrates prepared using the two-step thermal annealing and electropolishing process yields a uniform monolayer of h-BN film.

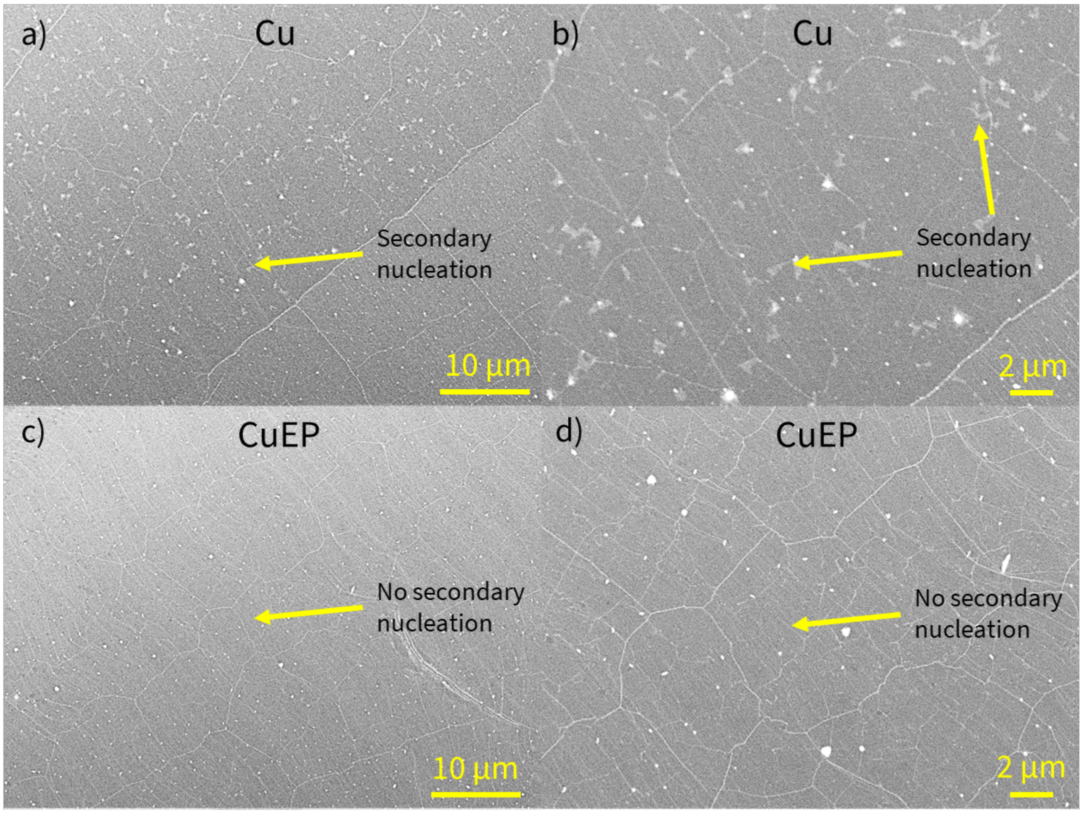

Figure 4.16: SEM micrographs of h-BN film on Cu and electropolished Cu at two different magnifications a) Cu at 2000X, b) Cu at 5000X, c) Electropolished Cu at 2000X, d) Electropolished Cu at 5000X.

4.3.2 The effects of Cu surface preparation on graphene growth

To test the versatility of the Cu samples prepared using this two-step process, graphene is also grown on the treated Cu substrates using optimized CVD growth conditions for graphene. Graphene is grown on both Cu and surface-treated Cu to understand the effect of surface preparation of Cu, graphene nucleation and quality. As a vertical CVD furnace is used, the top side of the sample is directly exposed to the precursor flow. The back side typically has a slower growth as it is not directly exposed to the incoming precursor flow and therefore, the front face is expected to have film growth and the back side is expected to grow graphene crystals. The benefit of probing the front and back side of Cu substrates is that the graphene film and crystal growth can be observed. Figure 4.17 shows the SEM micrographs of both the front (the growth face) and the back side of the graphene grown on unpolished and electropolished Cu samples. As demonstrated (Figures 4.17a and 4.17c), the graphene growth on unpolished Cu is non-uniform, riddled with gaps, and contain a noticeable amount of secondary nucleation. On the contrary, the electropolished Cu showed a well-coalesced graphene film forming on the front side of the Cu sample (Figure 4.17b). The graphene crystals observed on the back side are measured to be >50 μm in size (Figure 4.17d). This highlights the role of electropolished Cu sample for the growth of well-coalesced graphene films and large graphene crystals.

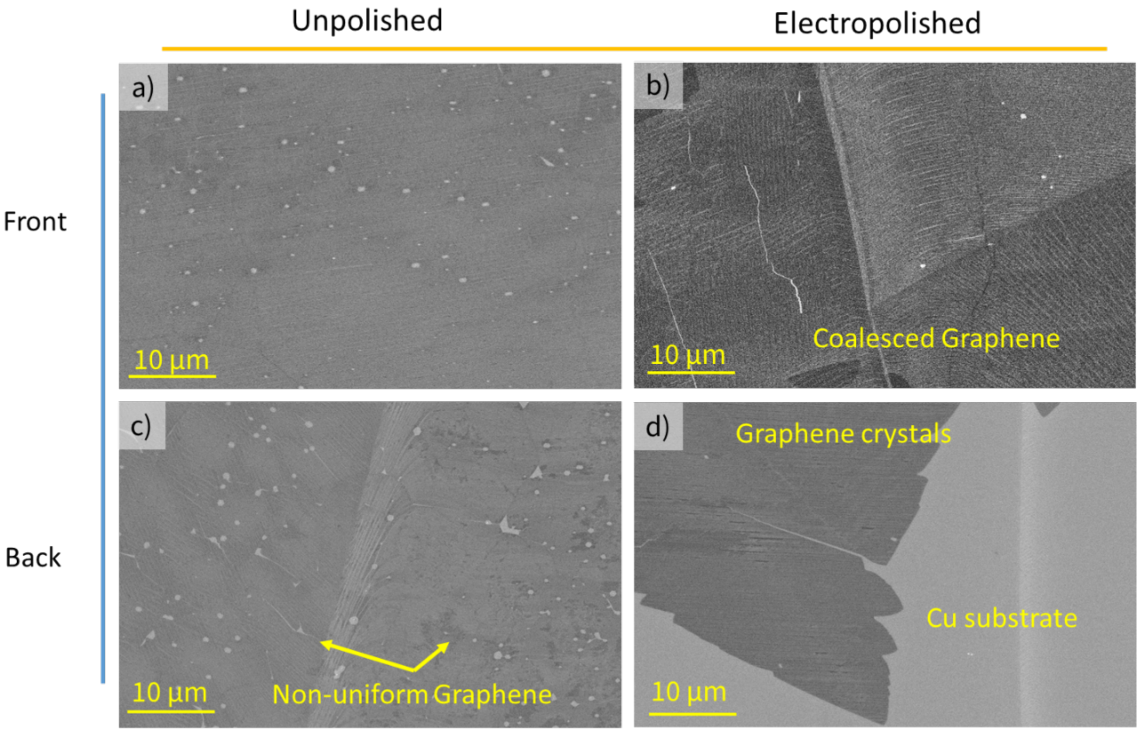

Figure 4.17: SEM micrographs of graphene grown on unpolished and polished Cu substrates. a) Graphene on unpolished Cu front side, b) graphene on polished Cu front side, c) graphene on unpolished Cu back side, d) graphene on polished Cu back side. The scale bar is 10 μm.

Raman spectroscopy is used to assess the structural quality of graphene films, from the shifts in the characteristic peaks, grown on both unpolished and electropolished Cu. The thickness and the growth quality were evaluated with the characteristic peaks: D (≈1350 cm^{-1}), G (≈1582 cm^{-1}) and 2D (≈2685 cm^{-1}) bands [245, 246, 247, 248]. The D band, also known as defect or disorder band, is an indication of atomic defects (point defect) present in the hexagonal lattice. The band is typically very weak and is a result of one phonon vibrational process [245, 246, 247, 248]. The D band is dispersive and consequently the position and the shape of the band will vary with different laser frequencies. The G band is the primary vibrational mode of 2D graphene and 3D graphite indicative of sp^2 hybridized carbon in hexagonal configuration [210, 245, 246, 247, 248, 249, 250]. The 2D or G' band is the result of two phonon lattice vibration process. However, unlike the D-band, the 2D band does not arise due to defects and can be observed even when there is no D-band present in the spectra. The D, G, and 2D bands are useful to determine the layer thickness and the growth quality with reference to the lack of defects [210, 245, 246, 247, 248, 249, 250].

The layer thickness of graphene can be determined by the shift in the G-band, which shifts to lower energy indicating softening of the bonds as the layer count increases. Simultaneously, the 2D band, mainly its shape and intensity, can also be used to determine the layer count [210, 245, 246, 247, 248, 249, 250]. Unlike the G-band, the 2D band is dispersive, which makes it sensitive to defects and functionalization [210, 245, 246, 247, 248, 249, 250]. Additionally, the 2D band shape for single layer graphene can be fitted with a single Lorentzian peak with a full width half maximum (FWHM) of $\approx$30 cm^{-1} and widens with successive layers of graphene. A defect-free monolayer graphene has an accepted 2D to G band (I$_{2D/G}$) intensity of two [210,245,246,247,248, 249, 250]. The degree of defects within a graphene sample can also be similarly characterized. The presence of a strong D-band is a direct indicator of presence of atomic defects, where the intensity is proportional to the quantity of defects in the graphene sample. The atomic defects could amount to point defects such as vacancies, and substitutional impurities [210, 245, 246, 247, 248, 249, 250].

Figures 4.18 and 4.19 show the Raman spectra and dark field images of the region from which spectra are obtained for both unpolished and electropolished, front and back sides of samples, respectively. In Figure 4.18a, the front side of the graphene on unpolished Cu, there is a clear presence of the D-peak indicating defects. There is also a notable shift in the G-band, which can either indicate defects or doping of graphene by the Cu substrate. Additionally, the $I_{2D/G}$ changes at different positions on the unpolished samples, which indicates inconsistent thickness and excessive secondary nucleation. However, the Raman spectra of graphene on electropolished Cu are clearly different. The D-peak is present only on Point 3 of graphene grown on electropolished Cu sample (Figure 4.18f), with no observable shift in the G and 2D bands. A list of the D, G and 2D peak positions from the Raman spectra for the front side of the sample are listed in Table 1.

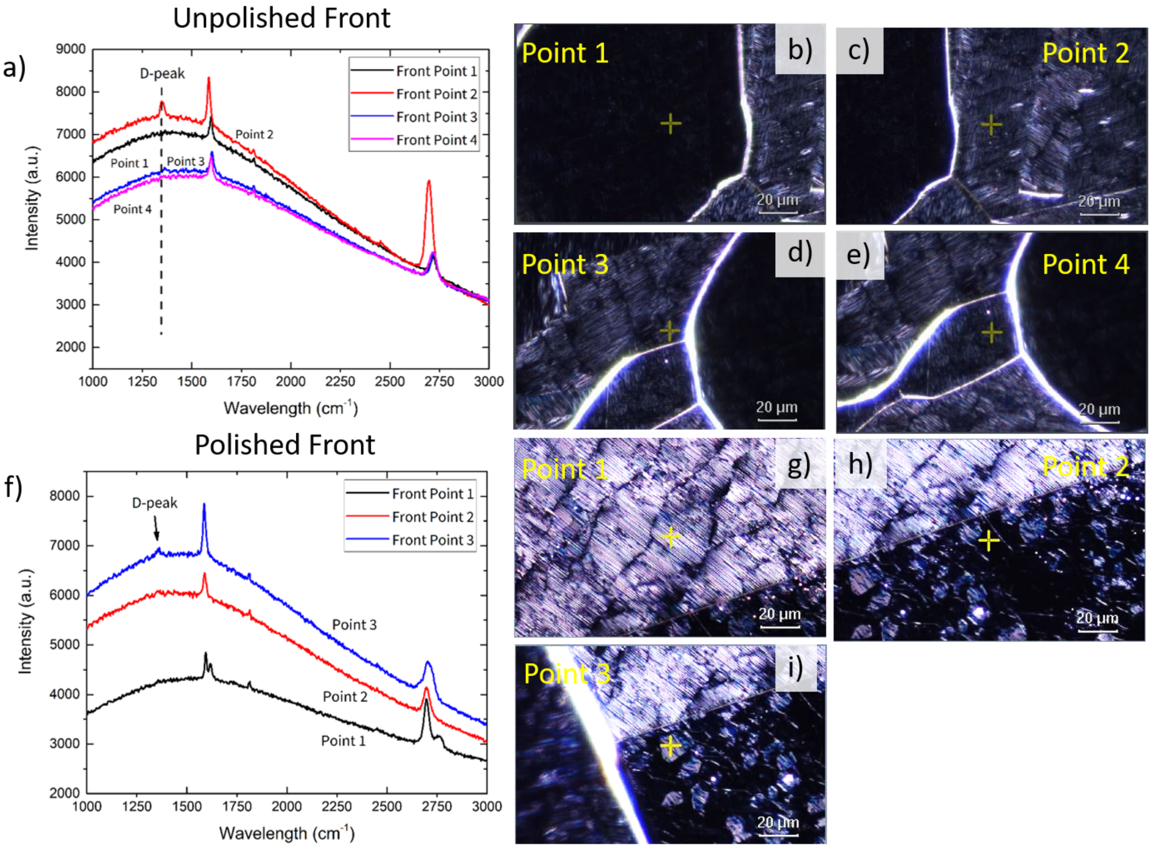

Figure 4.18: Raman spectroscopy and dark field optical images of graphene on unpolished and electropolished Cu (front facing) a) Raman spectra of graphene grown on unpolished Cu, b-e) dark field optical images of spectra 1-4 shown in (a). f) Raman spectra of graphene grown on polished Cu, g-i) dark field images of spectra 1-3 shown in (f). The crosshair on all the darkfield images indicate the location where Raman spectra was obtained.

Table 4.1: D, G and 2D peak positions from Raman spectra of various points of graphene on unpolished and polished Cu substrate, front side.

	Point	D-Peak Position (cm^{-1})	G-Peak Position (cm^{-1})	2D-Peak Position (cm^{-1})
Unpolished Front	Point 1	0	1586	2720
	Point 2	1347	1598	2697
	Point 3	1363	1602	2720
	Point 4	1365	1600	2712
Polished Front	Point 1	0	1594	2696
	Point 2	0	1588	2697
	Point 3	1361	1586	2703

Raman spectra of graphene grown on the back side of the unpolished and electropolished Cu sample is shown in Figure 4.19. Similar to the front side, graphene on the unpolished side has a small D-peak indicating defects. While there is no noticeable shift in the G-peak, the $I_{2D/G}$ is around 2 suggesting monolayer graphene growth. The graphene growth on the unpolished back side appeared to be of a higher quality than the front (growth) side, which is based on the absence of D-peak. In contrast, there is no visible D peak on the electropolished Cu sample indicating a lack of defects (refer Figure 4.19e). A list of the D, G and 2D peak positions from the Raman spectra for the back side of the sample are listed in Table 2. Additionally, the graphene crystals, which are approximately 100 µm in size, are visible using the dark field optical microscope and complement the findings from the SEM micrographs (Figure 4.17).

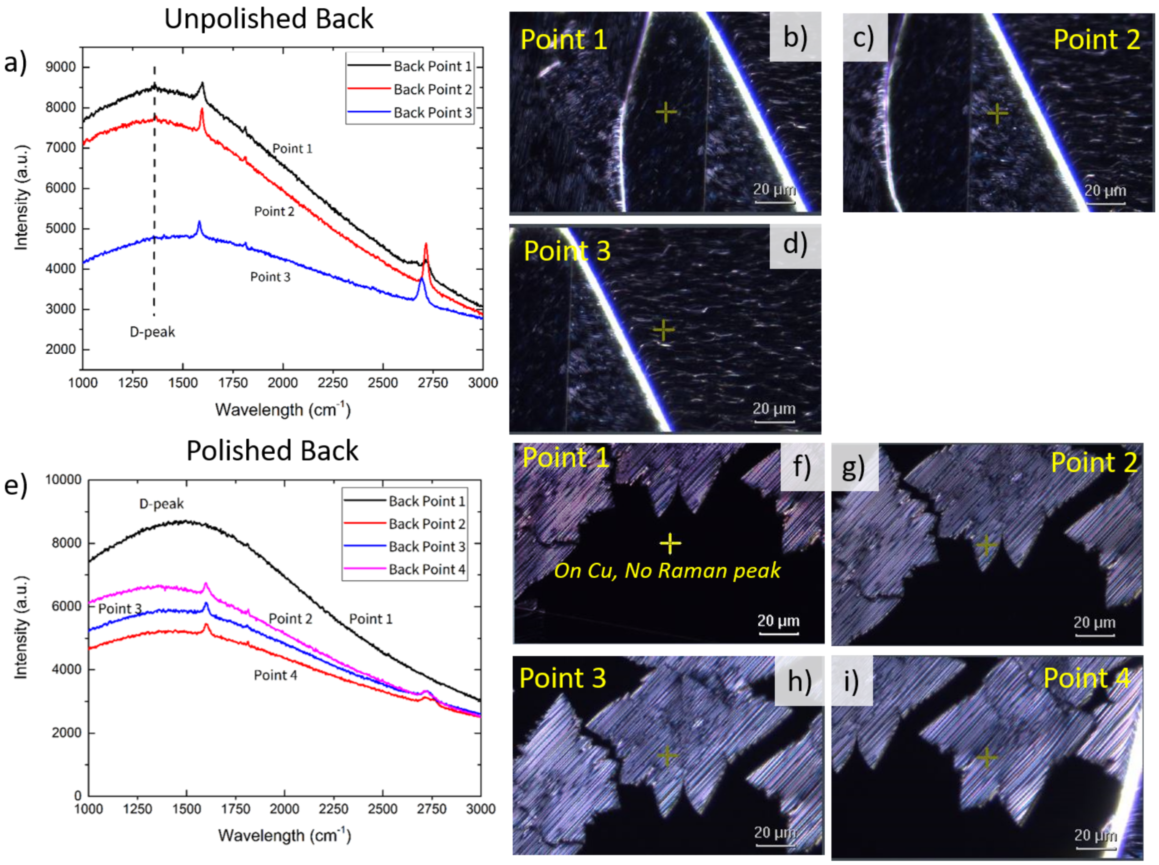

Figure 4.19: Raman spectroscopy and dark field optical images of graphene on unpolished and electropolished Cu (back facing) a) Raman spectra of graphene grown on unpolished Cu, b-d) dark field optical images of spectra 1-3 shown in (a). e) Raman spectra of graphene grown on polished Cu, f-i) dark field images of spectra 1-3 shown in (e). The crosshair on all the darkfield images indicate the location where Raman spectra was obtained.

Table 4.2: D, G and 2D peak positions from Raman spectra of various points of graphene on unpolished and polished Cu substrate, back side.

	Point	D-Peak Position (cm^{-1})	G-Peak Position (cm^{-1})	2D-Peak Position (cm^{-1})
Unpolished Back	Point 1	1363	1598	2712
	Point 2	1365	1596	2715
	Point 3	0	1592	2693
Polished Back	Point 1	0	0	0
	Point 2	0	1598	2722
	Point 3	0	1598	2728
	Point 4	0	1598	2722

4.3.3 Summary

Upon assessing the morphology of Cu, it can be concluded that the surface is composed of impurities and structural defects, making the material non-ideal for 2D material growth. To address this, a two-step thermal annealing and electropolishing technique is developed to create a surface that is extremely smooth and well suited for both h-BN and graphene growth. This resulted in enlargement of h-BN and graphene crystal size, fewer nucleation sites for h-BN, and uniformity in h-BN and graphene growth as the secondary nucleation is eliminated.

The growth of h-BN is so far discussed from a surface-oriented perspective, focusing on the reduction of nucleation sites and increasing the h-BN crystal size by using a novel surface preparation technique. While the h-BN crystal and film growth relationship with the Cu surface is established in this work and in the literature [66, 69], the growth dependence on the various Cu grain orientations of a polycrystalline sample has not been thoroughly studied in the literature.

4.4 Role of Cu grain orientation on h-BN growth

Electron backscattering diffraction (EBSD) mapping and scanning electron microscopy (SEM) are used to address the effect of Cu grain orientation on h-BN crystal growth on both unpolished and electropolished polycrystalline Cu samples using APCVD. The advantage of studying h-BN growth on polycrystalline Cu is that there are multitude of grain orientations in existence adjacent to each other, along with the low index orientations: (100), (111), and (110). This ensures that the entire sample has identical growth conditions: precursor flow, pressure, and temperature.

4.4.1 Microstructure of Cu foil substrates

The microstructure of Cu samples are analyzed using EBSD (as shown in Figure 4.20) to get grain statistics such as grain size, grain orientation distribution, for two different Cu purities: low purity Cu (99.99%) and high purity Cu (99.999%), and two different annealing temperatures for high purity Cu. The vendor supplied low purity Cu (Figure 4.20) has a small average grain size of $\approx$5 µm, making it less desirable for h-BN growth. In contrast, the vendor supplied high purity Cu has a larger average grain size of $\approx$20 µm (Figure 4.20b). This increases the prospects of having a larger Cu grain after annealing, on the order of hundreds of microns, making it suitable for h-BN growth [69]. The average grain size increases further with thermal annealing at 500°C and 1030°C (Figures 4.20c and 4.20d). As the annealing temperature increases, the smaller grains are consumed by the adjacent larger grains during the recrystallization process, leading to larger grains [251] (Figure 4.20d). After thermal annealing, the Cu crystal twins [252, 253] form at 500°C and are well resolved when Cu is annealed to 1030°C. Simultaneously, there is an overall dominance of (100)-like orientation of Cu grains observed [254]. There is also a noticeable existence of high index grains, where the grain orientations are neither (100), (111) or (110)-like. As grain boundaries act as potential nucleation sites for h-BN growth, larger grains reduce the overall boundary perimeter/area ratio limiting the role of grain boundaries as h-BN nucleation sites.

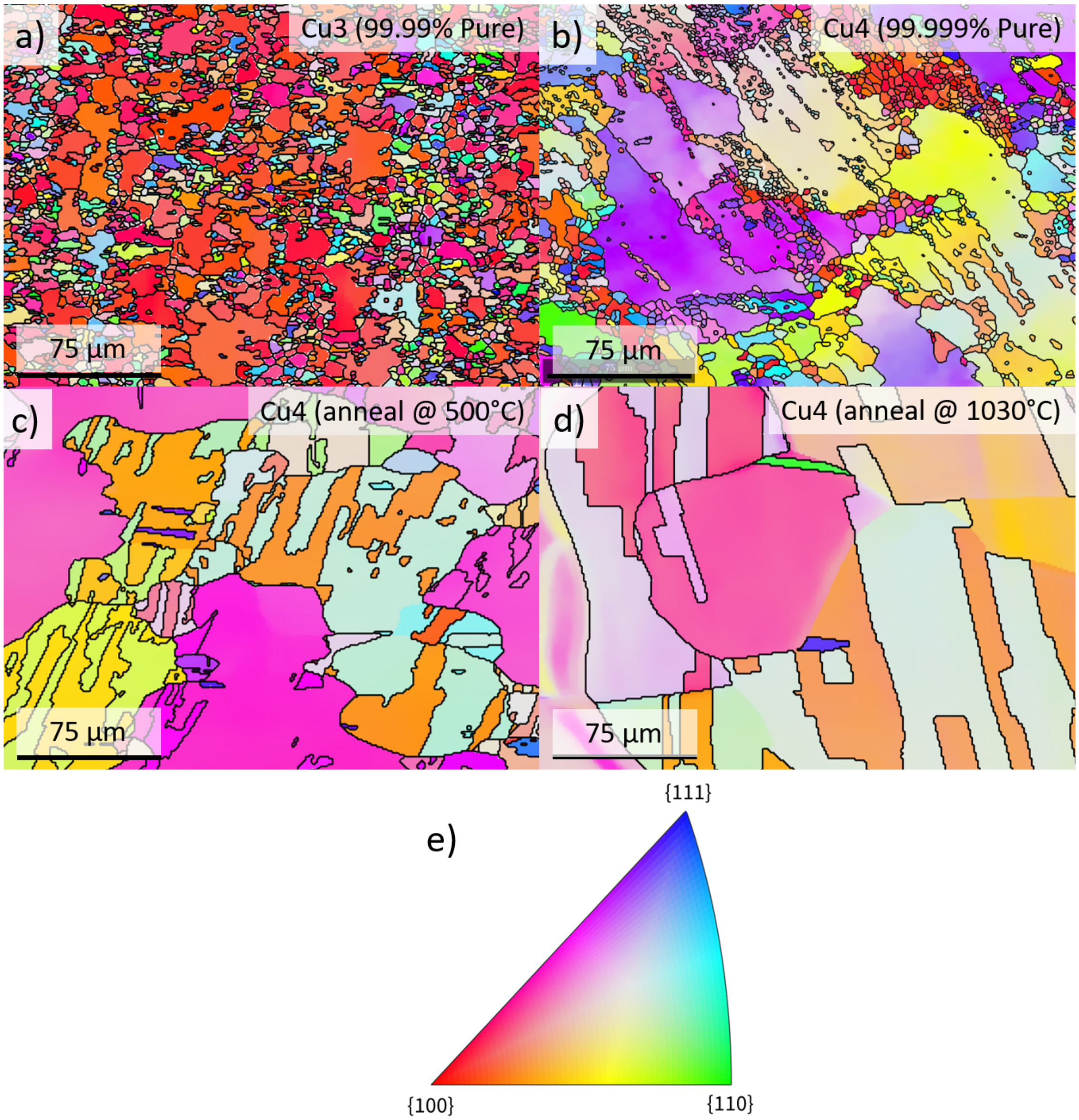

Figure 4.20: EBSD maps of Cu foils of 25 µm thickness with a) low purity Cu: 99.99% b) high purity Cu: 99.999%, c) high purity Cu annealed at 500 °C, d) high purity Cu annealed at 1030°C. The Cu grain size increases with purity and hence, higher purity Cu is desirable for growth. After annealing, the grain size increases through recrystallization. c) shows increase in grain in comparison with b). There is also noticeable formation of twin grains. d) After annealing close to the melting temperature of Cu, the crystal size increases even further and twin grains are distinctly formed with parent and daughter grains in twin crystals showing different orientations. e) the inverse pole figure for the EBSD maps.

A total of five high purity Cu samples are characterized by EBSD after h-BN growth: two unpolished Cu samples with h-BN crystals, one Cu electropolished with h-BN crystals and two Cu samples with h-BN film. As discussed in the methods section, SEM micrographs of all the grains in the EBSD map are obtained at various magnifications. Figure 4.21 shows a summary of SEM and EBSD correlated micrographs of h-BN grown on Cu across grains at all the three orientations: (100), (111), (110) and high index orientations.

4.4.2 Relating h-BN growth with Cu grain orientation

Figure 4.21 illustrates differences in h-BN crystal nucleating on different Cu grain orientations on an unpolished Cu foil substrate. The dark grey triangular features are h-BN nucleates or crystals growing on the Cu substrates. By counting the number of h-BN nucleates on the SEM micrograph, the nucleation density can be obtained. On (100)-like oriented Cu grain (Figure 4.21a), there is little, or no nucleation of h-BN observed. There are $\approx$45 crystals on the (100)-like orientation, which amounts to a density of 1.68$\times$10^6 crystals/cm^2. Both (111)-like (Figure 4.21d) and (110)-like (Figure 4.21g) orientations have a higher density of h-BN crystals at $\approx$527 and $\approx$158 crystals, respectively. This amounts to a density of 1.97$\times$10^7 crystals/cm^2 for (111)-like and 5.91$\times$10^6 crystals/cm^2 for (110)-like orientations. This trend of less-preferred growth on (100) orientations is also reported by Hite et al [68], where the surface energy of each of these crystal orientations is assumed to dictate growth rate. In contrast to low-index Cu grains, the high index Cu grain (Figure 4.21j), has a quasi-film of h-BN forming, suggesting a much faster growth or nucleation rate than on low indexed Cu grain orientations.

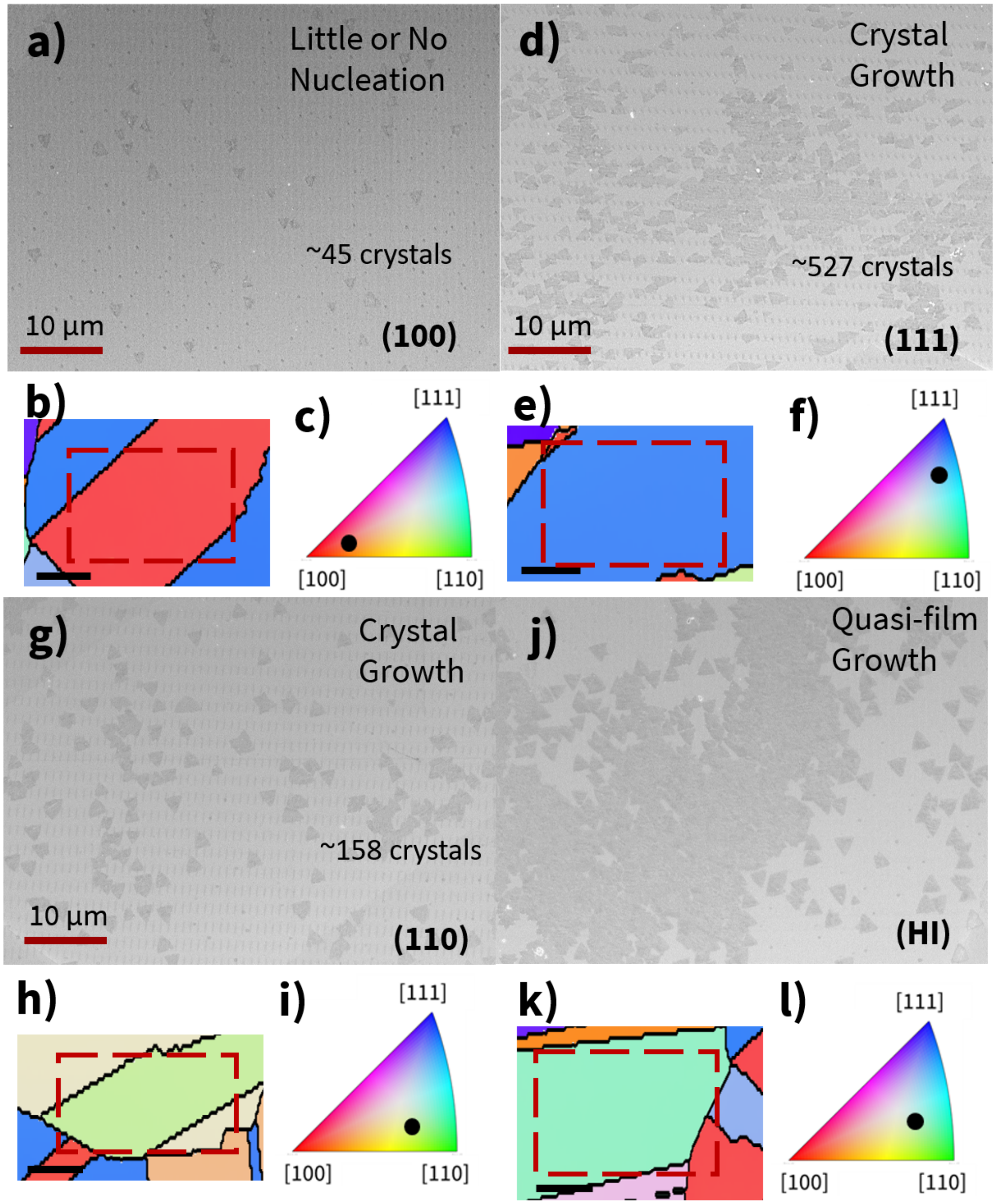

Figure 4.21: Summary of h-BN growth across a Cu sample. a) Shows little or no nucleation on (100)-like crystal ($\approx$45 crystals, 1.68×10^6 crystals/cm^2) b) and c) EBSD map of the (100)-Cu grain and the orientation location on IPF. d) Cu grain with h-BN crystal growth ($\approx$527 crystals, 1.97×10^7 crystals/cm^2) on a (111)-like oriented Cu grain shown in e) and f) EBSD map of the grain and the orientation on IPF. g) Cu grain with h-BN crystal growth ($\approx$158 crystals, 5.91×10^6 crystals/cm^2) on a (110)-like oriented Cu grain shown in h) and i) EBSD map of the grain and the orientation on IPF. j) The high index (HI) region where a quasi-film growth is observed. k) and l) EBSD map of the grain and the grain orientation on IPF. The approximate region of where SEM micrograph was taken is indicated on the EBSD map of the grain with a dashed rectangle. The scale bars for the EBSD maps are 25 µm.

Despite thermal annealing, which leads to an increase in Cu grain size and lower surface roughness, there is presence of microfaceting (microscopic variations in surface facets) on the Cu surface. The microfacets on the Cu surface were reported to influence the growth of h-BN and graphene on Cu [163, 255]. The microfaceting cannot be observed using EBSD as the probing depth is >20 nm [213]. Hence, an additional processing step such as electropolishing can be used to mitigate the role of microfacets on h-BN growth and to have a planarized Cu surface.

The Cu grain dependent growth of h-BN is much more evident on the electropolished sample (Figure 4.22). There is little or no nucleation of h-BN observed on (100)-like Cu grain orientation (Figure 4.22a), which agrees with the h-BN growth on (100)-like unpolished Cu sample discussed above. The density of h-BN nucleation is $\approx$1.01$\times$10^6 crystals/cm^2 on the (100)-like orientation. The dark spots on the sample are possibly aminoborane nanoparticles [140], which may decompose upon subjecting the sample high accelerating electron voltages during EBSD mapping. The h-BN crystal growth is much more well defined on (111)-like orientation (Figure 4.22d) than on (100)-like grain, with a nucleation density of $\approx$8.45$\times$10^6 crystals/cm^2. This also agrees with the above results on (111)-like orientation. However, the growth on (110)-like orientation is in contrast with the unpolished Cu, where there is a quasi-film growth of h-BN (Figure 4.22g). This can be attributed to the high surface energy of (110)-like orientation as reported by Hite et al [68]. In addition, there is a complete h-BN film formation on a high index-oriented Cu grain (Figure 4.22j), which indicates that the high-index oriented Cu grain has faster relative growth rate than low-index oriented Cu grains. This is also observed on unpolished high index Cu grain. Therefore, the relative Cu grain orientation dependent h-BN growth rates based on the nucleation density are as follows: (100) < (111) <= (110) < (hkl), where hkl is the orientation of the high index Cu grain.

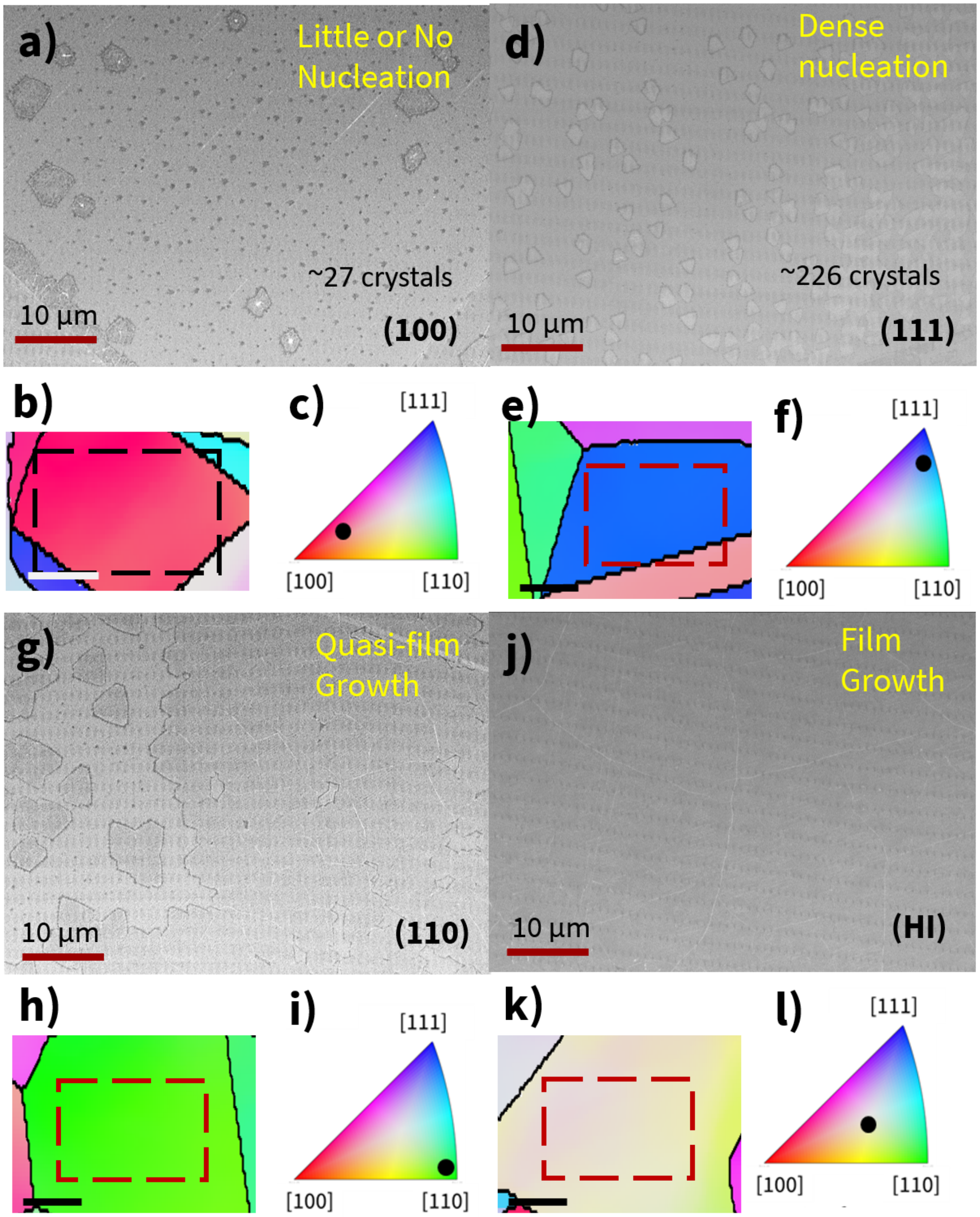

Figure 4.22: h-BN growth on electropolished Cu samples. a) Very little or no h-BN nucleation ($\approx 1.01\times10^{6}$ crystals/cm^{2}) on (100)-like orientation. b) and c) the EBSD map of the grain and grain orientation on IPF. d) Shows moderate density of crystal nucleation ($\approx 8.45\times10^{6}$ crystals/cm^{2}) on a (111)-like orientation. e) and f) have the EBSD map of the (111)-like grain and the grain orientation on IPF. g) Shows a quasi-film growth on a (110)-like crystal. h) and i) show the EBSD map of the (110)-like grain and the grain orientation. j) Complete film growth on a high index grain. k) and l) show the EBSD map of the high index grain and grain orientation on IPF. The approximate region of where SEM micrograph was taken is indicated on the EBSD map of the grain with a dashed rectangle. The scale bars for the EBSD maps are 25 µm.

4.4.3 h-BN growth on Cu twin grains

Another phenomenon is the existence of twin grains, which was prominently observed in the Cu microstructure at >500°C (Figure 4.20) and reported elsewhere for graphene growth on Cu [163, 255]. Twin grains exist as sandwich structures of smaller, rectangular high-index grain (daughter grains) in between larger low-index grains (parent grains) or vice versa. This coupling provides adjacent comparison of h-BN growth on low index and high index Cu grains.

Figures 4.23a and 4.23d show h-BN film growth on the daughter grain with crystals forming on the parent grain. The film growth on the daughter grain is noticeably very uniform, which is attributable to the fast-growing high index orientation of the daughter grain. The parent grains, which are marked by B in both figures (Figure 4.23a and d), have a density of $\approx 4.4 \times 10^6$ and $\approx 9.6 \times 10^6$ h-BN nucleates, respectively. The parent grain, which is of low index orientation, has micron-sized h-BN nucleates growing due to the comparatively moderate growth rate. However, in a Cu grain with low-index daughter grain and high-index parent grain, the opposite is persistent. The contrasting high-index, high-growth and low-index, low-growth agrees with the observations from h-BN growth on non-twin distant Cu grains.

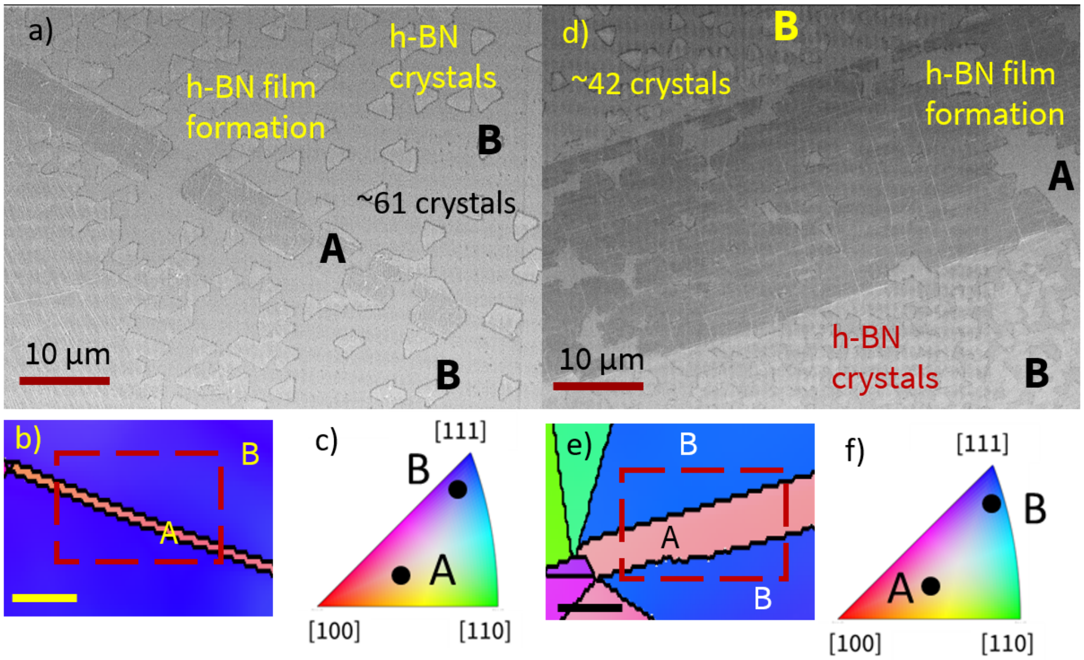

Figure 4.23: h-BN growth across Cu twin grains on an electropolished Cu sample. As twin grains are a frequent occurrence, the daughter grain (indicated by A) has a distinctly different orientation than the parent grain (indicated by B). a) shows an SEM micrograph of a twin grain. The h-BN density on the B grain is $\approx 4.4 \times 10^6$ crystals or nucleates. b) and c) show the EBSD map and the grain orientations of daughter and parent grain on an IPF of (a). d) shows an SEM micrograph of another twin grain structure. e) and f) show the EBSD map and the grain orientations of daughter and parent grain on an IPF of (d). The h-BN density on the B grain is $\approx 9.6 \times 10^6$ crystals or nucleates. In both (a) and (d), the daughter grains (marked by A) have a complete h-BN film coverage.

4.4.4 Statistical categorization of h-BN grown on Cu grains

To understand the context of h-BN growth dependency on Cu grain orientation, a categorization method is employed. The EBSD grain is first correlated with SEM micrographs of h-BN for all the samples and then categorized into three different groups: no growth or nucleation (NG), marginal growth or nucleation (MG) and complete growth (G). All three categories are populated on an inverse pole figure with their respective grain orientations (Figure 4.24). No growth or nucleation is where there are no observable h-BN nucleates or low-density of sub-micron sized h-BN crystals (Figure 4.24a). Marginal growth or nucleation is where there is a high-density of sub-micron size h-BN crystals or nucleates (Figure 4.24b). A complete growth (or growth) is considered when the h-BN crystals or nucleates are greater than micron size, a quasi-film or a complete film formation (Figure 4.24c).

Figure 4.24d shows that h-BN growth occurs across a wide spectrum of Cu grain orientations. Certain Cu grain orientations have faster, or slower growth as assessed by the size of h-BN crystal formed. As an example, there is a noticeable agglomeration of no-growth and marginal-growth data points on (100)-like grain orientations leading to the understanding that (100)-like orientation is a slower growth face. However, the growth is more widely dispersed for (111)-like grain orientations, i.e. all three categories have nearly equal representations, indicating a faster growth orientation than (100)-like grain.

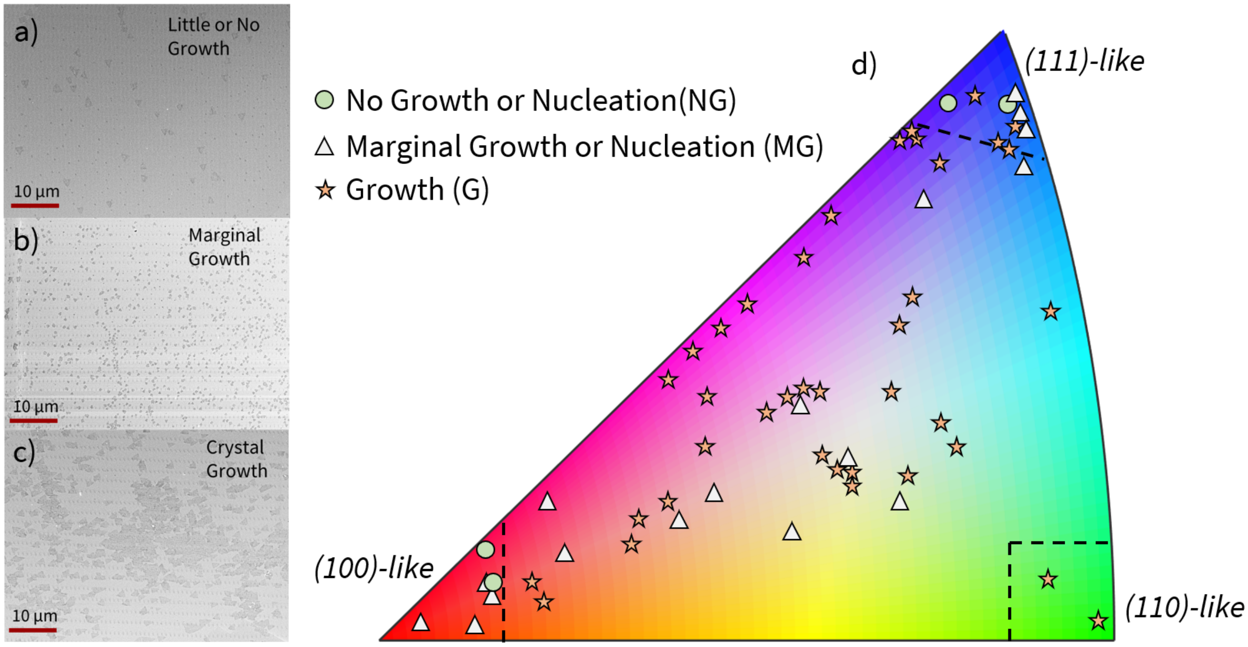

Figure 4.24: Shows h-BN growth statistics across all orientations of grains and across all samples. All data was grouped into three categories: a) no growth or nucleation, b) marginal growth or nucleation and c) growth and shown on the d) inverse pole figure, which indicates the Cu grain orientation. The following are conditions for categorization: In no growth or nucleation, there are smaller, low-density h-BN nucleates are observed; In marginal growth or nucleation, there is clear formation of h-BN crystals, however, they are sub-micron in size; In growth, the h-BN crystals are largest in the samples, and there is also a noticeable film formation.

In contrast to low-index orientations, the majority of good BN growth, crystals or film, occurs on Cu grains with high index orientation. The wide array of data points in the high index region of the IPF supports this statement. Upon closer examination, it is evident that the majority of growth surfaces that yield faster growth lie in-between (100) and (111) orientations, and orientations in the center of IPF. From this categorization method, high-index orientations have a faster growth rate, while the low index orientation (100) has the slowest growth rate. Both (111) and (110) have moderately faster growth rate relative to (100)-like Cu grain orientation.

4.4.5 Summary

In summary, the results indicate that the Cu grain orientation has a strong influence on h-BN growth as studied using EBSD and SEM. This influence is more evident on electropolished Cu than on unpolished Cu as the microfacets on the Cu surface is removed. The statistical categorization of the EBSD and SEM of all the grains show a strong correlation where (100)-like Cu grain orientation has the slowest h-BN growth and high index Cu grain orientation has the fastest h-BN growth.

4.5 Summary and Conclusion

This work demonstrates the understanding of the growth morphology of h-BN on Cu, where the h-BN crystals reflect the underlying Cu substrate. The poor coalescence of h-BN crystals, smaller grain size and extensive secondary nucleation of h-BN are the primary limitations of Cu substrate. By utilizing the two-step thermal annealing and electropolishing technique, a smooth and highly planarized Cu substrate can be created to facilitate the uniform growth of h-BN and graphene.

The influence of polycrystalline Cu grain orientation on h-BN growth is also demonstrated in this work. h-BN growth is the slowest on (100)-like orientation for both unpolished and electropolished samples. While on (111) and (110)-like grain orientations, there is proper h-BN crystal forming in the case of both unpolished and electropolished Cu samples. The categorization method provides a general trend of Cu grain orientation influence on h-BN growth.

5. APCVD GROWTH ON H-BN ON CU-NI BINARY ALLOY SUBSTRATES

This section discusses the results of h-BN growth on Cu-Ni binary alloys in five subsections. The first subsection explores the surface morphology and microstructure of CuNi and NiCu alloys using SEM and EBSD. The second subsection presents the general trend of h-BN growth on alloys. The third and the fourth subsections discuss the specific growth behavior of h-BN on CuNi and NiCu alloys, respectively. The final subsection presents perspectives of h-BN growth differences in CuNi50 and NiCu50 alloys.

5.1 Introduction

The growth and characterization of h-BN on Cu foil substrates has limitations as assessed in the previous section (Section 4). The h-BN growth on Cu is self-limited leading to monolayer crystal and film formation. Additionally, the h-BN film on Cu has poor coalescence leading to discontinuous film growth. Furthermore, the h-BN growth on Ni is observed to be uncontrolled leading to nonuniform multilayered h-BN films. This necessitates examination of alternate substrates to overcome the inadequacies of Cu and Ni substrates. Cu-Ni binary alloys are suggested in this work, where Cu and Ni compositions in the alloy are used to overcome the limitations of Cu and Ni substrates. An additional advantage of using Cu-Ni alloys is that Cu and Ni have complete miscibility in each other, thereby creating a uniform isomorphous Cu-Ni alloy substrate [256].

5.2 Characterization of Cu-Ni alloy substrates

The CVD growth of h-BN on alloys has two contributing parameters: the surface and the microstructure. This requires an inspection of alloy substrates using SEM in both in-lens and secondary electron mode, EDX, and EBSD to glean insights into the alloy surface morphology, composition and distribution of Ni and Cu species, and the microstructure, respectively.

5.2.1 Surface morphology of alloy substrates

The surface morphology of the alloy substrates are characterized qualitatively and quantitatively using SEM and AFM. Figure 5.1 shows the SEM micrographs of unpolished (left column) and mechanically polished (right column) CuNi alloy samples and evolution of the surface morphology with increasing Ni concentration. A Cu sample that is unpolished and mechanically polished (Figures 5.1a and 5.1b) is used for reference. As observed in the left column (Figures 5.1c, 5.1e, and 5.1g), with increasing Ni wt.% in Cu, the surface morphology changes as follows. With 10 wt.% of Ni, the surface has a very pseudo-porous structure, attributable to the difference in Cu and Ni diffusion rates [256]. However, the nature and size of the voids on the alloy surface decreases upon increasing Ni concentration (Figure 5.1e and 5.1g), with CuNi50 showing the least void features on the surface. The grain sizes of the unpolished alloys are not clearly distinguishable due to the presence of pseudo-porous surface morphology.

The SEM micrographs on the polished samples (right column, Figures 5.1d, 5.1f, and 5.1h) show that it loses its pseudo-porous or void-like morphology to reveal the alloy microstructure. With increasing Ni wt.%, the grain size decreases. During the preparation of CuNi alloys for mechanical polishing, increasing Ni wt.% in the CuNi alloy increases the overall stiffness of the sample. Furthermore, lower Ni wt.% CuNi alloys are more susceptible to pitting as can be seen in Figure 5.1d as depressions into the surface. As Ni strengthens during cold working, the Ni-rich CuNi alloys become more resistant to pitting and the depressions or scratches are less evident (Figure 5.1f and 5.1h). Additionally, the polishing slurry (1 µm) is too abrasive at higher vibration intensities (>50%) on the Buehler Vibromat vibratory polisher. Therefore, in the subsequent polishing runs, the vibration intensity is limited to 30% to ensure a smoother finish on all the samples.

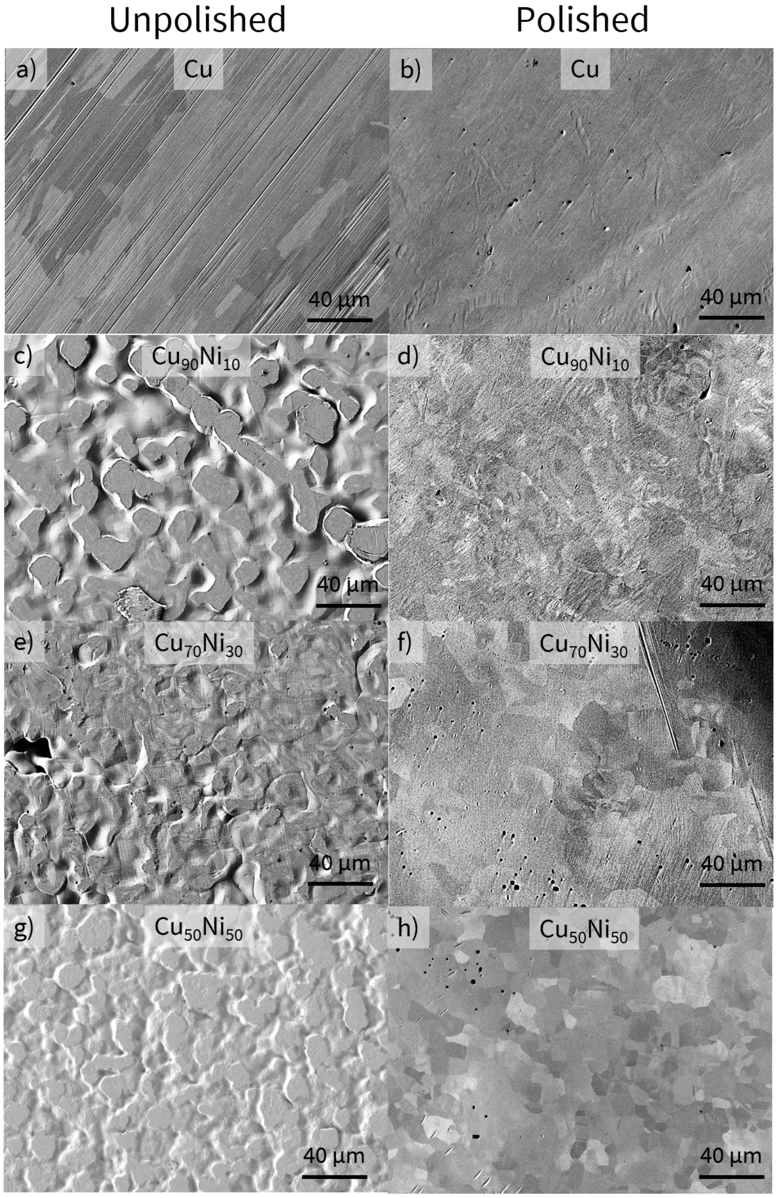

Figure 5.1: SEM micrographs of CuNi alloys before and after mechanical polishing. a) Cu, b) mechanically polished Cu, c) Unpolished CuNi10, d) Polished CuNi10, e) Unpolished CuNi30, f) Polished CuNi30, g) Unpolished CuNi50, h) Polished CuNi50.

Figure 5.2 shows the SEM micrographs of unpolished (left column) and polished (right column) NiCu alloy samples and the evolution of surface morphology of NiCu alloys. Similar to Cu, the unpolished Ni surface is extremely rough, and the rolling lines are clearly visible (Figure 5.2a). Additionally, the Ni grains are not visible due to the surface features and roughness on the Ni sample. When 10 wt.% Cu is added, the NiCu10 grain sizes become visible and the magnitude of the rolling lines dissipate (Figure 5.2c). In NiCu30 and NiCu50 samples, the surface has a pseudo-porous morphology (Figures 5.2e and 5.2f, respectively) making the native surface of the NiCu alloy unsuitable for h-BN growth. As described in the experimental methods section, the NiCu alloy samples undergo mechanical polishing identical to CuNi alloys. After polishing, the surface of Ni and NiCu samples appears very smooth revealing the microstructure (Figure 5.2a). As the Cu wt.% increases in the NiCu alloy, the grain size appears to increase in NiCu10, NiCu30, and NiCu50 (Figure 5.2d, 5.2f, and 5.2h, respectively). Unlike in CuNi alloys where the samples are susceptible to pitting from the slurry, no such behavior is observable for NiCu samples. However, NiCu50 shows a slightly abrasive surface (Figure 5.2h) after polishing. Additionally, there was no change in the stiffness of the sample with increasing Cu wt.% in the NiCu alloy.

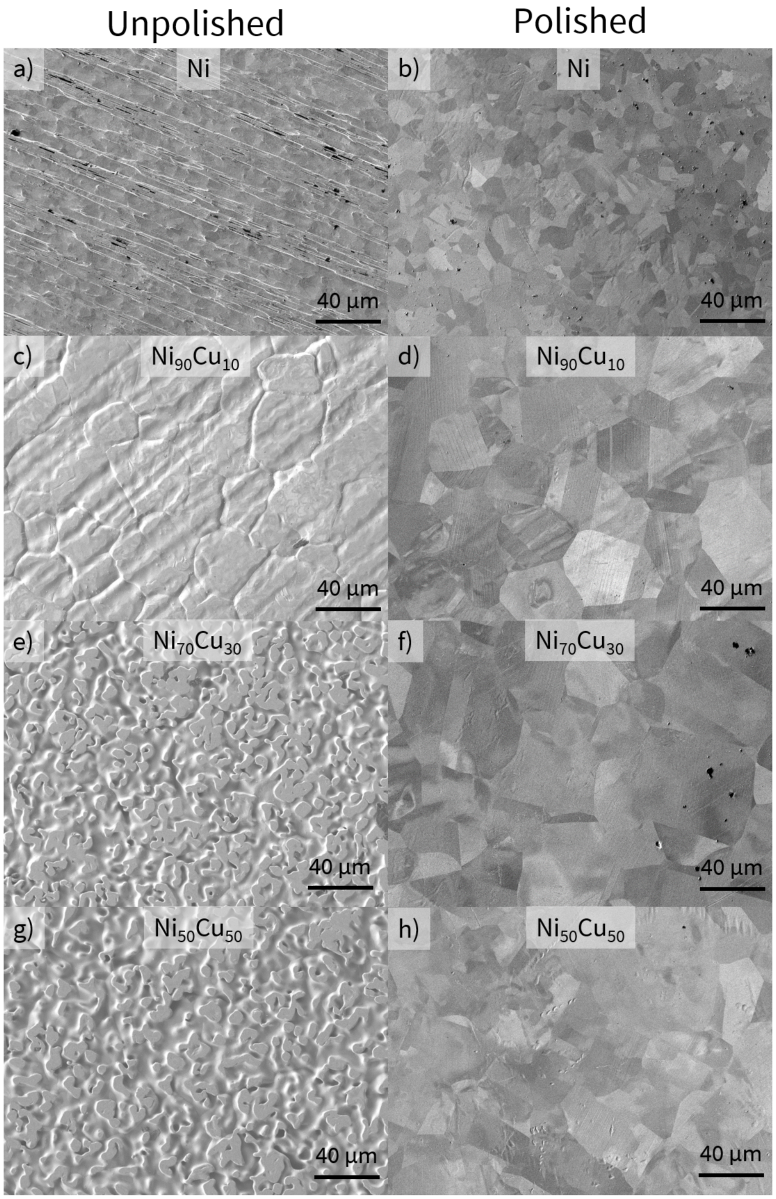

Figure 5.2: SEM micrographs of NiCu alloys before and after mechanical polishing. a) Ni, b) mechanically polished Ni, d) Unpolished NiCu10, d) Polished NiCu10, e) Unpolished NiCu30, f) Polished NiCu30, g) Unpolished NiCu50, h) Polished NiCu50.

To quantify the surface roughness after polishing, AFM was performed on CuNi30 and NiCu30 samples. Figure 5.3 shows the 10 µm $\times$ 10 µm AFM scan tapping mode AFM images of CuNi30 with phase imaging enabled. The height or the topographical image (Figure 5.3a) reveals a planarized surface in agreement with the SEM assessment of CuNi alloys (Figure 5.1). The phase image (Figure 5.3b) does not reveal major variations in phase except in the presence of polishing and scotch tape residue. This indicates a very homogenous surface finish. The residue from mechanical polishing is clearly visible as debris on both the height and the phase image. The fine lines in random directions on the height AFM image are scratch lines or comet tailing formed during mechanical polishing. The root mean square (RMS) roughness (R_q) is $\approx$3.19 nm and the average roughness (R_a) is $\approx$1.83 nm on the whole 10 µm $\times$ 10 µm AFM scan. Line profiles are also obtained at different regions from the topographical AFM image to assess the surface variations (Figure 5.3d-f). The line profiles on four different regions show low variations indicating a planarized surface. The spikes in the line profiles are the cross-sections of the polishing or tape residue. The RMS and average roughness of the line profiles are indicated in the inset of Figure 5.3d-f, which show consistency in values. The roughness of line profile 2 (Figure 5.3e) shows higher RMS roughness due to the presence of a scratch lines and residue on the surface.

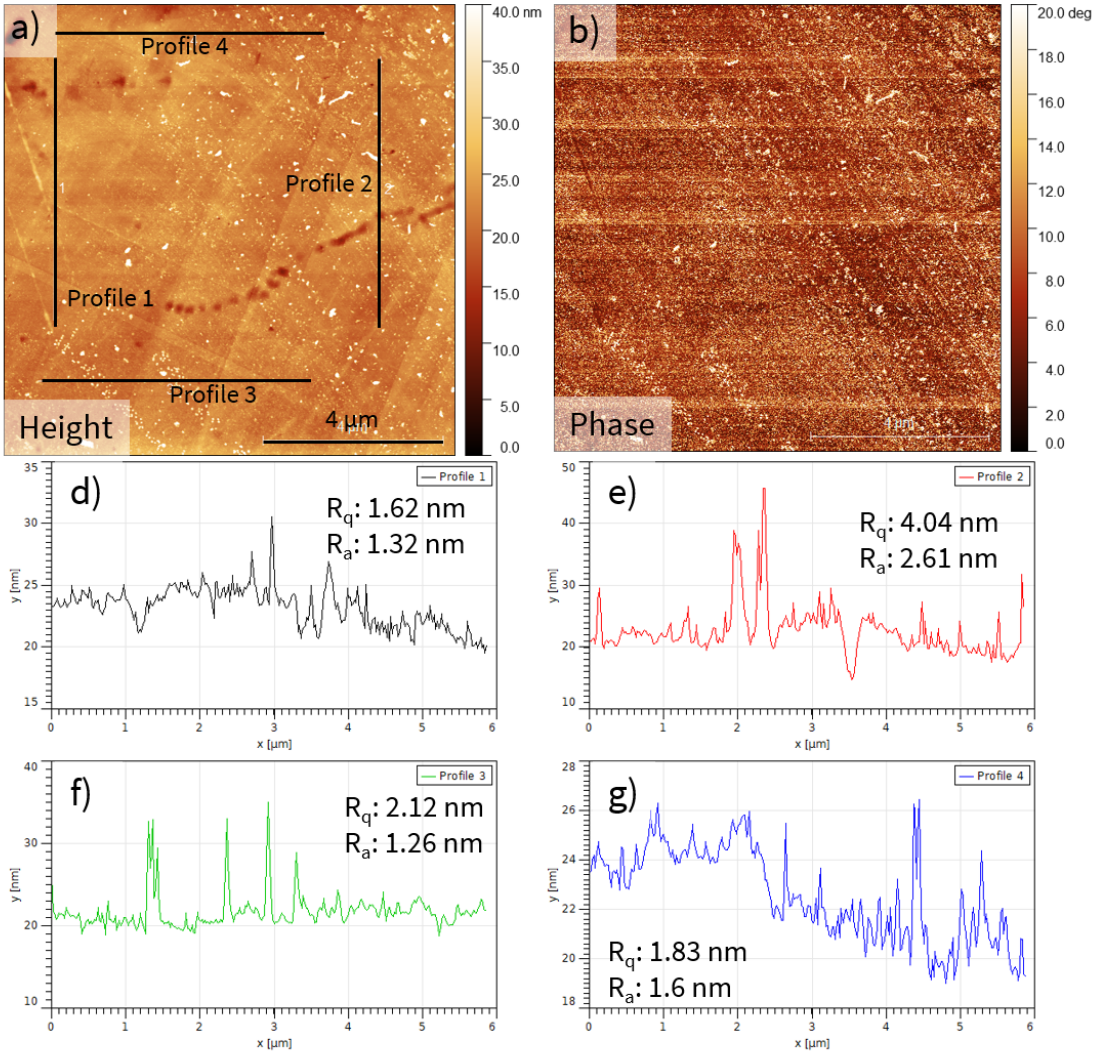

Figure 5.3: AFM image of mechanically polished CuNi30 showing a) Height, b) Phase image. d-g) shows the line profiles 1-4 from the height image in (a). The RMS (R_q) and average roughness (R_a) is 3.19 nm and 1.83 nm, respectively for a 10 µm × 10 µm AFM scan of height image shown in (a). The R_q and R_a values of the line profile are shown in the inset of (d-g).

The topography of NiCu30 is also evaluated after mechanical polishing using TM-AFM. A 10 µm × 10 µm scan is obtained with phase imaging mode enabled (Figure 5.4). The height reveals a planarized, smooth surface in agreement with SEM micrographs of NiCu alloys (Figure 5.2). The phase image (Figure 5.4b) does not show major variations in phase indicating a very homogeneous surface. Despite the uniformity in the height and phase image scans, there are bright white spots that are visible. These particles are debris from the residue during the polishing and cleaning procedures, which are also observed for CuNi30 polished samples from above (Figure 5.3). The RMS and average roughness of the whole AFM image is $\approx$3.89 nm and $\approx$1.64 nm. Line profiles in four different regions on the height AFM image (Figure 5.4d-f) show low amount of variations. The larger spikes in the line scans are the cross-sections of the polishing slurry particles and tape residue. The RMS and average roughness of the line profiles are shown in the inset of Figure 5.4d-f, which are in agreement with each other. Unlike in the polished CuNi30 sample (Figure 5.3a), the polished NiCu30 sample does not have large number of comet tails or scratches on the surface. This is due to hardness of surface caused by greater concentration of nickel in the alloy composition. The qualitative and quantitate assessment of the alloy substrate using SEM and AFM, respectively, after polishing shows a very smooth and planarized surface that is suitable for the growth of h-BN.

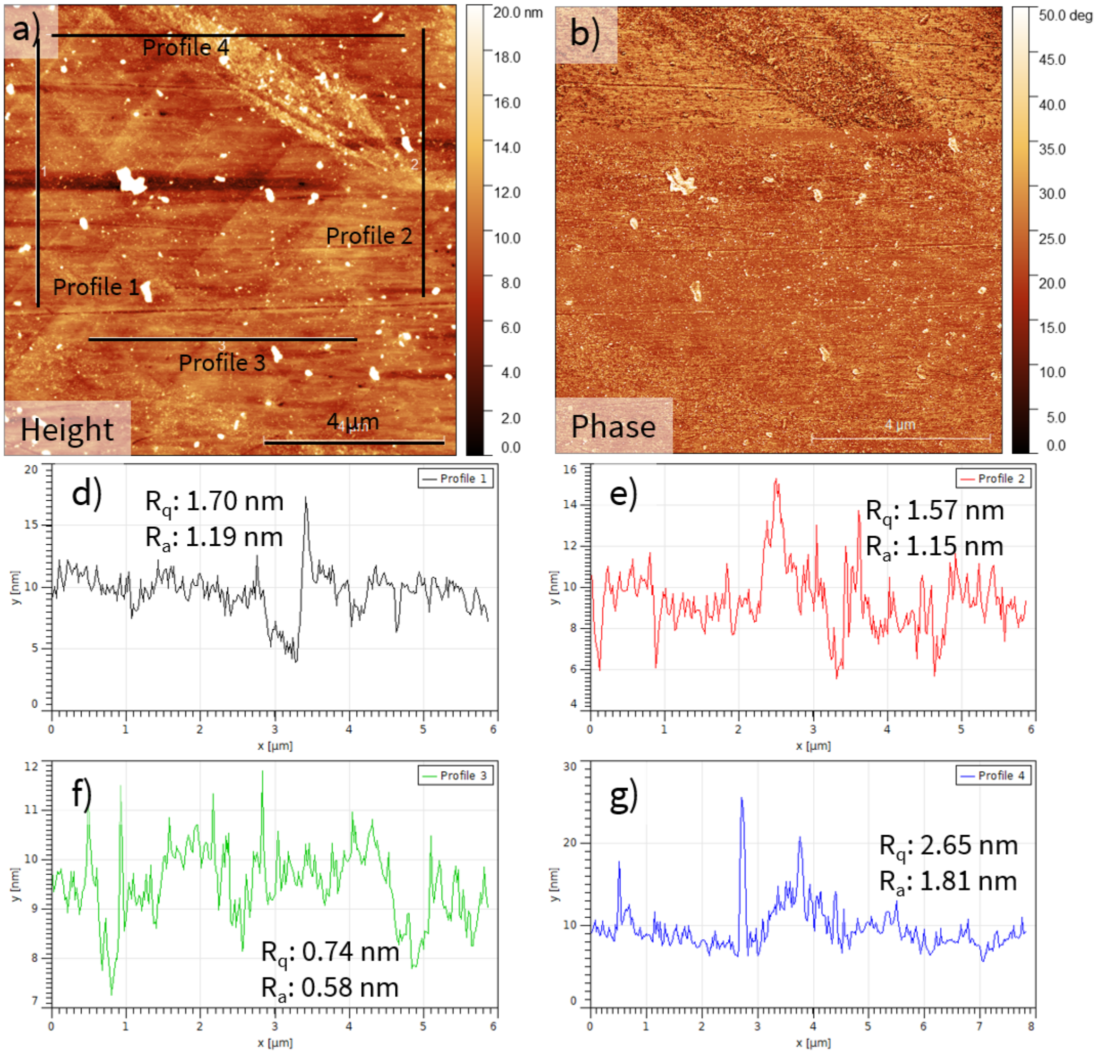

Figure 5.4: AFM image of mechanically polished NiCu30 showing a) Height, b) Phase image. d-g) shows the line profiles 1-4 from the height image in (a). The RMS (R_q) and average roughness (R_a) is 3.89 nm and 1.64 nm, respectively for a 10 µm × 10 µm AFM scan of height image shown in (a). The R_q and R_a values of the line profile are shown in the inset of (d-g).

5.2.2 Compositional analysis of alloy substrates

EDX maps are obtained before and after polishing to ensure that mechanical polishing did not alter the composition of the alloys (Figure 5.5). EDX confirms complete miscibility of Cu and Ni species in the alloy, indicating an absence of Ni-rich and Cu-rich regions. Figure 5.5a shows the SEM micrograph of unpolished CuNi30 alloy; the morphological features on the CuNi30 alloy surface are clearly seen as the surface is not smooth. EDX maps of Ni and Cu species (Figure 5.5b and 5.5c) show that Ni and Cu species are equally distributed areally on the sample without any noticeable Ni and Cu-rich regions. The SEM micrograph of a polished CuNi30 alloy (Figure 5.5d) shows a smoother surface than unpolished CuNi30 alloy (Figure 5.5a). The Ni and Cu species are also equally dispersed in the polished CuNi30 sample and there are no Ni-rich or Cu-rich regions visible. This confirms that mechanical polishing is not selectively etching Ni or Cu species and is a purely physical process, where the rougher features on the surface are removed. According to the EDX point spectra, the unpolished CuNi30 alloy (Figures 5.5g) has a composition of 77 wt.% of Cu and 23 wt.% of Ni. However, the polished CuNi30 alloy (Figures 5.5h) shows a much more balanced stoichiometry of 72 wt.% of Cu and 28 wt.% of Ni.

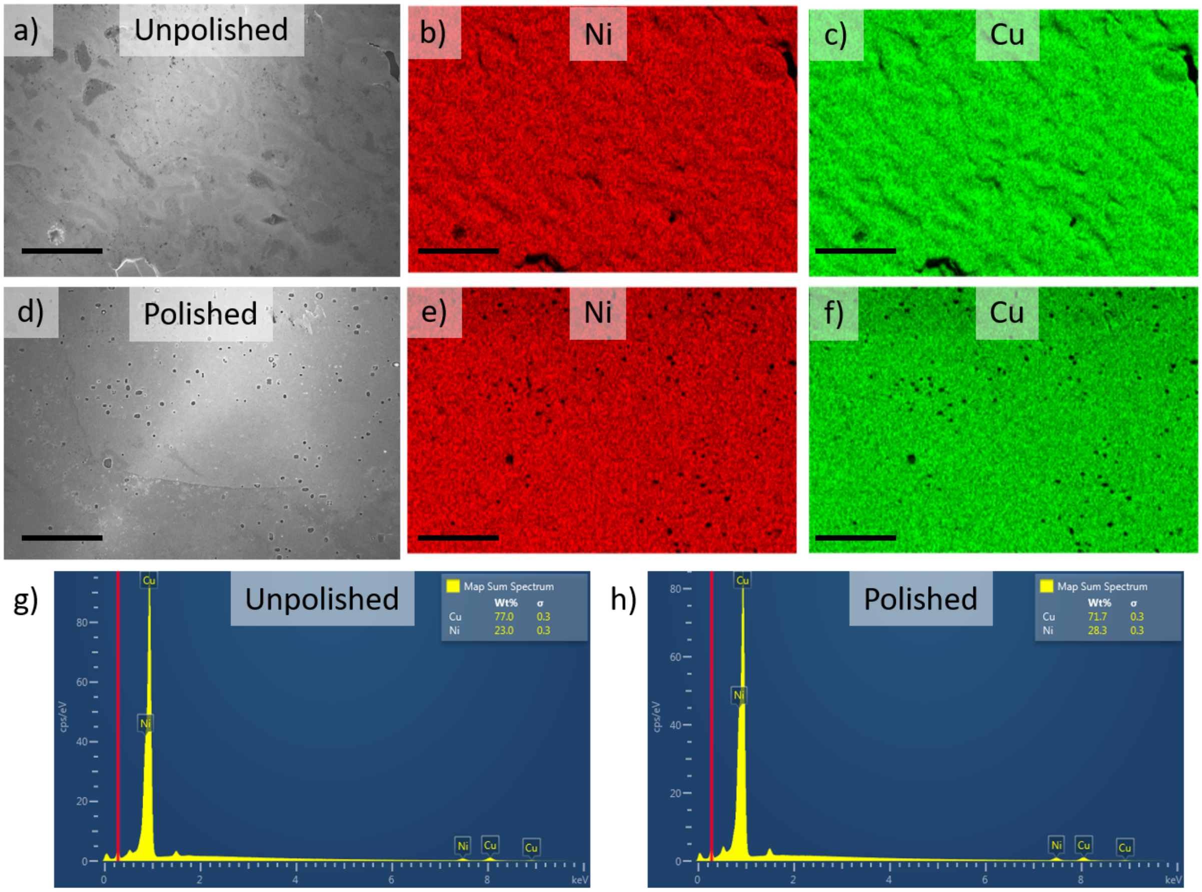

Figure 5.5: a) SEM micrograph of EDX region of unpolished CuNi30 map, b) EDX map of Ni distribution from (a), c) EDX map of Cu distribution from (a), d) SEM micrograph of polished CuNi30 alloy, e) EDX map of Ni distribution from (d), f) EDX map of Cu distribution from (d), g) EDX point spectra of unpolished CuNi30 sample, h) EDX point spectra of polished CuNi30 sample. The scale bar is 50 µm.

Figure 5.6 shows the EDX maps of NiCu30 alloy before and after mechanical polishing, along with SEM micrographs of the mapped regions. Figure 5.6a shows the SEM micrograph of NiCu30 alloy sample, which reveals surface features that are also reflected in the compositional maps of Ni and Cu (Figures 5.6b and 5.6c). In both the Ni and Cu compositional maps, there were no Ni or Cu-rich regions observed. The SEM micrograph of the polished NiCu30 alloy (Figure 5.6d) is extremely planarized without any surface abnormalities. The Ni EDX map (Figure 5.6e) shows an even distribution of Ni in the alloy sample. However, the Cu compositional map (Figure 5.6f) reveals brighter and darker green regions indicating a presence of Cu-rich regions. The Cu-rich regions, which are observed at the alloy grain boundaries, can be ascribed to the diffusion of Cu along the Nickel grain boundaries as reported by Barnes [257]. EDX point spectra of the composition of the NiCu30 alloy sample before and after polishing (Figures 5.6g and 5.6f, respectively) show a slightly Cu-rich region in unpolished NiCu30 samples, where the composition of Ni is 61 wt.% and Cu is 39 wt.%. As also observed with EDX of CuNi alloy, the stoichiometry of polished NiCu30 alloy sample is more balanced, where Ni is 70 wt.% and Cu is 30 wt.% in composition.

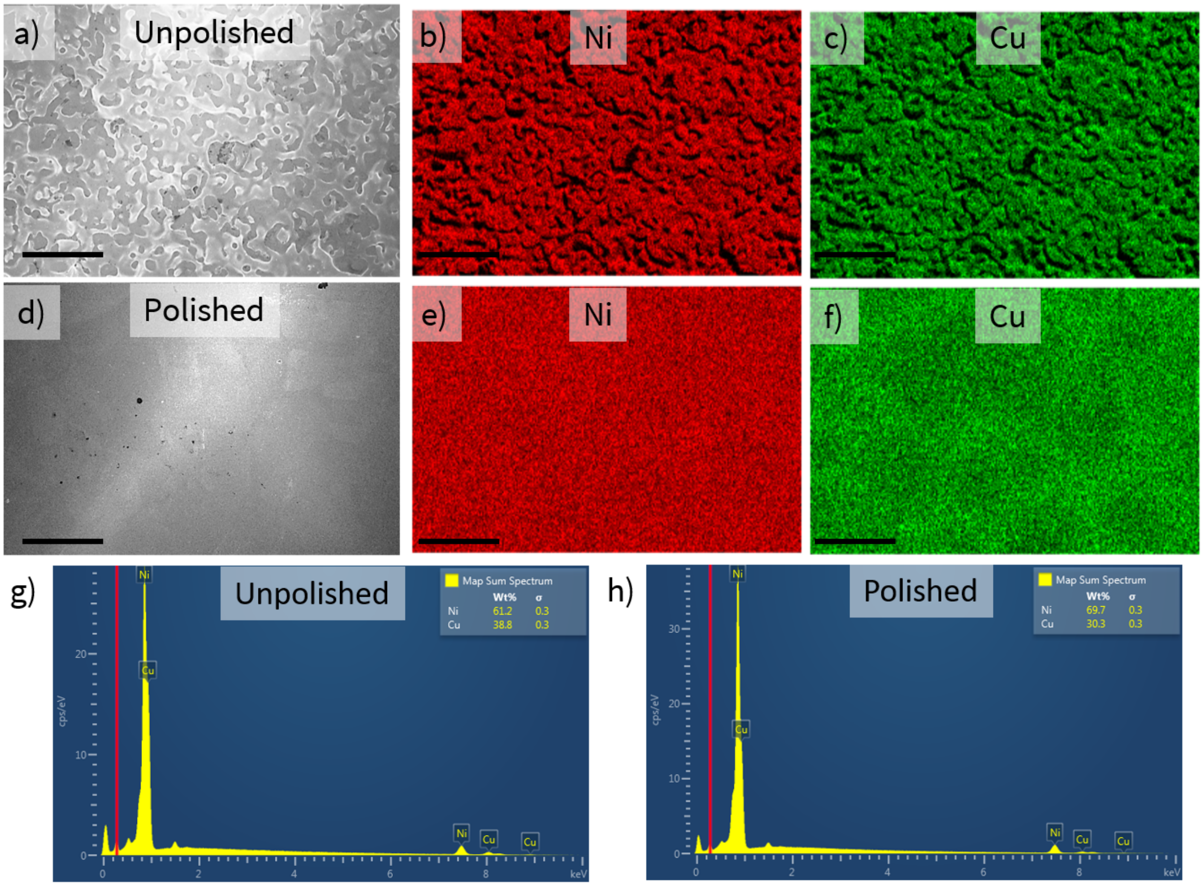

Figure 5.6: a) SEM micrograph of EDX region of unpolished NiCu30 map, b) EDX map of Ni distribution from (a), c) EDX map of Cu distribution from (a), d) SEM micrograph of polished NiCu30 alloy, e) EDX map of Ni distribution from (d), f) EDX map of Cu distribution from (d), g) EDX point spectra of unpolished NiCu30 sample, h) EDX point spectra of polished NiCu30 sample. The scale bar is 50 µm.

5.2.3 Microstructural analysis of alloy substrates

The microstructure of the Cu-Ni alloy system is probed using EBSD to understand the dominant grain orientation of the alloy and to assess the grain statistics, mainly the grain size evolution with respect to alloy composition. EBSD maps are obtained for both CuNi and NiCu alloy samples, along with the control samples: Cu and Ni. Figure 5.7 shows the EBSD maps of Cu and CuNi alloys, along with the inverse pole figure reference for the grain orientations. EBSD maps were obtained only on mechanically polished samples to avoid artefacts and poor indexing that may arise from a rougher surface. Figure 5.7a shows the EBSD map of the vendor supplied Cu (99.999% pure) with grains in the order of 20-50 μm in size and non-preferential grain orientations. After thermal annealing, the grain size increases to >200 μm (Figure 5.7b) and are predominantly (100)-like orientation, which is also reported in the literature [254]. There is also a noticeable amount of twin grains present in the thermally annealed Cu. The CuNi10 alloy (Figure 5.7c) consistently showed poor indexing during EBSD, limiting the ability to obtain the grain size statistics; the grain sizes from the SEM micrographs are approximately 50-70 μm. CuNi30 alloy (Figure 5.7d) has a dominant (100)-like crystal structure with grain sizes in the order of 30-50 μm for the CuNi30 alloy (Figure 5.7b). The grain size decreases to 20-30 μm for CuNi50 alloy (Figure 5.7e). Unlike CuNi10 and CuNi30 alloy, CuNi50 does not have a dominant (100)-like grain orientation (Figure 5.7e). Both the EBSD maps and SEM micrographs show decreasing grain sizes of the CuNi alloys with increasing Ni.

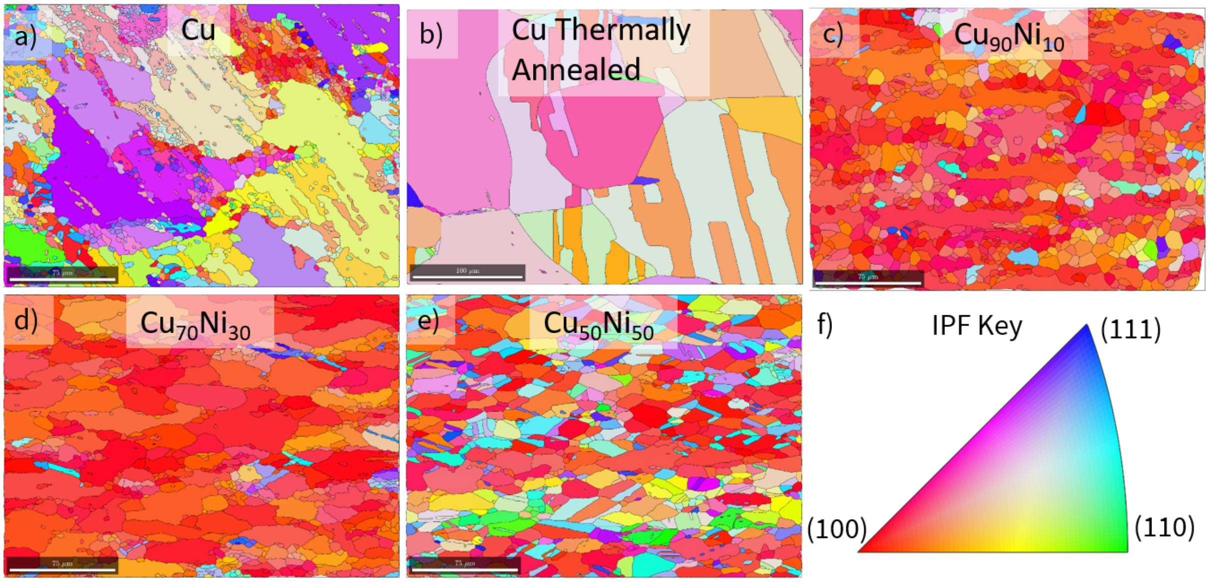

Figure 5.7: EBSD maps of Cu and CuNi alloys. a) Vendor supplied Cu, b) Cu thermally annealed and electropolished, c) CuNi10, d) CuNi30, e) CuNi50, f) IPF reference. The scale bar is 75 µm for all. Scale bar for (b) is 100 µm.

Figure 5.8a shows the EBSD map of Ni control sample, which reveals grains of untextured (random orientation) with a grain size of ≈10-20 µm. After thermal annealing of Ni, the grain size increased to ≈30-50 µm while retaining the untextured grain orientation (Figure 5.8b). Similar to Cu, twin grains are formed in Ni after thermal annealing. The grain size appears to increase marginally with increasing Cu concentration as observed in NiCu10, NiCu30, and NiCu50 alloys (Figures 5.8c, 5.8d and 5.8e, respectively). The grain sizes of NiCu10, NiCu30, and NiCu50 alloys are revealed to be ≈30 µm, 33 µm, and 34 µm, respectively, which are obtained from the EBSD analysis performed using Mtex software library [258]. Similar to the thermally annealed Ni sample, twin grains are observable in the NiCu alloys (Figures 5.8c, 5.8d, and 5.8e). There were no dominant grain orientations observed on all the NiCu alloy samples.

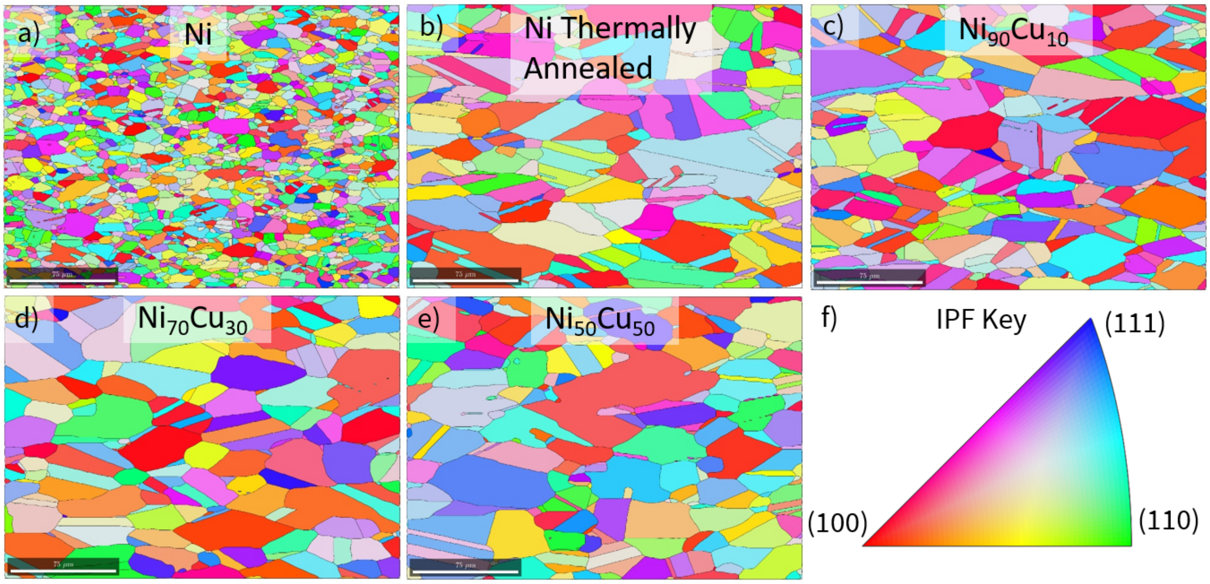

Figure 5.8: EBSD maps of Ni and NiCu alloys. a) Vendor supplied Ni, b) Ni thermally annealed and mechanically polished, c) NiCu10, d) NiCu30, e) NiCu50, f) IPF reference. The scale bar for all the samples is 75 µm.

5.2.4 Summary of Cu-Ni binary alloy substrate characterization

The Cu-Ni alloys are characterized using SEM, EDS and EBSD to understand the surface morphology, chemical composition, and microstructure of the alloy, respectively. The surface morphology of the alloys is riddled with features such as voids and porous-like structure. However, after mechanical polishing, the surface features disappear, and the alloy grains are revealed on the surface. The EDS analysis shows that there are no strong Cu-rich and Ni-rich regions in the alloys. Additionally, the stoichiometry of the alloys is much more balanced after polishing. The EBSD data reveals the grain size and orientations of the alloys. The Cu-rich alloys have a (100)-like orientation and the grain size decreases with increasing Ni concentration. The Ni-rich alloys are untextured (random orientation) and the grain size increases with increasing Cu concentration.

5.3 Growth of h-BN on Cu-Ni alloys: General Trend

During the initial trial runs, CVD growth of h-BN is performed on unpolished CuNi and NiCu alloy to assess whether h-BN can be grown on the complete alloy and to identify the general trend in h-BN growth using FT-IRRAS. Figure 5.9 shows a complete summary of FT-IRRAS spectra of h-BN grown on CuNi and NiCu (Figures 5.9a and 5.9b, respectively) alloy along with the Cu and Ni control samples. The peak intensity of A$_{2U}$ (LO) vibrational mode at 823 cm^{-1} is used for comparative analysis. On CuNi alloys, there is an h-BN peak at 823 cm^{-1} across all the samples. CuNi10-30 alloys have a similar peak intensity as Cu indicating comparable amount of h-BN growth. However, there is a significant drop in the peak intensity on CuNi40 and CuNi50 samples indicating slower growth on CuNi40 and CuNi50. There is no visible pattern of h-BN peak intensity on the CuNi alloy samples as there is no gradual increase or decrease of h-BN intensity observable with increasing Ni concentration.

A similar analysis is also performed for NiCu alloy samples (Figure 5.9b). Ni and Cu were used as control samples for NiCu alloys, primarily to confirm multilayer h-BN growth, which can be approximated from FT-IRRAS peak intensities of Cu and Ni. Figure 5.9b shows that Ni has a much higher peak intensity than Cu, indicating multilayer h-BN growth. However, after adding 10 wt.% of Cu in Ni (NiCu10), there is an increase in the peak intensity of h-BN at 823 cm^{-1} (Figure 5.9b). Upon increasing the Cu concentration (from 10 wt.% to 50 wt.%), the peak intensity of h-BN gradually decreases indicating lower amount of h-BN growth on the alloy surface.

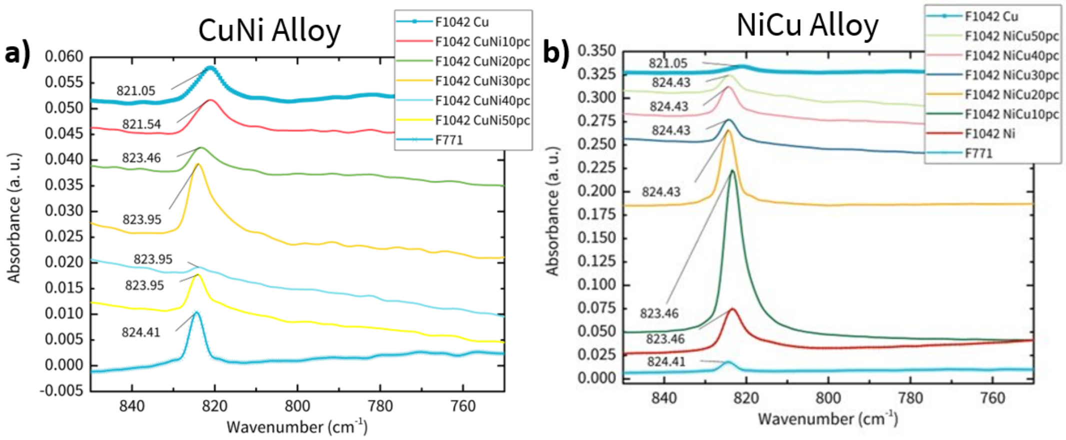

Figure 5.9: FT-IRRAS spectra of a) h-BN grown on CuNi and b) h-BN grown on NiCu alloys.

To assess the growth pattern of h-BN on the Cu-Ni alloys, the integrated peak area of h-BN at 823 cm^{-1} is calculated and plotted against Cu wt.% for both CuNi and NiCu (Figure 5.10a). The peak area of FT-IRRAS is proportional to the total amount of h-BN on the surface. A growth pattern of h-BN is clear when plotted against Cu wt.% from 0 wt.% to 100 wt.% (Figure 5.10a). There is an increase in peak area from 0 wt.% to 10 wt.% Cu. With subsequent increases in Cu wt.% (10-50 wt.%), a gradual decrease in the integrate peak intensity of h-BN on NiCu alloy samples is observable. There is a sudden drop at the 50 wt.% of Cu (NiCu50 alloy) and 50 wt.% Ni (in CuNi50 alloy); further discussion of this phenomenon is presented in the last subsection (Section 5.6). Both CuNi50 and CuNi40 show a similar growth pattern, where there is a low amount of h-BN in comparison with Cu implying a slower growth rate of h-BN. On CuNi30 alloy sample, there is an increase in the amount of h-BN and in the subsequent alloys, CuNi20 and CuNi10, there is a lower amount of h-BN than CuNi30 and Cu, the control sample.

To crosscheck the growth pattern from FT-IRRAS peak area analysis, XPS is performed and B 1s peak area is used for comparative analysis (Figure 5.10b). B 1s peak is used to assess the amount of h-BN as N 1s peak area can be distorted by nitrogen in the ambient atmosphere. The growth trend of h-BN appear to be very similar between FT-IRRAS peak area and XPS B 1s data. On NiCu alloys, there is an inverse relationship between increasing Cu wt.% and decreasing in

B 1s peak implying a decreasing amount of h-BN. The sudden dip in the amount of h-BN at the 50 wt.% intersection for NiCu50 and CuNi50 is also observable in the FT-IRRAS spectra. Additionally, CuNi30 alloy shows the highest amount of h-BN amongst all the CuNi alloys. To better understand the growth behavior of h-BN on the alloys, CuNi and NiCu alloys are analyzed separately using SEM to understand and relate to the FT-IRRAS and XPS spectroscopy results.

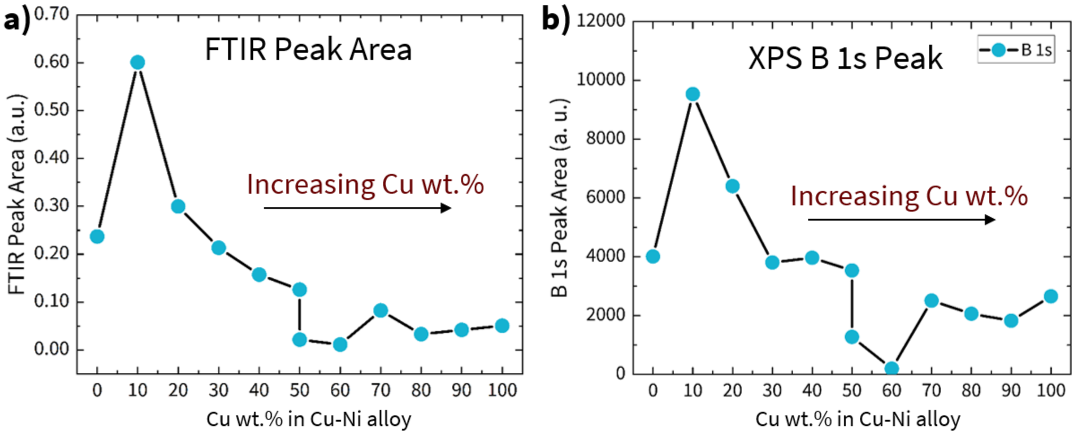

Figure 5.10: a) FT-IRRAS peak area, b) XPS B 1s peak area of h-BN on Cu-Ni alloys from 0-100 wt.% of Cu.

5.4 Growth of h-BN on $Cu_{1-x}Ni_x$

To correlate the alloy composition to h-BN growth morphology, both spectroscopic (FT-IRRAS and XPS) and microscopic (SEM) techniques are utilized. From the FT-IRRAS and XPS data (Figure 5.11a and 5.11b, respectively), the growth pattern is classified into two categories: lighter alloy and heavier alloy. The lighter alloy has a composition of <20 wt.% of Ni (CuNi10 and CuNi20) and heavier alloy has a composition of >20 wt.% (CuNi30, CuNi40 and CuNi50). The lighter alloys have a lower amount of h-BN than Cu. However, the heavier alloy (CuNi30) shows much higher amount of h-BN. Additionally, CuNi40 and CuNi50 alloys have the lowest amounts of h-BN of all the CuNi alloys.

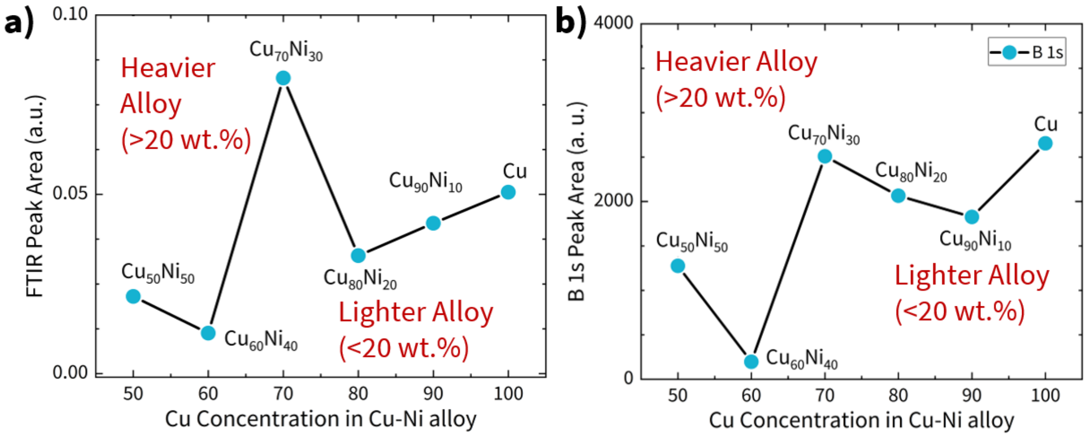

Figure 5.11: a) FT-IRRAS peak area, b) XPS B 1s peak area of CuNi alloys from 50 to 100 wt.% of Cu.

5.4.1 SEM of h-BN growth on CuNi alloys

SEM is performed to understand and correlate h-BN growth with the spectroscopic results. Firstly, SEM is used to highlight the impact of surface preparation (mechanical polishing) on h-BN growth on CuNi alloys. Secondly, SEM is used to assess the growth behavior of h-BN across various alloy compositions and growth conditions. Figure 5.12a and 5.12b show h-BN growth on unpolished and mechanically polished Cu samples, respectively. The secondary nucleation on both unpolished and polished samples appears as bright white regions on the h-BN film. There is also a marginal increase in the h-BN film grain size in the mechanically polished Cu from ≈1 µm to ≈2 µm. There is also an increase in the film grain size on unpolished CuNi10 alloy (≈2 µm) in comparison with unpolished Cu. Although the unpolished alloy (Figure 5.12c) shows a marginal increase in the h-BN grain size, the polished CuNi10 alloy (Figure 5.12d) shows substantial increase in the grain size of the h-BN film from ≈2-3 µm to nearly ≈10 µm. On the unpolished CuNi30 alloy (Figure 5.12e), there is a complete film of h-BN with substantial amount of secondary nucleation. However, on the polished CuNi30 alloy (Figure 5.12f), there are h-BN crystals present and there is a low amount of secondary nucleation. The isolated h-BN crystals observed on polished CuNi30 alloys were also larger (10 µm) than on Cu film grains size (1-2 µm).

There is an h-BN film with small amounts of secondary nucleation observable on unpolished CuNi50 alloy (Figure 5.12g) and isolated h-BN crystals with little or no secondary nucleation on polished CuNi50 alloy (Figure 5.12h).

The growth trend from the SEM micrographs of the CuNi alloy samples show that with increasing Ni wt.% in the CuNi alloy, the amount of h-BN decreases. The transition of completely covered h-BN film on CuNi10 alloy to a quasi-film on CuNi30 alloy and finally to isolated h-BN crystals on CuNi50 alloy validates the statement. The h-BN crystal and film coalescence also improves with increasing Ni wt.% in the CuNi alloy. This is substantiated by the lack of a well-defined h-BN grain boundaries, which is evident on the lighter CuNi10 alloy. The grain boundaries of h-BN film are almost nonexistent on the quasi-film growing on heavier CuNi30 alloy. Therefore, using heavier CuNi alloys can mitigate poor coalescence of h-BN film on Cu substrates. Additionally, the presence of secondary nucleation of h-BN on both unpolished and polished CuNi30 samples (Figures 5.12e and 5.12f) causes an increasing in the amount of h-BN in FT-IRRAS and XPS analysis on CuNi30 alloy. The formation of isolated h-BN crystals on CuNi50 alloy without any secondary nucleation causes a subsequent decrease in the amount of h-BN in the FT-IRRAS and XPS peak area for CuNi50 alloy. The heavier CuNi alloys also appear to be less susceptible to agglomeration of monomeric aminoborane particles, which impede film continuity and are commonly observable on Cu substrates [140]. By combining and correlating the FT-IRRAS, XPS and SEM characterization, the h-BN growth behavior on lighter (<20 wt.%) and heavier (>20 wt.%) CuNi alloy are distinct. However, closer inspection of h-BN growth on CuNi20 alloy reveals a transitionary nature of both lighter and heavier alloys.

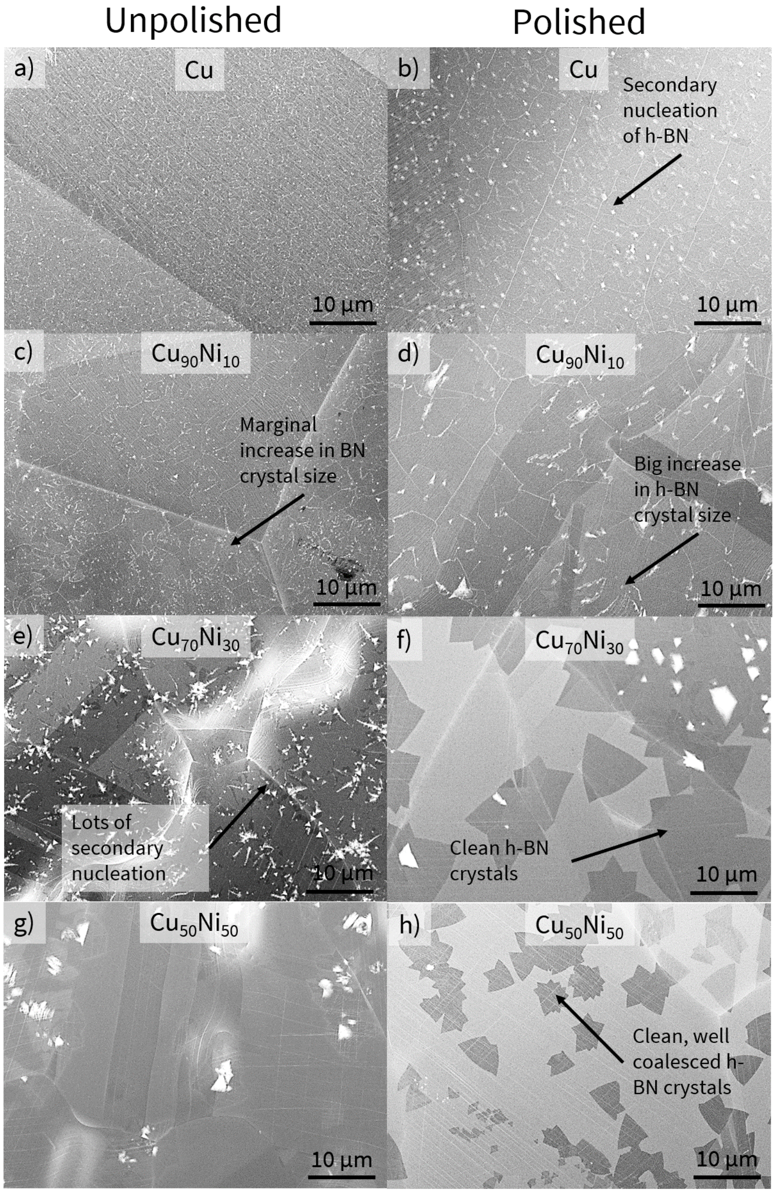

Figure 5.12: SEM micrographs of h-BN growth on Cu before (a) and after polishing (b). h-BN growth on CuNi10 before (c) and after polishing (d). h-BN growth on CuNi30 before (e) and after polishing (f). h-BN growth on CuNi50 before (g) and after polishing (h).

Figure 5.13 shows the SEM micrographs of CuNi10, 20, and 30 alloys for two different growth conditions: growth A with a precursor flow rate of 40 sccm (left column) and growth B with a precursor flow rate of 60 sccm (right column). Growth trends in growth A indicate a complete h-BN film growing on CuNi10 alloy (Figure 5.13a). However, on CuNi20 (Figure 5.13c) and CuNi30 (Figure 5.13e) alloys show growth of a quasi-film of h-BN. Growth B shows a complete h-BN film growing on CuNi10 alloy sample (Figure 5.13b) with considerable amount of secondary nucleation. CuNi20 alloy sample (Figure 5.13d) also shows a similar growth behavior as CuNi10 alloy sample with complete h-BN film and secondary nucleation. This is distinct from CuNi30 alloy sample (Figure 5.13f), where isolated h-BN crystals are observable. The SEM characterization reveals that the CuNi20 alloy substrate is transitionary in nature exhibiting the h-BN growth pattern of both lighter and heavier alloys. This also suggests that the by fine tuning the growth conditions CuNi20 alloy can be used to growth isolated h-BN crystals, quasi-films or complete films with significantly larger h-BN crystal size than on Cu.

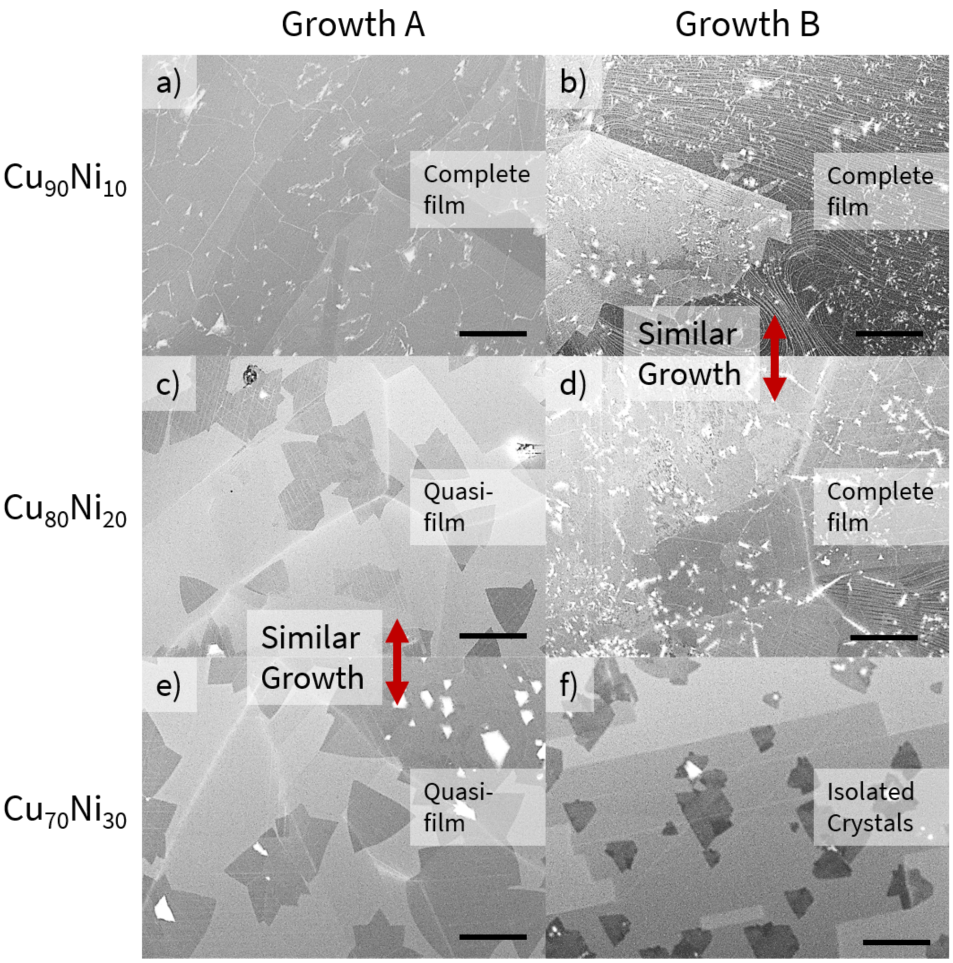

Figure 5.13: Growth of h-BN on CuNi20 alloy showing tendencies of both heavier alloy in growth A conditions and lighter alloy in growth B conditions. a) and b) h-BN on CuNi10 from growth A and B, c) and d) h-BN on CuNi20 on growth A and B, e) and f) h-BN on CuNi30 from growth A and B. The scale bar is 10 µm.

The SEM micrographs of h-BN growth on two different alloy compositions from two different growth conditions are obtained (Figure 5.14) to show the impact of alloy composition and flow rate on h-BN growth. A precursor flow of 50 sccm and 40 sccm is used for the alloy samples (Figures 5.14a and 5.14b, and Figures 5.14c and 5.14d, respectively). CuNi40 alloy (Figure 5.14a) has a complete h-BN film growing whereas CuNi20 alloy has a quasi-film growth (Figure 5.14b). Reducing the flow rate from 60 to 40 sccm on CuNi40 and CuNi20 alloys show a quasi-film and isolated h-BN crystals growing, respectively (Figures 5.14c and 5.14d). The SEM results demonstrate the versatility of CuNi alloy substrates, where the alloy composition along with the growth parameters can be tuned to grow desirable h-BN: monolayer crystals or films.

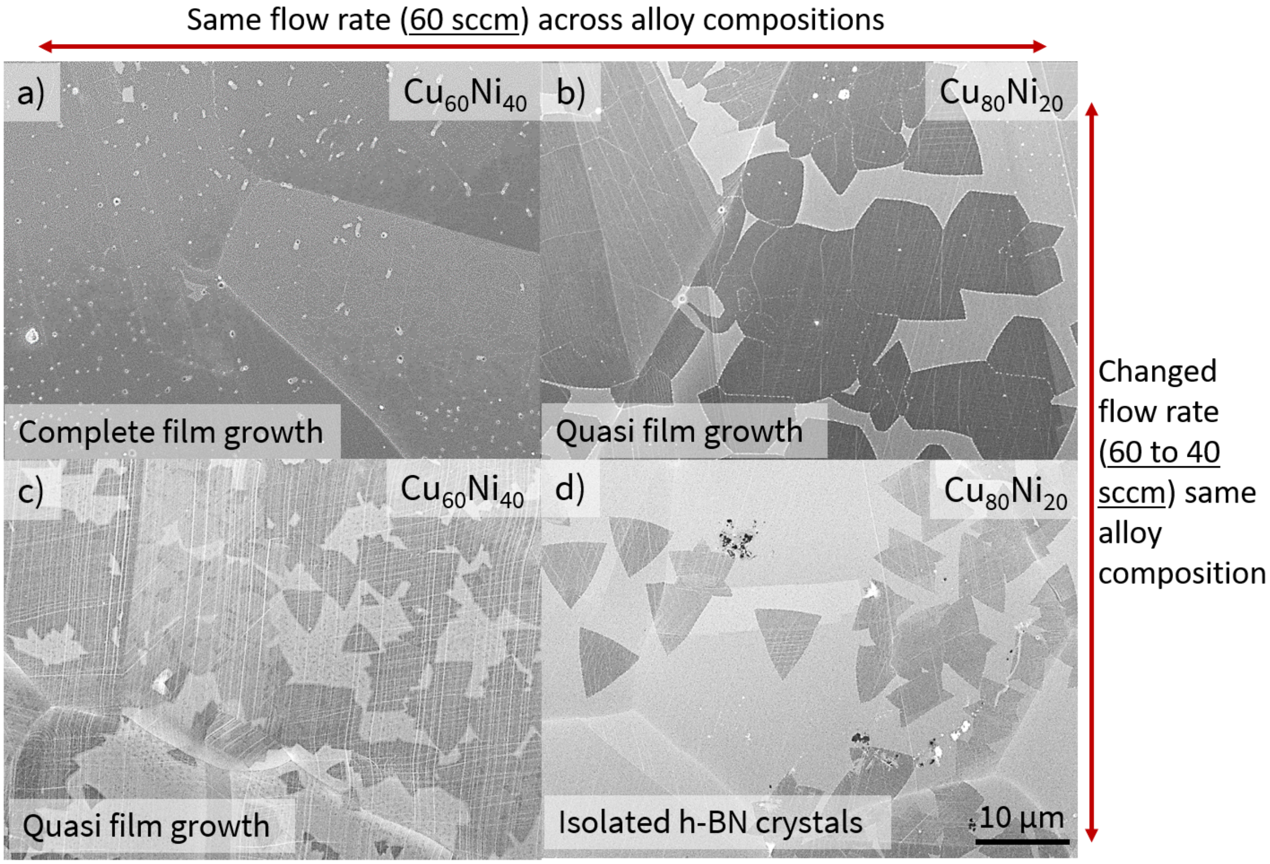

Figure 5.14: SEM micrographs of h-BN growth on two different CuNi alloy compositions and two different flow rates. a) h-BN on CuNi40 and b) CuNi20 grown with a precursor flow rate of 60 sccm. c) h-BN on CuNi40 and d) CuNi20 alloy grown with a precursor flow rate of 40 sccm.

5.4.2 Characterization of CuNi alloy surfaces after h-BN growth

XPS is performed on CuNi alloys after h-BN growth to provide a preliminary insight into the role of Cu and Ni in controlling h-BN growth. The Cu and Ni catalytic activity can be assessed by the oxidation state of these elements from the Cu and Ni peaks. Figures 5.15a and 5.15b show the Ni 2p and Cu 2p regions of all the CuNi alloy samples along with the Cu control sample. Figures 5.15c and 5.15d show the truncated and magnified plot of the Ni 2p and Cu 2p regions. The truncated plots identify the oxidation states from the variation in the satellite peaks of both Ni and Cu for all the Cu and CuNi alloy samples.

The dashed vertical lines indicate the primary peaks of Ni 2p, Ni 2p$^{3/2}$ and Ni 2p$^{1/2}$ (Figures 5.15a and 5.15c). The presence of Ni 2p$^{3/2}$ and Ni 2p$^{1/2}$ peaks at 852.7 eV and 870 eV, respectively, indicate a pure Ni surface [259]. However, on CuNi10 and CuNi20 alloys, there is a small Ni (Ni 2p$^{3/2}$) metal peak at $\approx$852.7 eV and a secondary peak at $\approx$856.5 eV, indicating the presence of Ni(OH)$_2$ (Figure 5.15c) [260, 261, 262]. The Ni(OH)$_2$ peak is also much larger in intensity than Ni 2p$^{3/2}$ peak implying the presence of oxidized Ni species on CuNi10 and CuNi20 alloy surfaces. This phenomenon is not as pronounced in CuNi30-50 alloys, where the Ni 2p$^{3/2}$ metal peak is much greater in intensity than the Ni(OH)$_2$ peak [260, 261, 262]. This indicates that the Ni atoms in CuNi10 and 20 alloys have a different chemical environment (bonding). They exist more prominently on the surface and hence, are more oxidized than CuNi30-50 alloys. This also demonstrates that Ni is playing a more active role in CuNi10 and CuNi20 alloys, contributing to a faster lateral growth of h-BN than in CuNi30-50 alloys as observed using SEM.

The Cu 2p$^{3/2}$ and 2p$^{1/2}$ peak are indicated at $\approx$933 eV and 953 eV, respectively using dashed lines (Figure 5.15b). The satellite peaks for the Cu control substrate and CuNi10 alloy (blue) show that they are slightly higher in binding energy than CuNi20 alloy (yellow). This indicates that the surface of Cu and CuNi10 is Cu$_2$O has a +1 oxidation state [263, 264, 265, 266, 267, 268]. However, the CuNi20-50 alloys have satellite peaks lower than Cu along with the presence of a shoulder peak on Cu 2p$^{3/2}$ (Figures 5.15b and 5.15d). The satellite peaks and the shoulder peak, which are more prominently observable in CuNi20 alloy, indicate that the surface of CuNi20-50 alloys is a Cu(OH)$_2$ and CuO complex oxide, having a +2 oxidation state [215]. The CuNi30 alloy (green) does not show the Cu satellite peaks indicating either the formation of Cu(I)O or Cu(II)O species, and the Cu 2p spectra is more metal-like [263, 264, 265, 266, 267, 268]. The XPS analysis of Ni and

Cu indicate that Ni plays an active role in precursor breakdown in CuNi10 and CuNi20 alloys as it is observed to readily oxidize. However, in CuNi30-50 alloys, Ni plays a passive role as the amount of Ni oxide species reduces relative to the Ni species.

From the FT-IRRAS, SEM, and XPS analyses, the following is theorized on the differences in h-BN growth on the CuNi alloys. h-BN growth on CuNi10 alloy is similar to Cu as both of them have a very similar Cu oxidation state. Ni takes an active role, facilitating an increase in the h-BN film grain size. h-BN growth on CuNi20 alloy has a more transitional behavior as observed under SEM because of the prominence of Cu(II) oxide and Ni taking an active role. FT-IRRAS and XPS on CuNi30 alloy reveals an increase in the amount of h-BN. This can be explained using the Cu 2p XPS peak, which reveals that the Cu species are not oxidized but the Ni species are oxidized, indicating a prominence of Ni on the alloy surface. CuNi40 and CuNi50 alloys show a similar h-BN growth pattern, where isolated h-BN crystals or quasi-film are observed, as both these alloys have similar Ni and Cu XPS peaks.

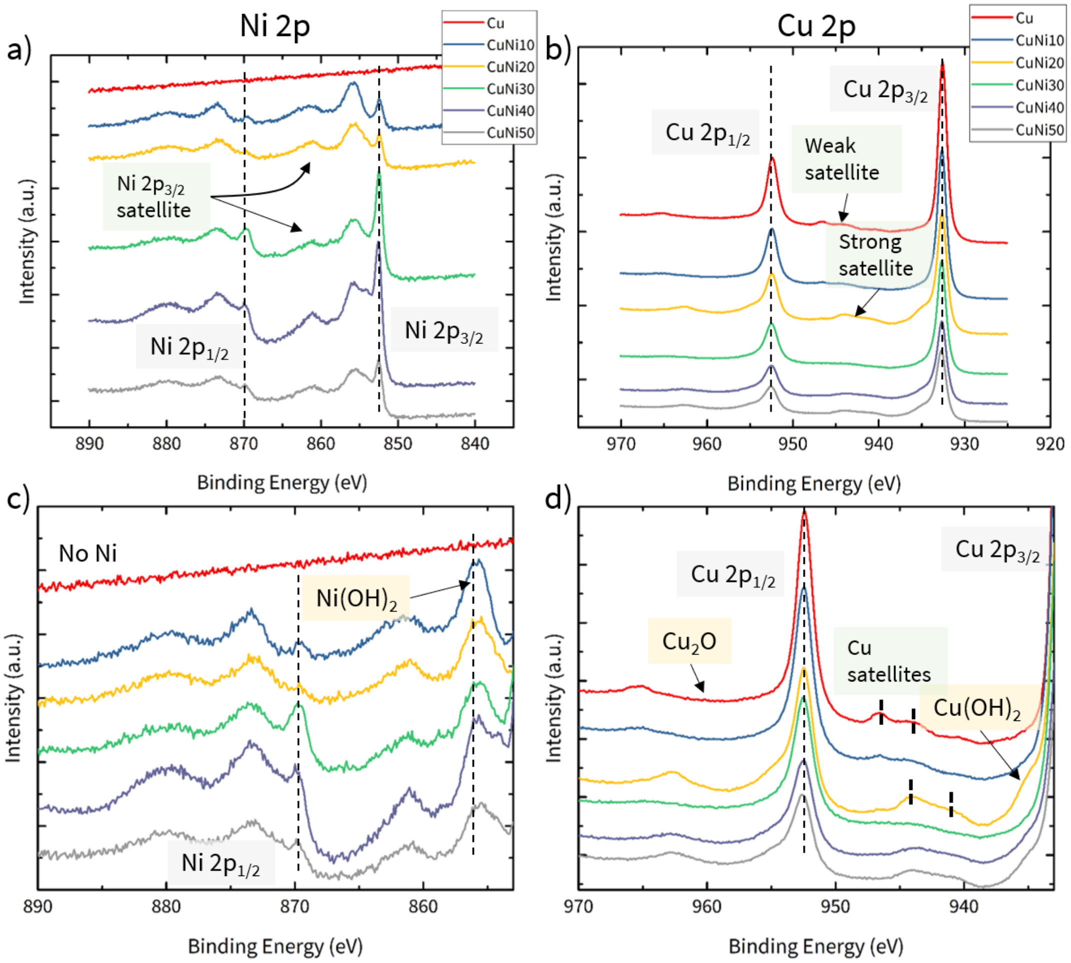

Figure 5.15: XPS analysis of CuNi alloys. a) Ni 2p, b) Cu 2p, c) Ni 2p region limited to 850-890 eV, d) Cu 2p region limited to 930-970 eV. The legend for a and c, b and d are the same.

5.4.3 Summary of h-BN growth on CuNi alloys

This work demonstrates the growth of h-BN on CuNi alloy substrates which produce well- coalesced monolayer h-BN crystals and quasi-films with large film grain size (5-10 µm). The growth pattern of h-BN on CuNi alloys are divided into two categories based on the CuNi alloy composition. The lighter alloys (CuNi10 and CuNi20) after polishing lead to complete monolayer of h-BN growing with a larger h-BN film grain size (10 µm) than Cu (1-2 µm). The heavier alloys (CuNi30-50) are best suited to grow well coalesced isolated h-BN crystals and quasi-films.

5.5 Growth of h-BN on $Ni_{1-x}Cu_x$

A closer look at FT-IRRAS and XPS results is necessary to understand h-BN growth behavior on NiCu alloys (Figure 5.16). Figure 5.16a shows the FT-IRRAS integrate peak area versus Cu wt.%., where the amount of h-BN decreases as the Cu wt.% increases. The XPS B 1s peak area, which is proportional to the amount of h-BN, also shows a decreasing trend with increasing Cu wt.% (Figure 5.16b). However, in contrast to Ni, there is a substantial increase in the amount of h-BN on NiCu10 alloy, which is present in both FT-IRRAS and XPS results. Additionally, XPS data reveals that the amount of h-BN is similar on heavier NiCu alloys (NiCu30-50). Unlike h-BN growth on CuNi alloys, the growth trend of h-BN on NiCu alloys is very clear: increasing Cu wt.%, decreasing amount of h-BN.

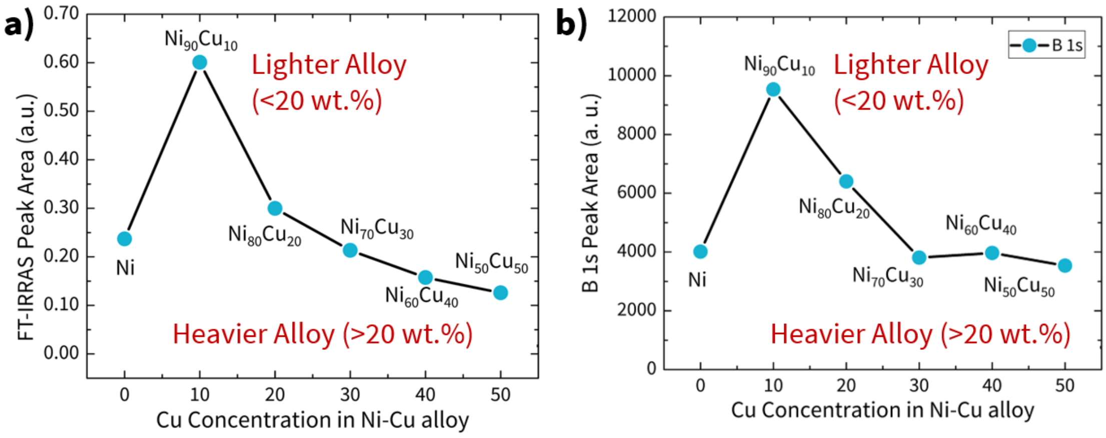

Figure 5.16: a) FT-IRRAS peak area analysis, b) XPS B 1s peak area analysis of NiCu alloys from 10 wt.% to 50 wt.% of Cu.

5.5.1 Assessing the h-BN growth on NiCu alloys

Figure 5.17 shows the SEM micrographs of h-BN grown on unpolished NiCu alloys (left column) and mechanically polished (right column). This highlights the importance and the role of surface preparation in promoting larger h-BN crystal formation on NiCu alloys. On both the unpolished and polished Ni reference samples (Figure 5.17a and 5.17b), there is uncontrolled growth of h-BN.

The h-BN growth on polished Ni has a higher affinity to the Ni substrate grain orientation, where only certain grains orientations result in h-BN film growth [65]. As evidenced using SEM characterization, the growth of h-BN on Ni is undesirable due to uncontrolled h-BN nucleation. On NiCu10 alloy, there are micron-sized nucleates randomly dispersed (Figures 5.17c and 5.17d) on both unpolished and polished NiCu10 samples without substrate grain-dependent h-BN nucleation as evidenced on Ni substrates. This result suggests that NiCu10 alloy is still not an optimal substrate for h-BN growth. On unpolished NiCu30 alloys, there are smaller ($\approx$1 µm size) h-BN crystals growing on the surface (Figure 5.17e). However, on polished NiCu30 alloy, both monolayer h-BN crystals and multilayer h-BN crystals are observed to grow (Figure 5.17f). The monolayer h-BN grain size is as large as 6-15 µm in size, while the multilayer h-BN is $\approx$5 µm in size. The formation of larger monolayer and multilayer h-BN highlights the effect of surface finishing of alloy sample on h-BN growth. On the unpolished NiCu50 alloy (Figure 5.17g), the h-BN nucleates grow randomly on the surface. h-BN on polished NiCu50 alloy sample (Figure 5.17h) shows similar growth behavior as polished NiCu30 alloy (Figure 5.17f), with a 10 µm sized monolayer of h-BN under $\approx$3 µm sized multilayered h-BN crystals.

SEM micrographs are used to assess the growth morphology and understand how the h-BN crystal morphology correlates to the respective FT-IRRAS and XPS spectra. In comparison with Ni, the FT-IRRAS and XPS data show that there is an increase in the amount of h-BN on NiCu10 alloy, which can be attributed to the randomly dispersed thick (n-layer) h-BN nucleates on NiCu10 alloy. There is a gradual decrease in the amount of h-BN in FT-IRRAS and XPS in NiCu30-50 alloys, which can be attributed to the formation of multilayered h-BN crystals. The SEM analysis suggests that the polished heavier alloys (NiCu30-50) are suitable for the growth of multilayered h-BN crystals as there is clear evidence of well-formed crystals. Additionally, NiCu10 and NiCu30 alloy samples show different h-BN crystals morphologies. Therefore, SEM is used to assess h-BN growth on NiCu20 alloy to understand the possible transitionary nature of the substrate.

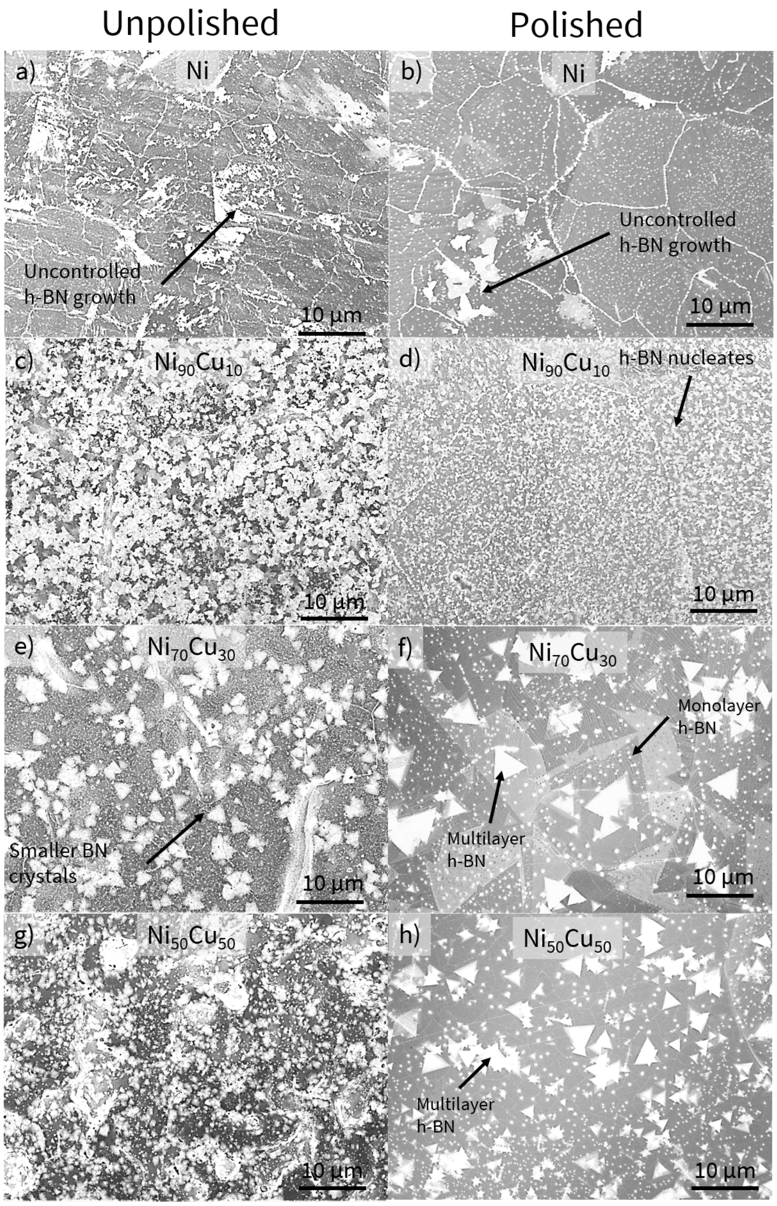

Figure 5.17: SEM micrographs of h-BN grown on NiCu alloys before and after polishing. a) and b) h-BN on unpolished and polished Ni control sample, c) and d) h-BN on unpolished and polished NiCu10 alloy sample, e) and f) h-BN on unpolished and polished NiCu30 alloy sample, g) and h) h-BN on unpolished and polished NiCu50 alloy sample.

Figure 5.18 shows SEM micrographs of polished NiCu10, 20, and 30 alloy samples for two different growth conditions: growth A has a precursor flow rate of 50 sccm (left column) and growth B has a precursor flow rate of 40 sccm (right column), with identical growth time (60 mins). In growth A, the NiCu10 alloy (Figure 5.18a) shows a complete film of h-BN with a noticeable amount of secondary nucleation. NiCu20 alloy in growth A (Figure 5.18c) also displays a similar behavior as NiCu10 alloy, where there is a quasi-film of h-BN with extensive secondary nucleation. However, in NiCu30, the multilayered h-BN crystals form on top of a quasi-film of h-BN (Figure 5.18e). In growth B, there is no observable amount of secondary nucleation in NiCu10 alloy (Figure 5.18b). NiCu20 alloy in growth B has multilayered h-BN crystals forming (Figure 5.18d), deviating from NiCu10 alloy in growth B and NiCu20 alloy in growth A. h-BN on NiCu30 alloy (Figure 5.18f) in growth B shows similar multilayered h-BN crystal growth behavior as NiCu20 alloy. This discussion presents the transitionary nature of NiCu20 alloy substrates, where the h-BN growth tendencies of either lighter or heavier alloys can be observed depending on the growth condition.

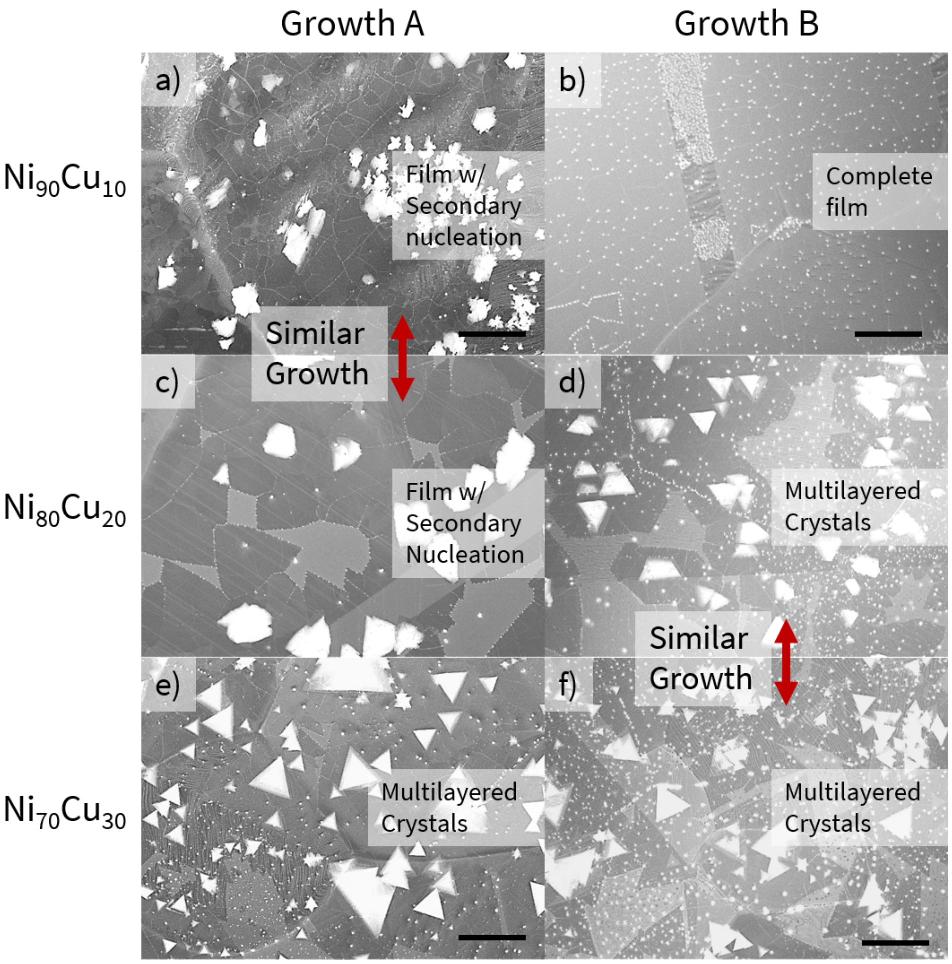

Figure 5.18: Growth of h-BN on NiCu20 alloy showing tendencies of both lighter alloy in growth A conditions and heavier alloy in growth B conditions. a) h-BN on NiCu10 alloy from growth A, b) h-BN on NiCu10 alloy from growth B, c) h-BN on NiCu20 alloy from growth A, d) h-BN on NiCu20 alloy from growth B, e) h-BN on NiCu30 from growth A, f) h-BN on NiCu20 alloy from growth B. The scale bar is 10 µm.

From the above discussion, both Ni and NiCu alloys result in the formation of multilayered h-BN. As SEM micrographs are obtained in both in-lens and secondary electrons (SE) modes, the h-BN morphology on Ni and NiCu30 alloy substrates can be differentiated (Figure 5.19). The in-lens mode is used to distinguish h-BN from the Ni and alloy substrate, and SE mode is used to assess the topography of the h-BN film or crystal. From the in-lens image (Figure 5.19a), h-BN on Ni appears to have a quasi-film structure. However, the SE image (Figure 5.19b) reveals several triangular features on the h-BN quasi-film indicating a high degree of mosaicity and polycrystallinity. Mosaicity is defined as the spread of crystal plane orientations in the film [269]. However, h-BN on NiCu30 alloy has a multilayered triangular-shaped crystal with no visible mosaicity, demonstrating single crystalline multilayered h-BN crystal growth (Figures 5.19c and 5.19d). The SEM analysis suggests that h-BN growth on NiCu alloys leads to higher quality h-BN multilayered single crystals derived from the lack of mosaicity in the crystal.

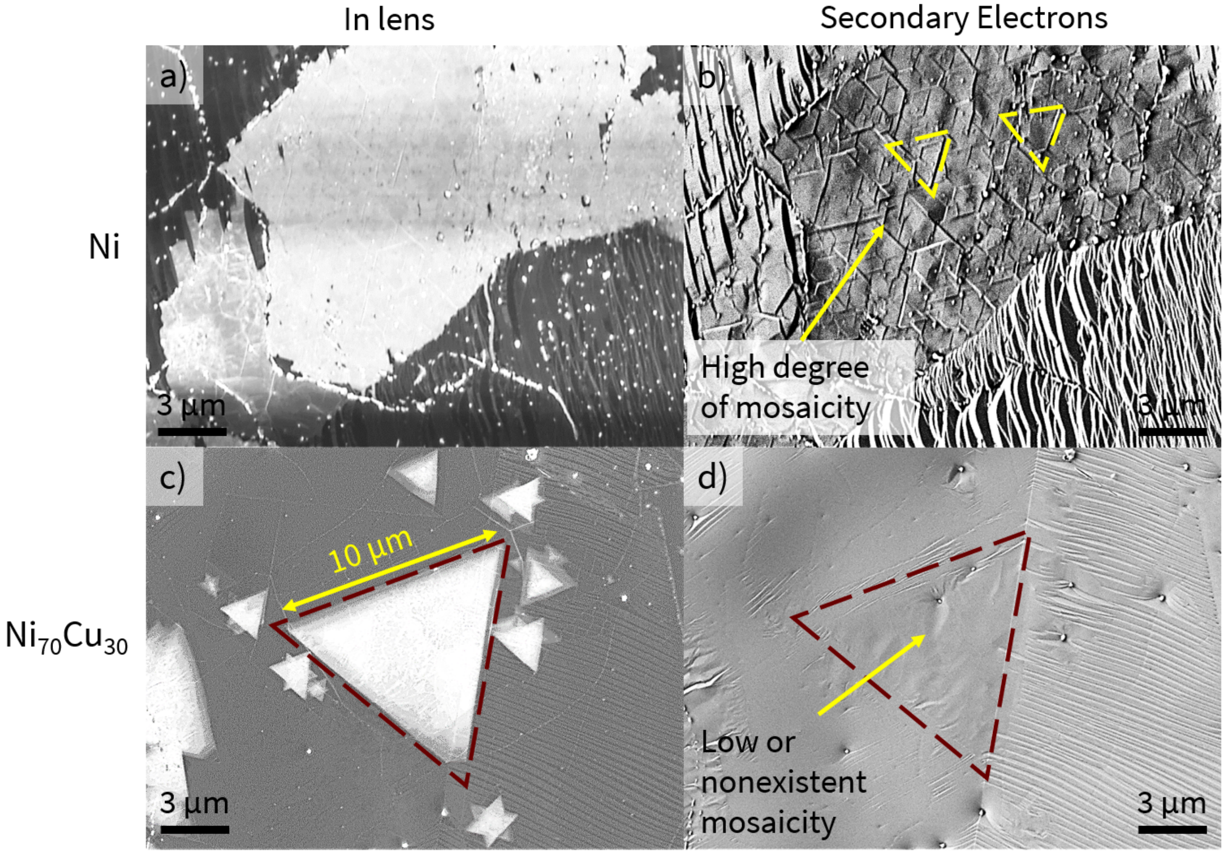

Figure 5.19: SEM micrographs of Ni (a) and (b) and NiCu30 alloys (c) and (d) assessing the h-BN crystal morphology. The difference in the degree of mosaicity is clear between the samples.

Figure 5.20 shows a tableau using SEM micrographs of h-BN growth on two different alloys and two different growth conditions. The alloy samples in Figures 5.20a and 5.20b have a growth time of ≈260 mins with a precursor flow rate of 40 sccm and the samples in Figures 5.20c and 5.20d have a growth time of 60 mins and precursor flow rate of 40 sccm. A single layer h-BN crystal ≈20 µm grows on NiCu30 sample (Figure 5.20a). However, during the same growth run, a multilayer single crystal (≈15 µm in size) grows on NiCu20 alloy sample (Figure 5.20b). Similarly, by varying the growth condition, a quasi-film of h-BN grows on NiCu30 alloy sample (Figure 5.20c) and a single layer continuous film is observed on NiCu20 alloy sample (Figure 5.20d). This indicates that by modulating the growth conditions, a variety of h-BN structures can be grown on NiCu alloys establishing the versatility of NiCu alloy substrates.

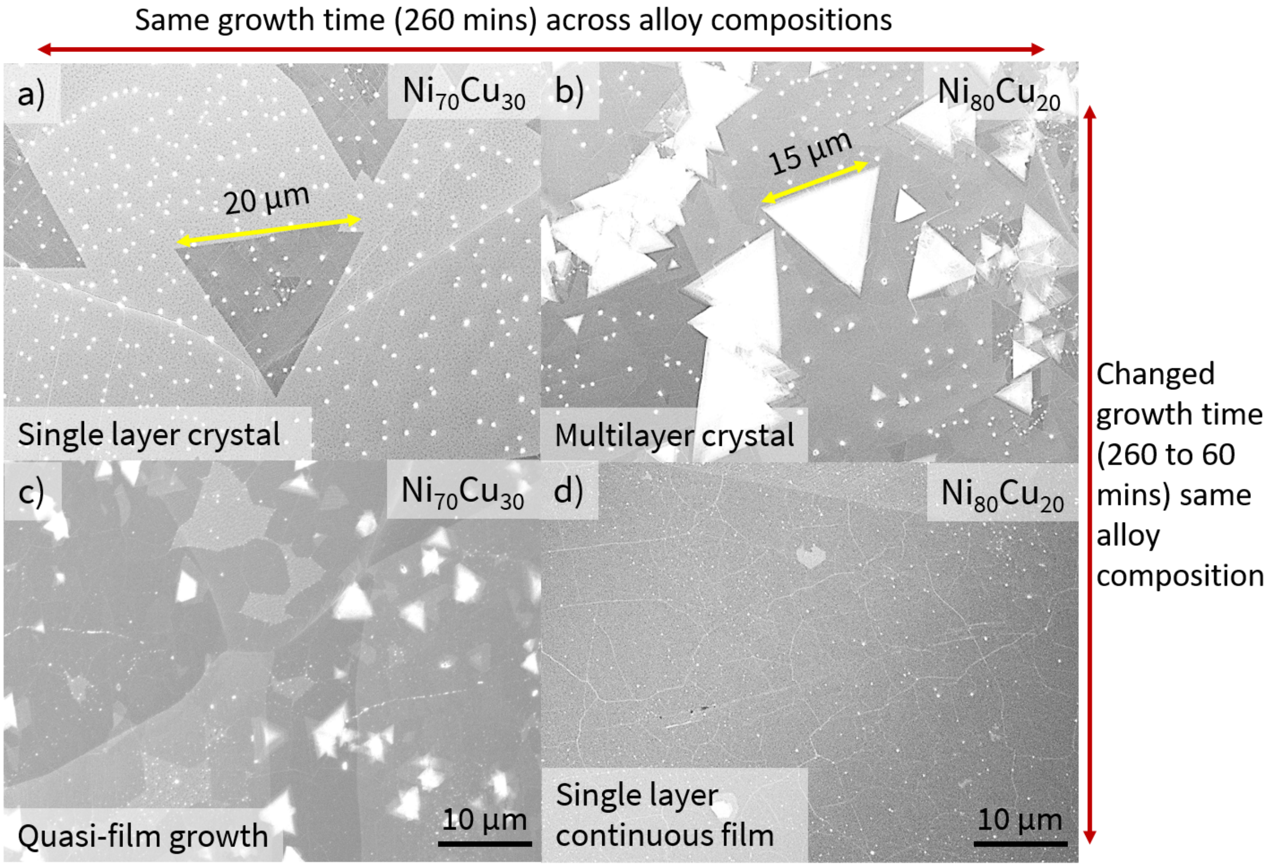

Figure 5.20: SEM micrographs of h-BN growth across alloy compositions and growth conditions. a) Monolayered h-BN film on NiCu30 alloy, b) multilayered h-BN film on NiCu20 alloy, c) monolayered quasi-film on NiCu30 alloy, d) single layered continuous film on NiCu20 alloy.

5.5.2 Characterization of NiCu alloy surfaces after h-BN growth

XPS is performed on NiCu alloys after h-BN growth to understand the evolution of Ni 2p and Cu 2p peaks at different alloy concentrations, which informs the changes in the oxidation state (Figure 5.21). The oxidation states of Ni and Cu can be identified with the respective satellite peaks (Figure 5.21a and 5.21b, respectively) and Figures 5.21c and 5.21d are magnified and truncated versions of Figure 5.21a and 5.21b. Figure 5.21a shows the existence of a Ni 2p$^{3/2}$ satellite peak next to the Ni 2p$^{3/2}$ peak at $\approx$852 eV indicating a native oxide on the alloy surface [260, 261, 262]. The satellite peak intensity is lower than Ni metal peak and the intensity does not change with increasing Cu concentration (Figure 5.21c). Additionally, there is no noticeable shift in Ni 2p$^{3/2}$ peak (Figure 5.21a and 5.21c) informing that the amount of native oxide of Ni, Ni(OH)$_2$, is proportionally similar on all Ni and NiCu alloy samples [260, 261, 262].

The role of Cu in NiCu alloys is also analyzed using the Cu 2p peak (Figure 5.21b and 5.21d). The Cu 2p peak in NiCu10 alloy does not show any formation of Cu native oxide as there are no observable satellite peaks indicating a metal-like surface [236, 263, 264, 265, 266, 267, 268]. This shows that Cu does not play an active role in the dissociation of the ammonia borane precursor in NiCu10 alloy. In NiCu20 alloy, the signal is too weak to extract meaningful information. However, in NiCu30 (brown line), a Cu satellite peak is observed (Figure 5.21b and 5.21d), along with a shoulder peak on Cu 2p$^{3/2}$, which suggests a Cu(II) oxide formation [263, 264, 265, 266, 267, 268]. While this phenomenon is clear in NiCu30 alloy, the satellite peaks of Cu are much more subdued in NiCu40 and NiCu50 alloys.

The h-BN growth mechanism on Ni is not fully established. However, the solid-gas reactions between Ni and B, and Ni and N, dictate the growth, yielding thicker uncontrolled h-BN films. This is different in Cu where h-BN growth is surface limited producing monolayer films. The XPS results show that adding Cu to Ni slows the solid-gas reactions leading to a more controlled h-BN growth on NiCu alloy. This is clearly observed using SEM characterization as multilayered h-BN crystal are grown on heavier NiCu alloy (NiCu30-50).

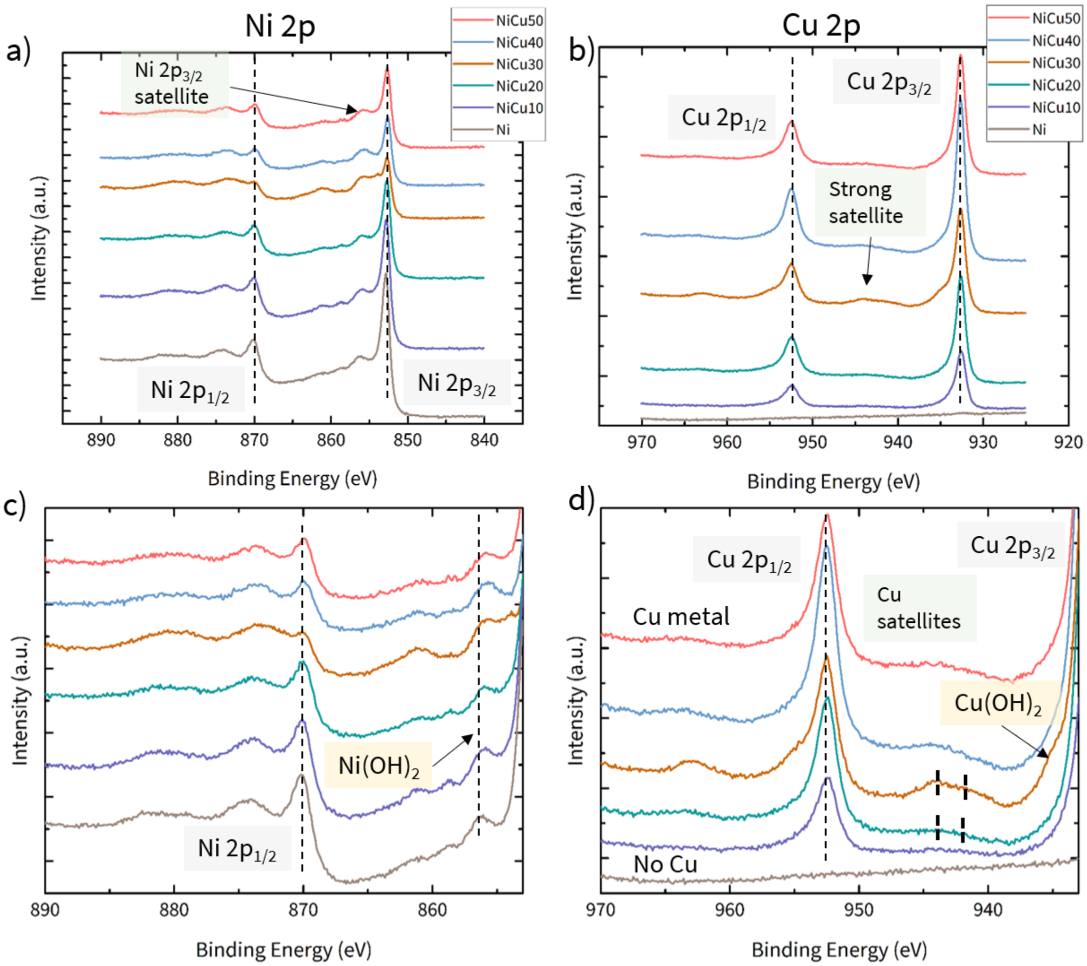

Figure 5.21: XPS analysis of NiCu alloys. a) Ni 2p, b) Cu 2p, c) Ni 2p region limited to 850-890 eV, d) Cu 2p region limited to 930-970 eV.

5.5.3 Summary of h-BN growth on NiCu alloys

The FT-IRRAS, XPS, and SEM characterization show that the heavier alloys (NiCu30-50) are well suited for the growth of both monolayered and multilayered h-BN single crystals as large as 20 µm in size. The lack of mosaicity is also a desirable trait as single crystalline multilayered growth of h-BN is evident on NiCu alloys. Additionally, the role of mechanical polishing is extremely critical as h-BN growth on polished alloys yield larger multilayered h-BN crystals. These results indicate that NiCu alloy holds promise as a substrate for the controlled growth of multilayered h-BN crystals.

5.6 Discussion on h-BN growth on Cu$_{50}$Ni$_{50}$ and Ni$_{50}$Cu$_{50}$ alloys

5.6.1 Growth morphology of h-BN on Cu$_{50}$Ni$_{50}$ and Ni$_{50}$Cu$_{50}$ alloys

The critical juncture where the stoichiometry of Cu-rich and Ni-rich alloys are balanced (CuNi50 and NiCu50), the h-BN growth pattern deviates as observed using FT-IRRAS and XPS (Figure 5.10a and b). The amount of h-BN on CuNi50 alloy is lower than on NiCu50 alloy from the FT-IRRAS and XPS peak area analysis. From the SEM characterization, there are large monolayer h-BN crystals observed to grow on CuNi50 alloy samples, while on NiCu50 alloy samples, there are multilayered h-BN crystals growing. To investigate this behavior further, h-BN growth on CuNi50 and NiCu50 alloys is examined for two different growth conditions A and B (Figure 5.22). In growth A, the precursor flow rate is 50 sccm and in growth B, the precursor flow rate is 40 sccm with identical growth times. Individual h-BN crystals of $\approx$5 µm and 1 µm sizes grow on CuNi50 alloy in growth A and B conditions, respectively (Figures 5.22a and 5.22b). In contrast, multilayered crystals grow on top of monolayer films of h-BN on NiCu50 alloy substrate in growth A. However, in growth B, large single crystals ($\approx$25 µm in size) grow on NiCu50 indicating different h-BN growth behavior despite having an identical same alloy composition (50 wt.% Cu and 50 wt.% Ni). The differences in h-BN growth on CuNi50 and NiCu50 alloys can be studied from the surface and microstructure perspective of both these alloys using XPS and EBSD, respectively.

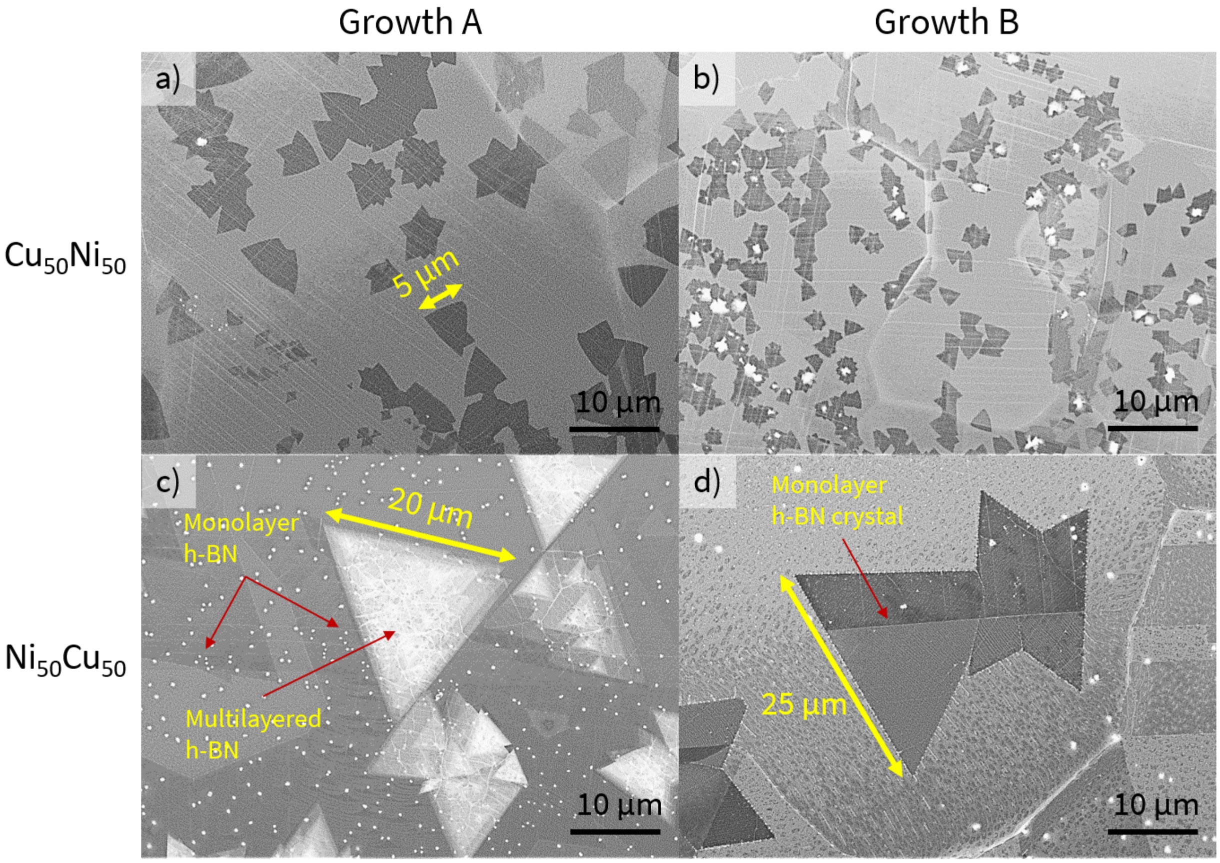

Figure 5.22: SEM micrographs of h-BN grown on CuNi50 and NiCu50 in two different growth conditions, growth A and growth B. a) CuNi50 in growth A, b) CuNi50 in growth B, c) NiCu50 in growth A, d) NiCu50 in growth B.

5.6.2 Surface characterization after h-BN growth

The XPS results for both CuNi50 and NiCu50 alloy substrates, along with the Cu and Ni control samples, after h-BN growth are shown (Figure 5.23). The primary peaks of Ni and Cu, Ni 2p and Cu 2p are used to analyze the nature of the surface. Figure 5.23a shows the Ni 2p peak and Figure 5.23b shows the Cu2p peak. The Ni 2p$^{1/2}$ and Cu 2p$^{1/2}$ are truncated at 853 eV and 933 eV, respectively, and magnified to identify subtle changes in the peak shapes and the changes in the oxidation states. From Figure 5.23a, the Ni sample has the most intense Ni 2p$^{3/2}$ peak with an adjacent satellite peak indicating the presence of surface oxide. In contrast with Ni control, the

Ni 2p decreases in intensity for NiCu50 and CuNi50 alloy samples. Additionally, the Ni 2p peak in CuNi50 alloy is much lower in intensity than NiCu50 alloy denoting a Ni deficiency on the top surface of the sample. The intensity of the Ni oxide peak is similar for all the three samples: Ni, NiCu50 and CuNi50 (Figure 5.23c), implying that all the three samples have a similar relative amount of surface native oxide.

The satellite peaks of Cu (Figures 5.23b and 5.23d), observable only on the Cu control sample and CuNi50 alloy, reveal surface oxidation. The satellite peaks on Cu indicate that the Cu has a native Cu(I)O (Cu_2O) oxide. The satellite peaks for CuNi50 alloy are shifted and there is a shoulder peak on Cu 2p$^{3/2}$ peak indicating the presence of $Cu(OH)_2$ (+2 oxidation state). There are no satellite peaks or shoulder peaks on Cu 2p$^{3/2}$ in NiCu50 alloy sample, revealing that the Cu surface is not oxidized and is metal-like. This also implies that the Cu in NiCu50 alloy is on the alloy surface and is playing a passive role in dictating h-BN growth. Additionally, the Cu 2p intensity in CuNi50 and NiCu50 alloy are similar, contrary to Ni 2p, confirming that CuNi50 alloy is Ni deficient on the surface.

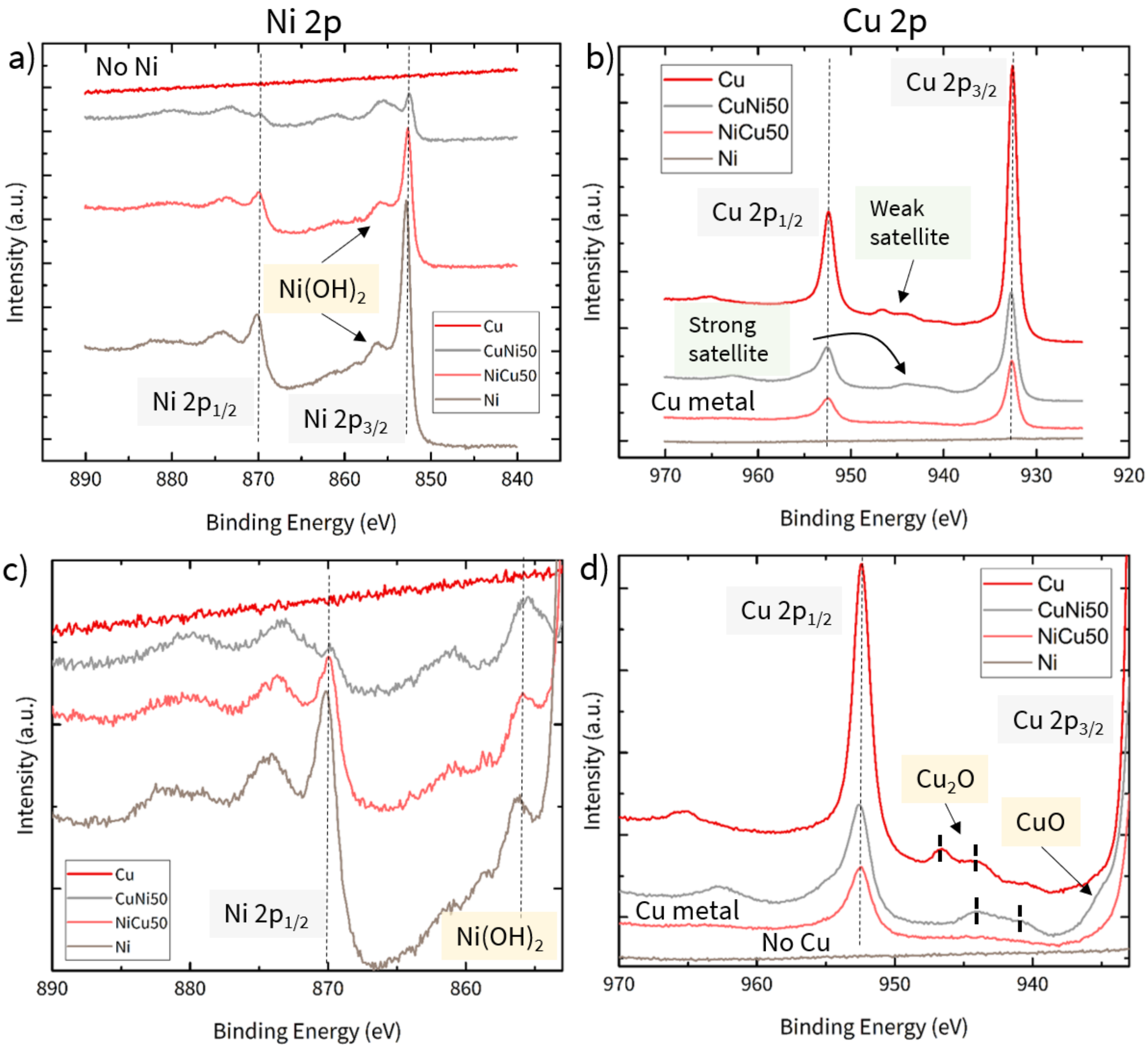

Figure 5.23: XPS analysis of CuNi50 and NiCu50. a) Ni 2p, b) Cu 2p, c) Ni 2p region limited to 850-890 eV, d) Cu 2p region limited to 930-970 eV.

5.6.3 Microstructural evaluation of $Cu_{50}Ni_{50}$ and $Ni_{50}Cu_{50}$ alloys

The microstructural information and the grain size statistics of CuNi50 and NiCu50 alloys after h-BN are obtained using EBSD (Figure 5.24). Figures 5.24c and 5.24d show the grain size distribution of CuNi50 and NiCu50 alloys, respectively, and neither alloy shows any preferential orientation. Additionally, there is a prominence of twin grains in both CuNi50 and NiCu50 alloys.

From the grain statistics analysis, the CuNi50 alloy has smaller grain sizes (15-25 µm) than the NiCu50 alloy (20-30 µm). The average grain size is calculated to be around 18 µm ($\approx$324 µm^2) for the CuNi50 alloy and 22 µm ($\approx$484 µm^2) for the NiCu50 alloy. The histogram of grain sizes for the CuNi50 and NiCu50 alloys (Figure 5.24c and 5.24d) reveals that the NiCu50 alloy has several grains much larger than 22 µm ($\approx$484 µm^2). Microstructural analysis indicates that the h-BN growth might be less dependent on the alloy orientation and more on the surface composition.

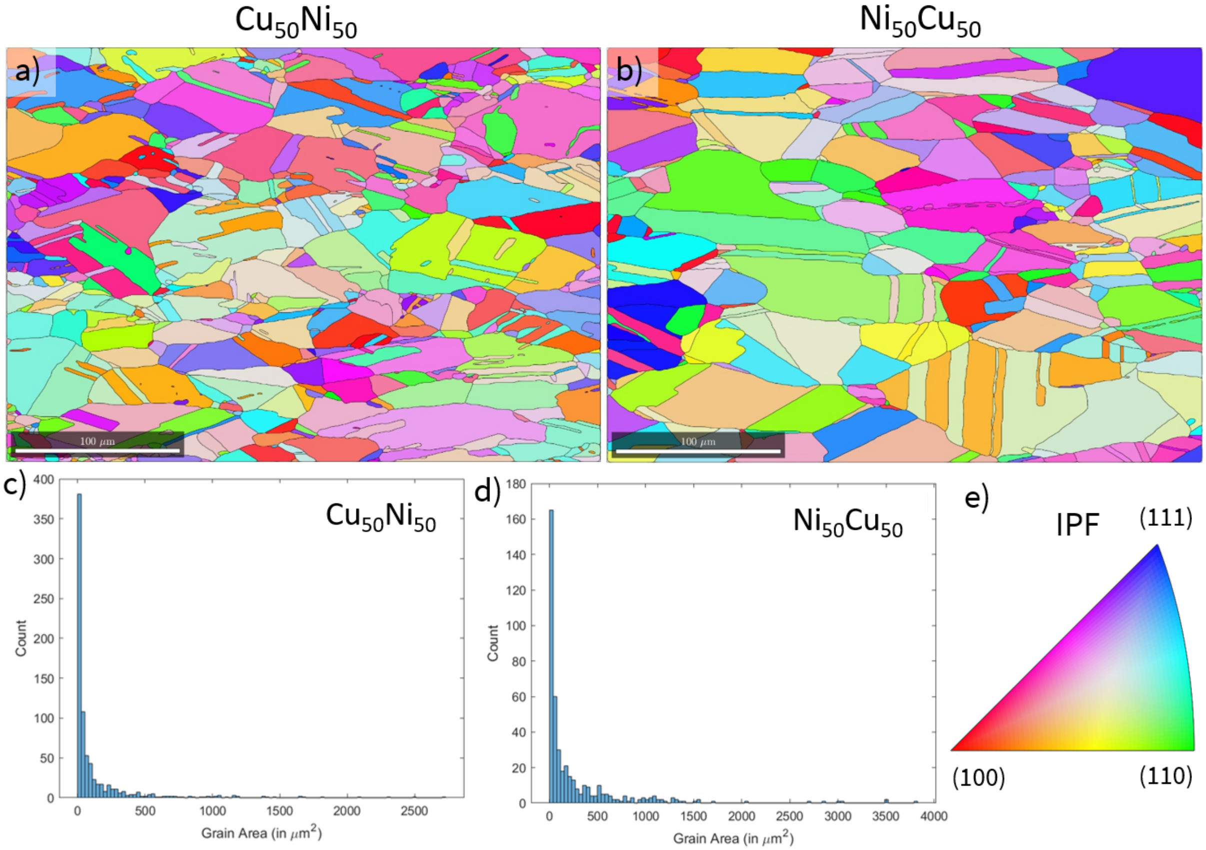

Figure 5.24: EBSD analysis of the microstructure of h-BN on CuNi50 and NiCu50 from growth A. a) Microstructure of CuNi50 alloy, b) Microstructure of CuNi50 alloy, c) Histogram of grain sizes in CuNi50 alloy, d) Histogram of grain sizes in NiCu50 alloy, e) IPF reference for EBSD maps.

The surface and microstructural characterization of CuNi50 and NiCu50 alloys after h-BN growth reveals that the deviation in h-BN growth is largely due to the differences in the alloy surface composition. As highlighted in the XPS analysis from above, the topmost surface composition of CuNi50 and NiCu50 is different, suggesting a Cu-dominated and Ni-dominated catalytic breakdown of ammonia borane precursor. The SEM micrographs (Figure 5.22) further strengthened this statement, where these is only monolayer h-BN growth on CuNi50 and multilayer h-BN growth on NiCu50 alloys. This monolayer-only behavior is very specific to Cu substrate due to it self-limiting nature.

As the microstructure of both the alloys is not very different: similar average grain size and no strong preferred grain orientation, the contribution of microstructure on the h-BN growth is hypothesized to be very limited. Additionally, as discussed in the experimental section, the CuNi alloys and NiCu alloy are prepared differently, where Ni is electrodeposited on Cu and Cu is electrodeposited on Ni to create CuNi and NiCu alloys, respectively. During the thermal annealing process to prepare the CuNi alloy, it is possible that Ni is substituting Cu atoms in the Cu foil preserving the Cu atomic structure (lattice parameter) [256]. This could also be similar with the case of NiCu alloy, where Cu is substituting into Ni atomic position preserving the Ni atomic structure [256]. It is likely that the difference in the lattice constants may also be contributing factor for the deviation of h-BN growth at this critical juncture. The lattice structure of Cu and Ni is face centered cubic (FCC) with a lattice constant of 3.597 Å and 3.499 Å, respectively [270]. To validate the hypothesis, X-ray diffraction (XRD) on both the alloys have to be performed to assess the difference in the lattice parameter.

5.6.4 Summary of h-BN growth on Cu$_{50}$Ni$_{50}$ and Ni$_{50}$Cu$_{50}$ alloys

From the XPS and EBSD analysis, the deviation in h-BN growth on CuNi50 and NiCu50 alloy is more likely to be surface-driven than microstructure-driven. In CuNi50 alloy, both Ni and Cu oxidize, demonstrating the presence of Ni and Cu species on the alloy surface. There is also a reduction in the intensity of Ni 2p peak compared with NiCu50 indicating a deficiency of Ni on the surface. This suggests that Cu is driving the h-BN growth behavior in CuNi50 alloy. However, in NiCu50 alloy, only Ni species oxidize, and the Cu species remain unoxidized. This suggests that the h-BN growth on NiCu50 alloy is Ni dominated as the Cu species is not among the topmost layer leading to a deviation in h-BN growth. XRD characterization needs to be performed to determine the lattice constants of CuNi50 and NiCu50 alloys, which could also be contributing to the difference in h-BN growth patterns in both the alloys.

5.7 Summary and Conclusion

This work demonstrates the growth of h-BN on a Cu-Ni binary alloys, which are prepared using electrodeposition and thermal annealing. The morphological assessment of alloys suggests a planarized surface after mechanical polishing making it more suitable for h-BN growth. Cu-rich (CuNi) alloys, that are prepared using Ni electroplating of Cu, show monolayer h-BN growth akin to Cu. However, the grain size of the monolayer h-BN films is larger on lighter CuNi alloys than Cu. The monolayer h-BN crystals and films that grow on heavier CuNi alloys (30-50 wt.% Ni) are extremely well-coalesced as the grain boundaries of h-BN films are weakly visible. This overcomes the limitation of poor crystal coalescence observed with Cu. On the other hand, Ni-rich (NiCu) alloys facilitate the growth of both monolayer and multilayer h-BN growth. The crystal sizes of h-BN on NiCu alloys are $\approx$20 µm in size, which are much larger than $\approx$2 µm on Cu foils. This shows that the growth behavior of h-BN on the Cu-Ni binary alloys is different from Cu and strongly dependent on the alloy composition. In conclusion, this study affirms that the Cu-Ni binary alloy substrates overcome the limitations posed by Cu substrates to enable the growth of monolayer and multilayer h-BN using APCVD.

6. SUMMARY, CONCLUSIONS AND FUTURE WORK

6.1 Summary

This body of work is an effort: 1) to understand the growth of h-BN on Cu, and 2) to develop a binary alloy substrate based on Cu and Ni to overcome the limitations of Cu and use the alloy composition to grow monolayered and multilayered h-BN crystals. Various characterization techniques (FT-IRRAS, SEM, STM, and AFM) are used to assess the morphology of h-BN crystals and films on Cu. The key observation is that h-BN follows the surface features (atomic steps and step edges) of Cu. STM characterization also reveals a gap of 50 nm in-between twin crystals of h-BN, which shows poor coalescence of h-BN domains growing on Cu substrates.

The growth of h-BN is studied both from Cu substrate surface and microstructural perspective. The state of Cu foil substrates supplied by vendors such as Alfa Aesar and Sigma Aldrich is assessed using AFM and SEM. The Cu foils supplied by the vendors are prepared using a cold rolling process, which leads to an extremely rough surface with rolling lines and metal impurities on the surface. This makes the Cu foils unsuitable for the growth of 2D materials. Therefore, a two-step thermal annealing and electropolishing technique is used for the Cu foil substrates to make it more suitable to grow 2D materials. The thermal annealing step is performed at 1030°C in H_2/N_2 environment, which reduces the rolling lines and the native Cu oxide. The electropolishing step further planarizes the thermally annealed Cu foil, while also removing any stray native oxide on the Cu surface. This two-step technique yields a Cu surface that is extremely smooth and well-suited for the growth of 2D materials. When h-BN is grown on Cu substrates prepared using the two-step processing technique, there is a decrease in the number of nucleation sites of h-BN and an increase in h-BN crystal size. The h-BN films grown on electropolished Cu foils also have very little or no secondary nucleation. Similarly, graphene is also grown on the Cu foils prepared using the two-step method to assess the versatility of this processing technique. Graphene crystals as large as 100 µm are also shown to grow on these Cu foils, with much better coalescence than unpolished Cu.

This work also shows that the growth of h-BN is dependent on the grain orientation of polycrystalline Cu. The relationship between Cu grain orientation is assessed from inverse pole figure of EBSD maps, and the h-BN on the specific Cu grain, imaged using SEM. The h-BN nucleation is observed to be slowest on (100)-like orientation, where there is no noticeable nucleation of h-BN on the surface for both unpolished and electropolished samples. While on (111) and (110)-like grain orientations, well-formed h-BN crystals grow on both unpolished and electropolished Cu samples. Statistical categorization is also performed on all the samples with various grain orientations to understand a general growth trend of h-BN on different Cu orientation. The fast growth takes place on high index grain orientations, where high density of well-formed h-BN crystals or film is observed to grow. The low-index grains, mainly (111)-like and (110)-like, appear to be moderate growth orientations as there is a wide dispersion of no nucleation to film growth regions. (100)-like shows the slowest growth as there is a prominence of no nucleation or marginal nucleation density regions. Therefore, the polycrystalline Cu grain orientation has a strong impact on h-BN growth.

Despite the improvement of the Cu surface with the two-step processing technique, the self-limiting nature of Cu leads to only a monolayer h-BN film growth. In parallel, h-BN growth on Ni yields multilayered h-BN films, as there is a lack of control of h-BN nucleation. By creating a binary alloy of Cu and Ni, the properties of Cu and Ni are combined to enable the controlled growth of thin (monolayer) and thick (>2 layers) films of h-BN. Cu-Ni binary alloys are prepared to understand the growth pattern of h-BN and to find the most suitable alloy combination that will lead to thin and thick films of h-BN. h-BN is grown on the Cu-Ni binary alloys at 10 wt.% steps at the same time, with Cu and Ni acting as control samples.

CuNi alloys (10-50 wt.% Ni), are prepared by electroplating Ni on Cu foils and thermal annealing. h-BN is grown on these alloys after mechanical polishing as the CuNi foils are too rough with surface features such as voids. The lighter CuNi alloys (10-20 wt.% Ni), show improved growth by means of enlarging the h-BN grain size in the polycrystalline h-BN film. The heavier CuNi alloys

(30-50 wt.% Ni) show a slower growth rate but the h-BN crystals and quasi-films are extremely well-coalesced, demonstrating an improvement over Cu foil substrates.

NiCu alloys (10-50 wt.% Cu), are prepared by electroplating Cu on Ni foils and thermal annealing. The NiCu foils are mechanically polished before h-BN growth, as the alloy surface is not very suitable due to the existence of voids on the surface. The growth pattern of h-BN is different on lighter NiCu alloys (10-20 wt.% Cu) and heavier NiCu alloys (30-50 wt.% Cu). NiCu10 alloy shows a growth pattern similar to Ni control sample, where thick and dense uncontrolled h-BN nucleation occurs. However, monolayer and multilayered h-BN crystals grow on heavier NiCu alloys (30-50 wt.% Cu). Therefore, by modulating the growth conditions, along with the alloy composition, both monolayer h-BN films with complete coverage and multilayered h-BN crystals as large as 20 µm in size can be grown.

6.2 Conclusions

In conclusion, the limitations of Cu substrate are assessed by studying the growth morphology of h-BN on Cu, which follows the Cu surface features. The two-step thermal annealing and electropolishing technique is an excellent processing technique well-suited for the growth of 2D materials like graphene and h-BN. The Cu-Ni binary alloys are outstanding substrates to overcome the limitations of Cu substrates, facilitating the growth of thin and thick h-BN. CuNi alloys are extremely well suited to grow large well-coalesced h-BN crystals and films. Similarly, NiCu alloys provide an opportunity for controlled epitaxial growth of monolayer and multilayered h-BN crystals suitable to be used as a substrate for 2D materials and a tunnel dielectric for tunnel diodes.

6.3 Future Work

The long-term goal of this project is to epitaxially grow graphene and h-BN vertical heterostructures to demonstrate metal-insulator-metal (MIM) and metal-insulator-metal-insulator-metal (MIMIM) tunnel diodes for THz applications. The ability to control the thickness of h-BN is of great importance as it acts as a tunnel barrier to control the tunneling currents, along with the h-BN crystal size (>100 µm in size). This requires the development of thin and thick h-BN growth using CMOS-compatible techniques such as CVD. The growth of h-BN on Cu using APCVD has been demonstrated. Despite the shortcomings of Cu as a substrate for h-BN due to poor coalescence, polycrystalline Cu remains the substrate of choice for the growth of h-BN and graphene. The Cu substrate grain dependent growth of h-BN and graphene can be more extensively investigated by performing EBSD and SEM on electropolished Cu, which is not affected by microfaceting. While the statistical categorization approach can be rudimentary, a more sophisticated quantitative approach can be utilized by obtaining the percent coverage of h-BN on Cu using image processing techniques. Such a method will confirm the role that the Cu substrate plays in h-BN and graphene nucleation and provide Cu grain-dependent growth rate of h-BN and graphene.

Even though h-BN is successfully grown on the complete Cu-Ni binary alloy system in this work, there is still scope for future studies in this system. The growth mechanism on both CuNi and NiCu alloy system must be investigated, especially using computational techniques. This is of great scientific interest because the growth pattern and behavior of h-BN is very different for CuNi and NiCu alloys. While well-coalesced monolayer h-BN polycrystalline films are observed to grow on CuNi alloys, SPM and AFM techniques can be used to measure the polycrystalline h-BN film grain boundary width. In contrast, multilayered h-BN crystals are observed to grow on NiCu alloys. The thickness of these multilayered h-BN crystals can be determined using AFM and cross-sectional TEM. The ability to control the thickness of h-BN by varying the alloy composition and growth conditions has to be further investigated. More importantly, the growth conditions that will yield multilayered h-BN films with a grain size in excess of 50 µm in size on NiCu alloys have to be studied. The role of the Cu-Ni binary alloy grain orientation and its relationship with h-BN can also be studied using EBSD and SEM techniques. Finally, the electronic quality of the h-BN crystals can be assessed using current-voltage measurements by fabricating metal-insulator-metal (MIM) devices.

REFERENCES

[1] K. S. Novoselov, “Electric field effect in atomically thin carbon films,” *Science*, vol. 306, pp. 666–669, Oct. 2004.

[2] K. S. Novoselov, D. Jiang, F. Schedin, T. J. Booth, V. V. Khotkevich, S. V. Morozov, and A. K. Geim, “Two-dimensional atomic crystals,” *Proceedings of the National Academy of Sciences*, vol. 102, pp. 10451–10453, Jul. 2005.

[3] A. K. Geim and I. V. Grigorieva, “Van der waals heterostructures,” *Nature*, vol. 499, pp. 419–425, Jul. 2013.

[4] M. C. Lemme, T. J. Echtermeyer, M. Baus, and H. Kurz, “A graphene field-effect device,” *IEEE Electron Device Letters*, vol. 28, pp. 282–284, Apr. 2007.

[5] H. Wang, D. Nezich, J. Kong, and T. Palacios, “Graphene frequency multipliers,” *IEEE Electron Device Letters*, vol. 30, pp. 547–549, May. 2009.

[6] X. Li, M. Zhu, M. Du, Z. Lv, L. Zhang, Y. Li, Y. Yang, T. Yang, X. Li, K. Wang, H. Zhu, and Y. Fang, “High detectivity graphene-silicon heterojunction photodetector,” *Small*, vol. 12, pp. 595–601, Dec. 2015.

[7] T. Yu, F. Wang, Y. Xu, L. Ma, X. Pi, and D. Yang, “Graphene coupled with silicon quantum dots for high-performance bulk-silicon-based schottky-junction photodetectors,” *Advanced Materials*, vol. 28, pp. 4912–4919, Apr. 2016.

[8] X. Wang, L. Zhi, and K. Müllen, “Transparent, conductive graphene electrodes for dye-sensitized solar cells,” *Nano Letters*, vol. 8, pp. 323–327, Jan. 2008.

[9] G. Eda, G. Fanchini, and M. Chhowalla, “Large-area ultrathin films of reduced graphene oxide as a transparent and flexible electronic material,” *Nature Nanotechnology*, vol. 3, pp. 270–274, Apr. 2008.

[10] Y. Wang, X. Chen, Y. Zhong, F. Zhu, and K. P. Loh, “Large area, continuous, few-layered graphene as anodes in organic photovoltaic devices,” *Applied Physics Letters*, vol. 95, p. 063302, Aug. 2009.

[11] J. Chen, M. Badioli, P. Alonso-González, S. Thongrattanasiri, F. Huth, J. Osmond, M. Spasenović, A. Centeno, A. Pesquera, P. Godignon, A. Z. Elorza, N. Camara, F. J. G. de Abajo, R. Hillenbrand, and F. H. L. Koppens, “Optical nano-imaging of gate-tunable graphene plasmons,” *Nature*, vol. 487, pp. 77–81, Jun. 2012.

[12] H. Yan, T. Low, W. Zhu, Y. Wu, M. Freitag, X. Li, F. Guinea, P. Avouris, and F. Xia, “Damping pathways of mid-infrared plasmons in graphene nanostructures,” *Nature Photonics*, vol. 7, pp. 394–399, Apr. 2013.

[13] T. Low and P. Avouris, “Graphene plasmonics for terahertz to mid-infrared applications,” *ACS Nano*, vol. 8, pp. 1086–1101, Jan. 2014.

[14] D. Rodrigo, O. Limaj, D. Janner, D. Etezadi, F. J. G. de Abajo, V. Pruneri, and H. Altug, “Mid-infrared plasmonic biosensing with graphene,” *Science*, vol. 349, pp. 165–168, Jul. 2015.

[15] D. Cohen-Tanugi and J. C. Grossman, “Water desalination across nanoporous graphene,” *Nano Letters*, vol. 12, pp. 3602–3608, Jun. 2012.

[16] A. A. Sagade, A. I. Aria, S. Edge, P. Melgari, B. Gieseking, B. C. Bayer, J. C. Meyer, D. Bird, P. Brewer, and S. Hofmann, “Graphene-based nanolaminates as ultra-high permeation barriers,” *npj 2D Materials and Applications*, vol. 1, Oct. 2017.

[17] S. Lee and Z. Zhong, “Nanoelectronic circuits based on two-dimensional atomic layer crystals,” *Nanoscale*, vol. 6, pp. 13283–13300, Sep. 2014.

[18] K. S. Novoselov, A. K. Geim, S. V. Morozov, D. Jiang, M. I. Katsnelson, I. V. Grigorieva, S. V. Dubonos, and A. A. Firsov, “Two-dimensional gas of massless Dirac fermions in graphene,” *Nature*, vol. 438, pp. 197–200, Nov. 2005.

[19] A. K. Geim and K. S. Novoselov, “The rise of graphene,” *Nature Materials*, vol. 6, pp. 183–191, Mar. 2007.

[20] K. Bolotin, K. Sikes, Z. Jiang, M. Klima, G. Fudenberg, J. Hone, P. Kim, and H. Stormer, “Ultrahigh electron mobility in suspended graphene,” *Solid State Communications*, vol. 146, pp. 351–355, Jun. 2008.

[21] H. Wang, T. Taychatanapat, A. Hsu, K. Watanabe, T. Taniguchi, P. Jarillo-Herrero, and T. Palacios, “BN/graphene/BN transistors for RF applications,” *IEEE Electron Device Letters*, vol. 32, pp. 1209–1211, Sep. 2011.

[22] L. Britnell, R. V. Gorbachev, A. K. Geim, L. A. Ponomarenko, A. Mishchenko, M. T. Greenaway, T. M. Fromhold, K. S. Novoselov, and L. Eaves, “Resonant tunnelling and negative differential conductance in graphene transistors,” *Nature Communications*, vol. 4, Apr. 2013.

[23] L. Britnell, R. V. Gorbachev, R. Jalil, B. D. Belle, F. Schedin, A. Mishchenko, T. Georgiou, M. I. Katsnelson, L. Eaves, S. V. Morozov, N. M. R. Peres, J. Leist, A. K. Geim, K. S. Novoselov, and L. A. Ponomarenko, “Field-effect tunneling transistor based on vertical graphene heterostructures,” *Science*, vol. 335, pp. 947–950, Feb. 2012.

[24] C. R. Dean, A. F. Young, I. Meric, C. Lee, L. Wang, S. Sorgenfrei, K. Watanabe, T. Taniguchi, P. Kim, K. L. Shepard, and J. Hone, “Boron nitride substrates for high-quality graphene electronics,” *Nature Nanotechnology*, vol. 5, pp. 722–726, Aug. 2010.

[25] X. Cui, G.-H. Lee, Y. D. Kim, G. Arefe, P. Y. Huang, C.-H. Lee, D. A. Chenet, X. Zhang, L. Wang, F. Ye, F. Pizzocchero, B. S. Jessen, K. Watanabe, T. Taniguchi, D. A. Muller, T. Low, P. Kim, and J. Hone, “Multi-terminal transport measurements of MoS_2 using a van der waals heterostructure device platform,” *Nature Nanotechnology*, vol. 10, pp. 534–40, Apr. 2015.

[26] L. Britnell, R. V. Gorbachev, R. Jalil, B. D. Belle, F. Schedin, M. I. Katsnelson, L. Eaves, S. V. Morozov, A. S. Mayorov, N. M. R. Peres, A. H. C. Neto, J. Leist, A. K. Geim, L. A. Ponomarenko,

and K. S. Novoselov, “Electron tunneling through ultrathin boron nitride crystalline barriers,” *Nano Letters*, vol. 12, pp. 1707–1710, Mar. 2012.

[27] G.-H. Lee, Y.-J. Yu, C. Lee, C. Dean, K. L. Shepard, P. Kim, and J. Hone, “Electron tunneling through atomically flat and ultrathin hexagonal boron nitride,” *Applied Physics Letters*, vol. 99, p. 243114, Dec. 2011.

[28] K. K. Kim, A. Hsu, X. Jia, S. M. Kim, Y. Shi, M. Dresselhaus, T. Palacios, and J. Kong, “Synthesis and characterization of hexagonal boron nitride film as a dielectric layer for graphene devices,” *ACS Nano*, vol. 6, pp. 8583–8590, Sep. 2012.

[29] Y. Hattori, T. Taniguchi, K. Watanabe, and K. Nagashio, “Layer-by-layer dielectric breakdown of hexagonal boron nitride,” *ACS Nano*, vol. 9, pp. 916–921, Dec. 2014.

[30] S. K. Jang, J. Youn, Y. J. Song, and S. Lee, “Synthesis and characterization of hexagonal boron Nitride as a gate dielectric,” *Scientific Reports*, vol. 6, p. 30449, Jul. 2016.

[31] R. Decker, Y. Wang, V. W. Brar, W. Regan, H.-Z. Tsai, Q. Wu, W. Gannett, A. Zettl, and M. F. Crommie, “Local electronic properties of graphene on a BN substrate via scanning tunneling microscopy,” *Nano Letters*, vol. 11, pp. 2291–5, Jun. 2011.

[32] J. Xue, J. Sanchez-Yamagishi, D. Bulmash, P. Jacquod, A. Deshpande, K. Watanabe, T. Taniguchi, P. Jarillo-Herrero, and B. J. LeRoy, “Scanning tunnelling microscopy and spectroscopy of ultra-flat graphene on hexagonal boron nitride,” *Nature Materials*, vol. 10, pp. 282–5, Feb. 2011.

[33] K. Watanabe, T. Taniguchi, and H. Kanda, “Direct-bandgap properties and evidence for ultraviolet lasing of hexagonal boron nitride single crystal,” *Nature Materials*, vol. 3, pp. 404–409, May. 2004.

[34] A. Laturia, M. L. V. de Put, and W. G. Vandenberghe, “Dielectric properties of hexagonal boron nitride and transition metal dichalcogenides: from monolayer to bulk,” *npj 2D Materials and Applications*, vol. 2, Mar. 2018.

[35] Z. Zhang, S. Hu, J. Chen, and B. Li, “Hexagonal boron nitride: a promising substrate for graphene with high heat dissipation,” *Nanotechnology*, vol. 28, p. 225704, May. 2017.

[36] W. Paszkowicz, J. Pelka, M. Knapp, T. Szyszko, and S. Podsiadlo, “Lattice parameters and anisotropic thermal expansion of hexagonal boron nitride in the 10-297.5 K temperature range,” *Applied Physics A: Materials Science & Processing*, vol. 75, pp. 431–435, Sep. 2002.

[37] R. Bourrellier, S. Meuret, A. Tararan, O. Stéphan, M. Kociak, L. H. G. Tizei, and A. Zobelli, “Bright UV single photon emission at point defects in h-BN,” *Nano Letters*, vol. 16, pp. 4317–4321, Jun. 2016.

[38] T. T. Tran, C. Elbadawi, D. Totonjian, C. J. Lobo, G. Grosso, H. Moon, D. R. Englund, M. J. Ford, I. Aharonovich, and M. Toth, “Robust multicolor single photon emission from point defects in hexagonal boron nitride,” *ACS Nano*, vol. 10, pp. 7331–7338, Jul. 2016.

[39] L. J. Martínez, T. Pelini, V. Waselowski, J. R. Maze, B. Gil, G. Cassabois, and V. Jacques, “Efficient single photon emission from a high-purity hexagonal boron nitride crystal,” *Physical Review B*, vol. 94, Sep. 2016.

[40] Z. Shotan, H. Jayakumar, C. R. Considine, M. Mackoit, H. Fedder, J. Wrachtrup, A. Alkauskas, M. W. Doherty, V. M. Menon, and C. A. Meriles, “Photoinduced modification of single-photon emitters in hexagonal boron nitride,” *ACS Photonics*, vol. 3, pp. 2490–2496, Dec. 2016.

[41] A. W. Schell, T. T. Tran, H. Takashima, S. Takeuchi, and I. Aharonovich, “Non-linear excitation of quantum emitters in hexagonal boron nitride multiplayers,” *APL Photonics*, vol. 1, p. 091302, Sep. 2016.

[42] S. Choi, T. T. Tran, C. Elbadawi, C. Lobo, X. Wang, S. Juodkazis, G. Seniutinas, M. Toth, and I. Aharonovich, “Engineering and localization of quantum emitters in large hexagonal boron nitride layers,” *ACS Applied Materials & Interfaces*, vol. 8, pp. 29642–29648, Oct. 2016.

[43] N. Chejanovsky, M. Rezai, F. Paolucci, Y. Kim, T. Rendler, W. Rouabeh, F. F. de Oliveira, P. Herlinger, A. Denisenko, S. Yang, I. Gerhardt, A. Finkler, J. H. Smet, and J. Wrachtrup, “Structural attributes and photodynamics of visible spectrum quantum emitters in hexagonal boron nitride,” *Nano Letters*, vol. 16, pp. 7037–7045, Oct. 2016.

[44] T. T. Tran, M. Kianinia, M. Nguyen, S. Kim, Z.-Q. Xu, A. Kubanek, M. Toth, and I. Aharonovich, “Resonant excitation of quantum emitters in hexagonal boron nitride,” *ACS Photonics*, vol. 5, pp. 295–300, Nov. 2017.

[45] A. W. Schell, M. Svedendahl, and R. Quidant, “Quantum emitters in hexagonal boron nitride have spectrally tunable quantum efficiency,” *Advanced Materials*, vol. 30, p. 1704237, Feb. 2018.

[46] M. Kianinia, C. Bradac, B. Sontheimer, F. Wang, T. T. Tran, M. Nguyen, S. Kim, Z.-Q. Xu, D. Jin, A. W. Schell, C. J. Lobo, I. Aharonovich, and M. Toth, “All-optical control and super-resolution imaging of quantum emitters in layered materials,” *Nature Communications*, vol. 9, Feb. 2018.

[47] M. Nguyen, S. Kim, T. T. Tran, Z.-Q. Xu, M. Kianinia, M. Toth, and I. Aharonovich, “Nanoassembly of quantum emitters in hexagonal boron nitride and gold nanospheres,” *Nanoscale*, vol. 10, pp. 2267–2274, Dec. 2017.

[48] K. Sridhara, “Growth of hexagonal boron nitride on electrochemically prepared polycrystalline copper substrates,” Master’s thesis, University of Maryland, 2014.

[49] Y. Kubota, K. Watanabe, O. Tsuda, and T. Taniguchi, “Deep ultraviolet light-emitting hexagonal boron nitride synthesized at atmospheric pressure,” *Science*, vol. 317, pp. 932–934, Aug. 2007.

[50] K. S. Novoselov, V. I. Fal′ko, L. Colombo, P. R. Gellert, M. G. Schwab, and K. Kim, “A roadmap for graphene,” *Nature*, vol. 490, pp. 192–200, Oct. 2012.

[51] W. Ren and H.-M. Cheng, “The global growth of graphene,” *Nature Nanotechnology*, vol. 9, pp. 726–730, Oct. 2014.

[52] T. S. Cheng, A. Summerfield, C. J. Mellor, A. Davies, A. N. Khlobystov, L. Eaves, C. T. Foxon, P. H. Beton, and S. V. Novikov, “High-temperature molecular beam epitaxy of hexagonal boron nitride layers,” *Journal of Vacuum Science & Technology B, Nanotechnology and Microelectronics: Materials, Processing, Measurement, and Phenomena*, vol. 36, p. 02D103, Mar. 2018.

[53] M. S. Driver, J. D. Beatty, O. Olanipekun, K. Reid, A. Rath, P. M. Voyles, and J. A. Kelber, “Atomic layer epitaxy of h-BN(0001) multilayers on Co(0001) and molecular beam epitaxy growth of graphene on h-BN(0001)/Co(0001),” *Langmuir*, vol. 32, pp. 2601–2607, Mar. 2016.

[54] H. Park, T. K. Kim, S. W. Cho, H. S. Jang, S. I. Lee, and S.-Y. Choi, “Large-scale synthesis of uniform hexagonal boron nitride films by plasma-enhanced atomic layer deposition,” *Scientific Reports*, vol. 7, Jan. 2017.

[55] J. Jones, B. Beauclair, O. Olanipekun, S. Lightbourne, M. Zhang, B. Pollok, A. Pilli, and J. Kelber, “Atomic layer deposition of h-BN(0001) on RuO_2(110)/Ru(0001),” *Journal of Vacuum Science & Technology A: Vacuum, Surfaces, and Films*, vol. 35, p. 01B139, Jan. 2017.

[56] W. Hao, C. Marichy, C. Journet, and A. Brioude, “A novel two-step ammonia-free atomic layer deposition approach for boron nitride,” *ChemNanoMat*, vol. 3, pp. 656–663, Aug. 2017.

[57] Y. Shi, C. Hamsen, X. Jia, K. K. Kim, A. Reina, M. Hofmann, A. L. Hsu, K. Zhang, H. Li, Z.-Y. Juang, M. S. Dresselhaus, L.-J. Li, and J. Kong, “Synthesis of few-layer hexagonal boron nitride thin film by chemical vapor deposition,” *Nano Letters*, vol. 10, pp. 4134–4139, Oct. 2010.

[58] L. Song, L. Ci, H. Lu, P. B. Sorokin, C. Jin, J. Ni, A. G. Kvashnin, D. G. Kvashnin, J. Lou, B. I. Yakobson, and P. M. Ajayan, “Large scale growth and characterization of atomic hexagonal boron nitride layers,” *Nano Letters*, vol. 10, pp. 3209–3215, Aug. 2010.

[59] X. Li, W. Cai, J. An, S. Kim, J. Nah, D. Yang, R. Piner, A. Velamakanni, I. Jung, E. Tutuc, S. K. Banerjee, L. Colombo, and R. S. Ruoff, “Large-area synthesis of high-quality and uniform graphene films on copper foils,” *Science*, vol. 324, pp. 1312–1314, May. 2009.

[60] A. Reina, S. Thiele, X. Jia, S. Bhaviripudi, M. S. Dresselhaus, J. A. Schaefer, and J. Kong, “Growth of large-area single- and bi-layer graphene by controlled carbon precipitation on polycrystalline Ni surfaces,” *Nano Research*, vol. 2, pp. 509–516, Jun. 2009.

[61] L. Gao, W. Ren, H. Xu, L. Jin, Z. Wang, T. Ma, L.-P. Ma, Z. Zhang, Q. Fu, L.-M. Peng, X. Bao, and H.-M. Cheng, “Repeated growth and bubbling transfer of graphene with millimetre-size single-crystal grains using platinum,” *Nature Communications*, vol. 3, p. 699, Jan. 2012.

[62] Y. Gao, W. Ren, T. Ma, Z. Liu, Y. Zhang, W.-B. Liu, L.-P. Ma, X. Ma, and H.-M. Cheng, “Repeated and controlled growth of monolayer, bilayer and few-layer hexagonal boron nitride on Pt foils,” *ACS Nano*, vol. 7, pp. 5199–206, May. 2013.

[63] H. Cho, S. Park, D.-I. Won, S. O. Kang, S.-S. Pyo, D.-I. Kim, S. M. Kim, H. C. Kim, and M. J. Kim, “Growth kinetics of white graphene (h-BN) on a planarised Ni foil surface,” *Scientific Reports*, vol. 5, p. 11985, Jul. 2015.

[64] K. K. Kim, A. Hsu, X. Jia, S. M. Kim, Y. Shi, M. Hofmann, D. Nezich, J. F. Rodriguez-Nieva, M. Dresselhaus, T. Palacios, and J. Kong, “Synthesis of monolayer hexagonal boron nitride on Cu foil using chemical vapor deposition,” *Nano Letters*, vol. 12, pp. 161–166, Dec. 2011.

[65] Y.-H. Lee, K.-K. Liu, A.-Y. Lu, C.-Y. Wu, C.-T. Lin, W. Zhang, C.-Y. Su, C.-L. Hsu, T.-W. Lin, K.-H. Wei, Y. Shi, and L.-J. Li, "Growth selectivity of hexagonal-boron nitride layers on Ni with various crystal orientations," *RSC Adv.*, vol. 2, pp. 111–115, Nov. 2012.

[66] R. Y. Tay, M. H. Griep, G. Mallick, S. H. Tsang, R. S. Singh, T. Tumlin, E. H. T. Teo, and S. P. Karna, "Growth of large single-crystalline two-dimensional boron nitride hexagons on electropolished copper," *Nano Letters*, vol. 14, pp. 839–46, Jan. 2014.

[67] B. N. Feigelson, V. M. Bermudez, J. K. Hite, Z. R. Robinson, V. D. Wheeler, K. Sridhara, and S. C. Hernández, "Growth and spectroscopic characterization of monolayer and few-layer hexagonal boron nitride on metal substrates," *Nanoscale*, vol. 7, pp. 3694–702, Jan. 2015.

[68] J. K. Hite, Z. R. Robinson, C. R. Eddy, and B. N. Feigelson, "Electron backscatter diffraction study of hexagonal boron Nitride growth on Cu single-crystal substrates," *ACS Applied Materials & Interfaces*, vol. 7, pp. 15200–5, Jul. 2015.

[69] K. Sridhara, B. N. Feigelson, J. A. Wollmershauser, J. K. Hite, A. Nath, S. C. Hernández, M. S. Fuhrer, and D. K. Gaskill, "Electrochemically prepared polycrystalline copper surface for the growth of hexagonal boron nitride," *Crystal Growth & Design*, vol. 17, pp. 1669–1678, Feb. 2017.

[70] P. Zhao, A. Kumamoto, S. Kim, X. Chen, B. Hou, S. Chiashi, E. Einarsson, Y. Ikuhara, and S. Maruyama, "Self-limiting chemical vapor deposition growth of monolayer graphene from ethanol," *The Journal of Physical Chemistry C*, vol. 117, pp. 10755–10763, May. 2013.

[71] W.-H. Lin, V. W. Brar, D. Jariwala, M. C. Sherrott, W.-S. Tseng, C.-I. Wu, N.-C. Yeh, and H. A. Atwater, "Atomic-scale structural and chemical characterization of hexagonal boron Nitride layers synthesized at the wafer-scale with monolayer thickness control," *Chemistry of Materials*, vol. 29, pp. 4700–4707, May. 2017.

[72] X. Lu, M. I. B. Utama, J. Lin, X. Gong, J. Zhang, Y. Zhao, S. T. Pantelides, J. Wang, Z. Dong, Z. Liu, W. Zhou, and Q. Xiong, “Large-area synthesis of monolayer and few-layer $MoSe_2$ films on SiO_2 substrates,” *Nano Letters*, vol. 14, pp. 2419–2425, Apr. 2014.

[73] S. Najmaei, Z. Liu, W. Zhou, X. Zou, G. Shi, S. Lei, B. I. Yakobson, J.-C. Idrobo, P. M. Ajayan, and J. Lou, “Vapour phase growth and grain boundary structure of molybdenum disulphide atomic layers,” *Nature Materials*, vol. 12, pp. 754–759, Jun. 2013.

[74] V. Senthilkumar, L. C. Tam, Y. S. Kim, Y. Sim, M.-J. Seong, and J. I. Jang, “Direct vapor phase growth process and robust photoluminescence properties of large area MoS_2 layers,” *Nano Research*, vol. 7, pp. 1759–1768, Aug. 2014.

[75] J. C. Shaw, H. Zhou, Y. Chen, N. O. Weiss, Y. Liu, Y. Huang, and X. Duan, “Chemical vapor deposition growth of monolayer $MoSe_2$ nanosheets,” *Nano Research*, vol. 7, pp. 511–517, Apr. 2014.

[76] X. Wang, Y. Gong, G. Shi, W. L. Chow, K. Keyshar, G. Ye, R. Vajtai, J. Lou, Z. Liu, E. Ringe, B. K. Tay, and P. M. Ajayan, “Chemical vapor deposition growth of crystalline monolayer $MoSe_2$,” *ACS Nano*, vol. 8, pp. 5125–5131, Apr. 2014.

[77] S. Y. Yang, G. W. Shim, S.-B. Seo, and S.-Y. Choi, “Effective shape-controlled growth of monolayer MoS_2 flakes by powder-based chemical vapor deposition,” *Nano Research*, vol. 10, pp. 255–262, Nov. 2016.

[78] Y. Zhan, Z. Liu, S. Najmaei, P. M. Ajayan, and J. Lou, “Large-area vapor-phase growth and characterization of MoS_2 atomic layers on a SiO_2 substrate,” *Small*, vol. 8, pp. 966–971, Feb. 2012.

[79] J. Zhang, H. Yu, W. Chen, X. Tian, D. Liu, M. Cheng, G. Xie, W. Yang, R. Yang, X. Bai, D. Shi, and G. Zhang, “Scalable growth of high-quality polycrystalline MoS_2 monolayers on SiO_2 with tunable grain sizes,” *ACS Nano*, vol. 8, pp. 6024–6030, May. 2014.

[80] W. Zhou, X. Zou, S. Najmaei, Z. Liu, Y. Shi, J. Kong, J. Lou, P. M. Ajayan, B. I. Yakobson, and J.-C. Idrobo, “Intrinsic structural defects in monolayer molybdenum disulfide,” *Nano Letters*, vol. 13, pp. 2615–2622, May. 2013.

[81] A. Das, S. Pisana, B. Chakraborty, S. Piscanec, S. K. Saha, U. V. Waghmare, K. S. Novoselov, H. R. Krishnamurthy, A. K. Geim, A. C. Ferrari, and A. K. Sood, “Monitoring dopants by Raman scattering in an electrochemically top-gated graphene transistor,” *Nature Nanotechnology*, vol. 3, pp. 210–215, Mar. 2008.

[82] M. Engel, M. Steiner, A. Lombardo, A. C. Ferrari, H. v. Löhneysen, P. Avouris, and R. Krupke, “Light–matter interaction in a microcavity-controlled graphene transistor,” *Nature Communications*, vol. 3, Jan. 2012.

[83] S. Rumyantsev, G. Liu, M. S. Shur, R. A. Potyrailo, and A. A. Balandin, “Selective gas sensing with a single pristine graphene transistor,” *Nano Letters*, vol. 12, pp. 2294–2298, Apr. 2012.

[84] R. Sordan, F. Traversi, and V. Russo, “Logic gates with a single graphene transistor,” *Applied Physics Letters*, vol. 94, p. 073305, Feb. 2009.

[85] X. Yang, G. Liu, A. A. Balandin, and K. Mohanram, “Triple-mode single-transistor graphene amplifier and its applications,” *ACS Nano*, vol. 4, pp. 5532–5538, Oct. 2010.

[86] F. Schwierz, “Graphene transistors,” *Nature Nanotechnology*, vol. 5, pp. 487–496, May. 2010.

[87] W. Gannett, W. Regan, K. Watanabe, T. Taniguchi, M. F. Crommie, and A. Zettl, “Boron nitride substrates for high mobility chemical vapor deposited graphene,” *Applied Physics Letters*, vol. 98, p. 242105, Jun. 2011.

[88] M. H. Khan, H. K. Liu, X. Sun, Y. Yamauchi, Y. Bando, D. Golberg, and Z. Huang, “Few-atomic-layered hexagonal boron nitride: CVD growth, characterization, and applications,” *Materials Today*, vol. 20, pp. 611–628, Dec. 2017.

[89] J. Sun, C. Lu, Y. Song, Q. Ji, X. Song, Q. Li, Y. Zhang, L. Zhang, J. Kong, and Z. Liu, "Recent progress in the tailored growth of two-dimensional hexagonal boron nitride via chemical vapour deposition," *Chemical Society Reviews*, vol. 47, pp. 4242–4257, May. 2018.

[90] H. Li, J. Wu, X. Huang, Z. Yin, J. Liu, and H. Zhang, "A universal, rapid method for clean transfer of nanostructures onto various substrates," *ACS Nano*, vol. 8, pp. 6563–6570, Jun. 2014.

[91] S. Cha, M. Cha, S. Lee, J. H. Kang, and C. Kim, "Low-temperature, dry transfer-printing of a patterned graphene monolayer," *Scientific Reports*, vol. 5, Dec. 2015.

[92] X. Ma, Q. Liu, D. Xu, Y. Zhu, S. Kim, Y. Cui, L. Zhong, and M. Liu, "Capillary-force-assisted clean-stamp transfer of two-dimensional materials," *Nano Letters*, vol. 17, pp. 6961–6967, Oct. 2017.

[93] A. Jain, P. Bharadwaj, S. Heeg, M. Parzefall, T. Taniguchi, K. Watanabe, and L. Novotny, "Minimizing residues and strain in 2D materials transferred from PDMS," *Nanotechnology*, vol. 29, p. 265203, May. 2018.

[94] T. Taniguchi and K. Watanabe, "Synthesis of high-purity boron nitride single crystals under high pressure by using Ba–BN solvent," *Journal of Crystal Growth*, vol. 303, pp. 525–529, May. 2007.

[95] M. Ohring, *Materials Science of Thin Films*. Elsevier Science, 2001.

[96] T. Takahashi, H. Itoh, and A. Takeuchi, "Chemical vapor deposition of hexagonal boron nitride thick film on iron," *Journal of Crystal Growth*, vol. 47, pp. 245–250, Aug. 1979.

[97] S. D. Roberston, "Graphite formation from low temperature pyrolysis of methane over some transition metal surfaces," *Nature*, vol. 221, pp. 1044–1046, Mar. 1969.

[98] B. C. Banerjee, T. J. Hirt, and P. L. Walker, "Pyrolytic carbon formation from carbon suboxide," *Nature*, vol. 192, pp. 450–451, Nov. 1961.

[99] A. E. Karu and M. Beer, “Pyrolytic formation of highly crystalline graphite films,” *Journal of Applied Physics*, vol. 37, pp. 2179–2181, Apr. 1966.

[100] C. Mattevi, H. Kim, and M. Chhowalla, “A review of chemical vapour deposition of graphene on copper,” *J. Mater. Chem.*, vol. 21, no. 10, pp. 3324–3334, 2011.

[101] J. Hamilton and J. Blakely, “Carbon segregation to single crystal surfaces of Pt, Pd and Co,” *Surface Science*, vol. 91, pp. 199–217, Jan. 1980.

[102] S. Bae, H. Kim, Y. Lee, X. Xu, J.-S. Park, Y. Zheng, J. Balakrishnan, T. Lei, H. R. Kim, Y. I. Song, Y.-J. Kim, K. S. Kim, B. Özyilmaz, J.-H. Ahn, B. H. Hong, and S. Iijima, “Roll-to-roll production of 30-inch graphene films for transparent electrodes,” *Nature Nanotechnology*, vol. 5, pp. 574–578, Jun. 2010.

[103] A. Goriachko, He, M. Knapp, H. Over, M. Corso, T. Brugger, S. Berner, J. Osterwalder, and T. Greber, “Self-assembly of a hexagonal boron nitride nanomesh on Ru(0001),” *Langmuir*, vol. 23, pp. 2928–2931, Mar. 2007.

[104] A. Hemmi, C. Bernard, H. Cun, S. Roth, M. Klöckner, T. Kälin, M. Weinl, S. Gsell, M. Schreck, J. Osterwalder, and T. Greber, “High quality single atomic layer deposition of hexagonal boron nitride on single crystalline Rh(111) four-inch wafers,” *Review of Scientific Instruments*, vol. 85, p. 035101, Mar. 2014.

[105] T. Herden, M. Ternes, and K. Kern, “Lateral and vertical stiffness of the epitaxial h-BN monolayer on Rh(111),” *Nano Letters*, vol. 14, pp. 3623–3627, May. 2014.

[106] M. Liu, Y. Li, P. Chen, J. Sun, D. Ma, Q. Li, T. Gao, Y. Gao, Z. Cheng, X. Qiu, Y. Fang, Y. Zhang, and Z. Liu, “Quasi-freestanding monolayer heterostructure of graphene and hexagonal boron nitride on Ir(111) with a zigzag boundary,” *Nano Letters*, vol. 14, pp. 6342–6347, Oct. 2014.

[107] F. Orlando, R. Larciprete, P. Lacovig, I. Boscarato, A. Baraldi, and S. Lizzit, “Epitaxial growth of hexagonal boron nitride on Ir(111),” *The Journal of Physical Chemistry C*, vol. 116, pp. 157–164, Dec. 2011.

[108] N. A. Vinogradov, A. A. Zakharov, M. L. Ng, A. Mikkelsen, E. Lundgren, N. Mårtensson, and A. B. Preobrajenski, “One-dimensional corrugation of the h-BN monolayer on Fe(110),” *Langmuir*, vol. 28, pp. 1775–81, Jan. 2012.

[109] F. Müller, S. Hüfner, and H. Sachdev, “One-dimensional structure of boron nitride on chromium (110) – a study of the growth of boron nitride by chemical vapour deposition of borazine,” *Surface Science*, vol. 602, pp. 3467–3476, Nov. 2008.

[110] S. Caneva, R. S. Weatherup, B. C. Bayer, B. Brennan, S. J. Spencer, K. Mingard, A. Cabrero-Vilatela, C. Baehtz, A. J. Pollard, and S. Hofmann, “Nucleation control for large, single crystalline domains of mono layer hexagonal boron nitride via Si-doped Fe catalysts,” *Nano Letters*, vol. 15, pp. 1867–1875, Feb. 2015.

[111] S. Caneva, R. S. Weatherup, B. C. Bayer, R. Blume, A. Cabrero-Vilatela, P. Braeuninger-Weimer, M.-B. Martin, R. Wang, C. Baehtz, R. Schloegl, J. C. Meyer, and S. Hofmann, “Controlling catalyst bulk reservoir effects for monolayer hexagonal boron nitride CVD,” *Nano Letters*, vol. 16, pp. 1250–1261, Jan. 2016.

[112] S. M. Kim, A. Hsu, M. H. Park, S. H. Chae, S. J. Yun, J. S. Lee, D.-H. Cho, W. Fang, C. Lee, T. Palacios, M. Dresselhaus, K. K. Kim, Y. H. Lee, and J. Kong, “Synthesis of large-area multilayer hexagonal boron nitride for high material performance,” *Nature Communications*, vol. 6, p. 8662, Oct. 2015.

[113] C. M. Orofeo, S. Suzuki, H. Kageshima, and H. Hibino, “Growth and low-energy electron microscopy characterization of monolayer hexagonal boron nitride on epitaxial cobalt,” *Nano Research*, vol. 6, pp. 335–347, Apr. 2013.

[114] W. Auwärter, H. U. Suter, H. Sachdev, and T. Greber, “Synthesis of one monolayer of hexagonal boron nitride on Ni(111) from b-trichloroborazine $(ClBNH)_3$,” *Chemistry of Materials*, vol. 16, pp. 343–345, Jan. 2004.

[115] N. Guo, J. Wei, L. Fan, Y. Jia, D. Liang, H. Zhu, K. Wang, and D. Wu, “Controllable growth of triangular hexagonal boron nitride domains on copper foils by an improved low-pressure chemical vapor deposition method,” *Nanotechnology*, vol. 23, p. 415605, Sep. 2012.

[116] A. Ismach, H. Chou, D. A. Ferrer, Y. Wu, S. McDonnell, H. C. Floresca, A. Covacevich, C. Pope, R. Piner, M. J. Kim, R. M. Wallace, L. Colombo, and R. S. Ruoff, “Toward the controlled synthesis of hexagonal boron nitride films,” *ACS Nano*, vol. 6, pp. 6378–6385, Jun. 2012.

[117] Y.-H. Lee, K.-K. Liu, A.-Y. Lu, C.-Y. Wu, C.-T. Lin, W. Zhang, C.-Y. Su, C.-L. Hsu, T.-W. Lin, K.-H. Wei, Y. Shi, and L.-J. Li, “Growth selectivity of hexagonal-boron nitride layers on Ni with various crystal orientations,” *RSC Adv.*, vol. 2, pp. 111–115, Nov. 2012.

[118] A. Nagashima, N. Tejima, Y. Gamou, T. Kawai, and C. Oshima, “Electronic structure of monolayer hexagonal boron nitride physisorbed on metal surfaces,” *Physical Review Letters*, vol. 75, pp. 3918–3921, Nov. 1995.

[119] A. Nagashima, N. Tejima, Y. Gamou, T. Kawai, and C. Oshima, “Electronic dispersion relations of monolayer hexagonal boron nitride formed on the Ni(111) surface,” *Physical Review B*, vol. 51, pp. 4606–4613, Feb. 1995.

[120] P. C. Yang, J. T. Prater, W. Liu, J. T. Glass, and R. F. Davis, “The formation of epitaxial hexagonal boron nitride on nickel substrates,” *Journal of Electronic Materials*, vol. 34, pp. 1558–1564, Dec. 2005.

[121] A. A. Tonkikh, E. N. Voloshina, P. Werner, H. Blumtritt, B. Senkovskiy, G. Güntherodt, S. S. P. Parkin, and Y. S. Dedkov, “Structural and electronic properties of epitaxial multilayer h-BN on Ni(111) for spintronics applications,” *Scientific Reports*, vol. 6, p. 23547, Mar. 2016.

[122] M. H. Khan, Z. Huang, F. Xiao, G. Casillas, Z. Chen, P. J. Molino, and H. K. Liu, “Synthesis of large and few atomic layers of hexagonal boron nitride on melted copper,” *Scientific Reports*, vol. 5, Jan. 2015.

[123] K. H. Lee, H.-J. Shin, J. Lee, I. yeal Lee, G.-H. Kim, J.-Y. Choi, and S.-W. Kim, “Large-scale synthesis of high-quality hexagonal boron nitride nanosheets for large-area graphene electronics,” *Nano Letters*, vol. 12, pp. 714–718, Jan. 2012.

[124] Y. Stehle, H. M. Meyer, R. R. Unocic, M. Kidder, G. Polizos, P. G. Datskos, R. Jackson, S. N. Smirnov, and I. V. Vlassiouk, “Synthesis of hexagonal boron nitride monolayer: Control of nucleation and crystal morphology,” *Chemistry of Materials*, vol. 27, pp. 8041–8047, Nov. 2015.

[125] Y. Y. Stehle, X. Sang, R. R. Unocic, D. Voylov, R. K. Jackson, S. Smirnov, and I. Vlassiouk, “Anisotropic etching of hexagonal boron nitride and graphene: Question of edge terminations,” *Nano Letters*, vol. 17, pp. 7306–7314, Nov. 2017.

[126] R. Y. Tay, X. Wang, S. H. Tsang, G. C. Loh, R. S. Singh, H. Li, G. Mallick, and E. H. T. Teo, “A systematic study of the atmospheric pressure growth of large-area hexagonal crystalline boron nitride film,” *Journal of Materials Chemistry C*, vol. 2, no. 9, p. 1650, 2014.

[127] M. Corso, “Boron nitride nanomesh,” *Science*, vol. 303, pp. 217–20, Jan. 2004.

[128] F. Müller, S. Hüfner, H. Sachdev, S. Gsell, and M. Schreck, “Epitaxial growth of hexagonal boron nitride monolayers by a three-step boration-oxidation-nitration process,” *Physical Review B*, vol. 82, Aug. 2010.

[129] P. Sutter, J. Lahiri, P. Albrecht, and E. Sutter, “Chemical vapor deposition and etching of high-quality monolayer hexagonal boron nitride films,” *ACS Nano*, vol. 5, pp. 7303–7309, Aug. 2011.

[130] P. Sutter, J. Lahiri, P. Zahl, B. Wang, and E. Sutter, “Scalable synthesis of uniform few-layer hexagonal boron nitride dielectric films,” *Nano Letters*, vol. 13, pp. 276–281, Dec. 2012.

[131] J. Lu, P. S. E. Yeo, Y. Zheng, H. Xu, C. K. Gan, M. B. Sullivan, A. C. Neto, and K. P. Loh, “Step flow versus mosaic film growth in hexagonal boron nitride,” *Journal of the American Chemical Society*, vol. 135, pp. 2368–2373, Jan. 2013.

[132] M. Morscher, M. Corso, T. Greber, and J. Osterwalder, “Formation of single layer h-BN on Pd(111),” *Surface Science*, vol. 600, pp. 3280–3284, Aug. 2006.

[133] F. Müller, S. Hüfner, H. Sachdev, R. Laskowski, P. Blaha, and K. Schwarz, “Epitaxial growth of hexagonal boron nitride on Ag(111),” *Physical Review B*, vol. 82, Sep. 2010.

[134] G. Kim, A.-R. Jang, H. Y. Jeong, Z. Lee, D. J. Kang, and H. S. Shin, “Growth of high-crystalline, single-layer hexagonal boron nitride on recyclable platinum foil,” *Nano Letters*, vol. 13, pp. 1834–1839, Mar. 2013.

[135] F. Müller, K. Stöwe, and H. Sachdev, “Symmetry versus commensurability: epitaxial growth of hexagonal boron nitride on Pt(111) from β-trichloroborazine ($(ClBNH)_3$),” *Chemistry of Materials*, vol. 17, pp. 3464–3467, Jun. 2005.

[136] L. Camilli, E. Sutter, and P. Sutter, “Growth of two-dimensional materials on non-catalytic substrates: h-BN/Au(111),” *2D Materials*, vol. 1, p. 025003, Aug. 2014.

[137] S. Frueh, R. Kellett, C. Mallery, T. Molter, W. S. Willis, C. King’ondu, and S. L. Suib, “Pyrolytic decomposition of ammonia borane to boron nitride,” *Inorganic Chemistry*, vol. 50, pp. 783–92, Feb. 2011.

[138] M. S. Bresnehan, M. J. Hollander, M. Wetherington, M. LaBella, K. A. Trumbull, R. Cavalero, D. W. Snyder, and J. A. Robinson, “Integration of hexagonal boron nitride with quasi-freestanding epitaxial graphene: Toward wafer-scale, high-performance devices,” *ACS Nano*, vol. 6, pp. 5234–5241, May. 2012.

[139] L. Wang, B. Wu, J. Chen, H. Liu, P. Hu, and Y. Liu, “Monolayer hexagonal boron nitride films with large domain size and clean interface for enhancing the mobility of graphene-based field-effect transistors,” *Advanced Materials*, vol. 26, pp. 1559–1564, Dec. 2013.

[140] J. Han, J.-Y. Lee, H. Kwon, and J.-S. Yeo, “Synthesis of wafer-scale hexagonal boron nitride monolayers free of aminoborane nanoparticles by chemical vapor deposition,” *Nanotechnology*, vol. 25, p. 145604, Mar. 2014.

[141] J. C. Koepke, J. D. Wood, Y. Chen, S. W. Schmucker, X. Liu, N. N. Chang, L. Nienhaus, J. W. Do, E. A. Carrion, J. Hewaparakrama, A. Rangarajan, I. Datye, R. Mehta, R. T. Haasch, M. Gruebele, G. S. Girolami, E. Pop, and J. W. Lyding, “Role of pressure in the growth of hexagonal boron nitride thin films from ammonia-borane,” *Chemistry of Materials*, vol. 28, pp. 4169–4179, Jun. 2016.

[142] V. Babenko, G. Lane, A. A. Koos, A. T. Murdock, K. So, J. Britton, S. S. Meysami, J. Moffat, and N. Grobert, “Time dependent decomposition of ammonia borane for the controlled production of 2D hexagonal boron nitride,” *Scientific Reports*, vol. 7, Oct. 2017.

[143] P. Bachmann, F. Düll, F. Späth, U. Bauer, H.-P. Steinrück, and C. Papp, “A HR-XPS study of the formation of h-BN on Ni(111) from the two precursors, ammonia borane and borazine,” *The Journal of Chemical Physics*, vol. 149, p. 164709, Oct. 2018.

[144] J.-H. Park, J. C. Park, S. J. Yun, H. Kim, D. H. Luong, S. M. Kim, S. H. Choi, W. Yang, J. Kong, K. K. Kim, and Y. H. Lee, “Large-area monolayer hexagonal boron nitride on Pt foil,” *ACS Nano*, vol. 8, pp. 8520–8528, Aug. 2014.

[145] H. Oh, J. Jo, Y. Tchoe, H. Yoon, H. H. Lee, S.-S. Kim, M. Kim, B.-H. Sohn, and G.-C. Yi, “Centimeter-sized epitaxial h-BN films,” *NPG Asia Materials*, vol. 8, pp. e330–e330, Nov. 2016.

[146] C. Gomez-Aleixandre, D. Diaz, F. Orgaz, and J. M. Albella, “Reaction of diborane and ammonia gas mixtures in a chemical vapor deposition hot-wall reactor,” *The Journal of Physical Chemistry*, vol. 97, pp. 11043–11046, Oct. 1993.

[147] S. Chatterjee, Z. Luo, M. Acerce, D. M. Yates, A. T. C. Johnson, and L. G. Sneddon, “Chemical vapor deposition of boron nitride nanosheets on metallic substrates via decaborane/ammonia reactions,” *Chemistry of Materials*, vol. 23, pp. 4414–4416, Oct. 2011.

[148] X. Wang, T. N. Hooper, A. Kumar, I. K. Priest, Y. Sheng, T. O. M. Samuels, S. Wang, A. W. Robertson, M. Pacios, H. Bhaskaran, A. S. Weller, and J. H. Warner, “Oligomeric aminoborane precursors for the chemical vapour deposition growth of few-layer hexagonal boron nitride,” *CrystEngComm*, vol. 19, pp. 285–294, Dec. 2016.

[149] C. Zhang, X. Hao, Y. Wu, and M. Du, “Synthesis of vertically aligned boron nitride nanosheets using CVD method,” *Materials Research Bulletin*, vol. 47, pp. 2277–2281, Sep. 2012.

[150] L. Qin, J. Yu, M. Li, F. Liu, and X. Bai, “Catalyst-free growth of mono- and few-atomic-layer boron nitride sheets by chemical vapor deposition,” *Nanotechnology*, vol. 22, p. 215602, Mar. 2011.

[151] J. Yu, L. Qin, Y. Hao, S. Kuang, X. Bai, Y.-M. Chong, W. Zhang, and E. Wang, “Vertically aligned boron nitride nanosheets: Chemical vapor synthesis, ultraviolet light emission, and superhydrophobicity,” *ACS Nano*, vol. 4, pp. 414–422, Jan. 2010.

[152] R. Y. Tay, H. Li, S. H. Tsang, M. Zhu, M. Loeblein, L. Jing, F. N. Leong, and E. H. T. Teo, “Trimethylamine borane: A new single-source precursor for monolayer h-BN single crystals and h-BCN thin films,” *Chemistry of Materials*, vol. 28, pp. 2180–2190, Mar. 2016.

[153] L. Wang, B. Wu, L. Jiang, J. Chen, Y. Li, W. Guo, P. Hu, and Y. Liu, “Growth and etching of monolayer hexagonal boron nitride,” *Advanced Materials*, vol. 27, pp. 4858–4864, Jul. 2015.

[154] X. Song, J. Gao, Y. Nie, T. Gao, J. Sun, D. Ma, Q. Li, Y. Chen, C. Jin, A. Bachmatiuk, M. H. Rümmeli, F. Ding, Y. Zhang, and Z. Liu, “Chemical vapor deposition growth of large-scale hexagonal boron nitride with controllable orientation,” *Nano Research*, vol. 8, pp. 3164–3176, Aug. 2015.

[155] C. Zhang, L. Fu, S. Zhao, Y. Zhou, H. Peng, and Z. Liu, “Controllable co-segregation synthesis of wafer-scale hexagonal boron nitride thin films,” *Advanced Materials*, vol. 26, pp. 1776–1781, Dec. 2013.

[156] G. Lu, T. Wu, Q. Yuan, H. Wang, H. Wang, F. Ding, X. Xie, and M. Jiang, “Synthesis of large single-crystal hexagonal boron nitride grains on Cu-Ni alloy,” *Nature Communications*, vol. 6, p. 6160, Jan. 2015.

[157] Z. Zhang, Y. Liu, Y. Yang, and B. I. Yakobson, “Growth mechanism and morphology of hexagonal boron nitride,” *Nano Letters*, vol. 16, pp. 1398–403, Feb. 2016.

[158] A. Preobrajenski, A. Vinogradov, and N. Mårtensson, “Monolayer of h-BN chemisorbed on Cu(111) and Ni(111): The role of the transition metal 3d states,” *Surface Science*, vol. 582, pp. 21–30, May. 2005.

[159] P. R. Kidambi, R. Blume, J. Kling, J. B. Wagner, C. Baehtz, R. S. Weatherup, R. Schloegl, B. C. Bayer, and S. Hofmann, “In situ observations during chemical vapor deposition of hexagonal boron nitride on polycrystalline copper,” *Chemistry of Materials*, vol. 26, pp. 6380–6392, Nov. 2014.

[160] G. E. Wood, A. J. Marsden, J. J. Mudd, M. Walker, M. Asensio, J. Avila, K. Chen, G. R. Bell, and N. R. Wilson, “van der Waals epitaxy of monolayer hexagonal boron nitride on copper foil: growth, crystallography and electronic band structure,” *2D Materials*, vol. 2, p. 025003, May. 2015.

[161] Y. Wen, X. Shang, J. Dong, K. Xu, J. He, and C. Jiang, “Ultraclean and large-area monolayer hexagonal boron nitride on Cu foil using chemical vapor deposition,” *Nanotechnology*, vol. 26, p. 275601, Jun. 2015.

[162] Q. Wu, J.-H. Park, S. Park, S. J. Jung, H. Suh, N. Park, W. Wongwiriyapan, S. Lee, Y. H. Lee, and Y. J. Song, “Single crystalline film of hexagonal boron nitride atomic monolayer by controlling nucleation seeds and domains,” *Scientific Reports*, vol. 5, p. 16159, Nov. 2015.

[163] X. Li, Y. Li, Q. Wang, J. Yin, J. Li, J. Yu, and W. Guo, “Oxygen-suppressed selective growth of monolayer hexagonal boron nitride on copper twin crystals,” *Nano Research*, vol. 10, pp. 826–833, Jan. 2017.

[164] R.-J. Chang, X. Wang, S. Wang, Y. Sheng, B. Porter, H. Bhaskaran, and J. H. Warner, “Growth of large single-crystalline monolayer hexagonal boron nitride by oxide-assisted chemical vapor deposition,” *Chemistry of Materials*, vol. 29, pp. 6252–6260, Jul. 2017.

[165] Y. Ji, B. Calderon, Y. Han, P. Cueva, N. R. Jungwirth, H. A. Alsalman, J. Hwang, G. D. Fuchs, D. A. Muller, and M. G. Spencer, “Chemical vapor deposition growth of large single-crystal mono-, bi-, tri-layer hexagonal boron nitride and their interlayer stacking,” *ACS Nano*, vol. 11, pp. 12057–12066, Nov. 2017.

[166] K. P. Sharma, S. Sharma, A. K. Sharma, B. P. Jaisi, G. Kalita, and M. Tanemura, “Edge controlled growth of hexagonal boron nitride crystals on copper foil by atmospheric pressure chemical vapor deposition,” *CrystEngComm*, vol. 20, pp. 550–555, Dec. 2017.

[167] M. Li, S. Zhou, R. Wang, Y. Yu, H. Wong, Z. Luo, H. Li, L. Gan, and T. Zhai, “In situ formed nanoparticle-assisted growth of large-size single crystalline h-BN on copper,” *Nanoscale*, vol. 10, pp. 17865–17872, Sep. 2018.

[168] W. Yang, G. Chen, Z. Shi, C.-C. Liu, L. Zhang, G. Xie, M. Cheng, D. Wang, R. Yang, D. Shi, K. Watanabe, T. Taniguchi, Y. Yao, Y. Zhang, and G. Zhang, “Epitaxial growth of single-

domain graphene on hexagonal boron nitride," *Nature Materials*, vol. 12, pp. 792–797, Jul. 2013.

[169] P. Zhuang, W. Lin, H. Chou, A. Roy, W. Cai, and S. K. Banerjee, "Growth of lateral graphene/h-BN heterostructure on copper foils by chemical vapor deposition," *Nanotechnology*, vol. 30, p. 03LT01, Nov. 2018.

[170] X. Gao, S. Wang, and S. Lin, "Defective hexagonal boron nitride nanosheet on Ni(111) and Cu(111): Stability, electronic structures, and potential applications," *ACS Applied Materials & Interfaces*, vol. 8, pp. 24238–24247, Sep. 2016.

[171] G. W. Cushing, V. Johánek, J. K. Navin, and I. Harrison, "Graphene growth on Pt(111) by ethylene chemical vapor deposition at surface temperatures near 1000 K," *The Journal of Physical Chemistry C*, vol. 119, pp. 4759–4768, Feb. 2015.

[172] B. J. Kang, J. H. Mun, C. Y. Hwang, and B. J. Cho, "Monolayer graphene growth on sputtered thin film platinum," *Journal of Applied Physics*, vol. 106, p. 104309, Nov. 2009.

[173] Z. Peng, F. Somodi, S. Helveg, C. Kisielowski, P. Specht, and A. T. Bell, "High-resolution in situ and ex situ TEM studies on graphene formation and growth on Pt nanoparticles," *Journal of Catalysis*, vol. 286, pp. 22–29, Feb. 2012.

[174] P. Zhou, W. J. Hardy, K. Watanabe, T. Taniguchi, and D. Natelson, "Shot noise detection in hBN-based tunnel junctions," *Applied Physics Letters*, vol. 110, p. 133106, Mar. 2017.

[175] S. Caneva, M.-B. Martin, L. D'Arsié, A. I. Aria, H. Sezen, M. Amati, L. Gregoratti, H. Sugime, S. Esconjauregui, J. Robertson, S. Hofmann, and R. S. Weatherup, "From growth surface to device interface: Preserving metallic Fe under monolayer hexagonal boron nitride," *ACS Applied Materials & Interfaces*, vol. 9, pp. 29973–29981, Aug. 2017.

[176] A. Ranjan, N. Raghavan, S. J. O'Shea, S. Mei, M. Bosman, K. Shubhakar, and K. L. Pey, "Conductive atomic force microscope study of bipolar and threshold resistive switching in 2D hexagonal boron nitride films," *Scientific Reports*, vol. 8, Feb. 2018.

[177] A. Summerfield, A. Kozikov, T. S. Cheng, A. Davies, Y.-J. Cho, A. N. Khlobystov, C. J. Mellor, C. T. Foxon, K. Watanabe, T. Taniguchi, L. Eaves, K. S. Novoselov, S. V. Novikov, and P. H. Beton, "Moiré-modulated conductance of hexagonal boron nitride tunnel barriers," *Nano Letters*, vol. 18, pp. 4241–4246, Jun. 2018.

[178] M. Piquemal-Banci, R. Galceran, F. Godel, S. Caneva, M.-B. Martin, R. S. Weatherup, P. R. Kidambi, K. Bouzehouane, S. Xavier, A. Anane, F. Petroff, A. Fert, S. M.-M. Dubois, J.-C. Charlier, J. Robertson, S. Hofmann, B. Dlubak, and P. Seneor, "Insulator-to-metallic spin-filtering in 2D-magnetic tunnel junctions based on hexagonal boron nitride," *ACS Nano*, vol. 12, pp. 4712–4718, Apr. 2018.

[179] X. Wu, R. Ge, P.-A. Chen, H. Chou, Z. Zhang, Y. Zhang, S. Banerjee, M.-H. Chiang, J. C. Lee, and D. Akinwande, "Thinnest nonvolatile memory based on monolayer h-BN," *Advanced Materials*, vol. 31, p. 1806790, Feb. 2019.

[180] Z. Xu, H. Tian, A. Khanaki, R. Zheng, M. Suja, and J. Liu, "Large-area growth of multi-layer hexagonal boron nitride on polished cobalt foils by plasma-assisted molecular beam epitaxy," *Scientific Reports*, vol. 7, p. 43100, Feb. 2017.

[181] S. Chen, W. Cai, R. D. Piner, J. W. Suk, Y. Wu, Y. Ren, J. Kang, and R. S. Ruoff, "Synthesis and characterization of large-area graphene and graphite films on commercial Cu–Ni alloy foils," *Nano Letters*, vol. 11, pp. 3519–3525, Sep. 2011.

[182] J. H. Cho, J. J. Gorman, S. R. Na, and M. Cullinan, "Growth of monolayer graphene on nanoscale copper-nickel alloy thin films," *Carbon*, vol. 115, pp. 441–448, May. 2017.

[183] X. Liu, L. Fu, N. Liu, T. Gao, Y. Zhang, L. Liao, and Z. Liu, “Segregation growth of graphene on Cu–Ni alloy for precise layer control,” *The Journal of Physical Chemistry C*, vol. 115, pp. 11976–11982, May. 2011.

[184] M. J. Madito, A. Bello, J. K. Dangbegnon, C. J. Oliphant, W. A. Jordaan, D. Y. Momodu, T. M. Masikhwa, F. Barzegar, M. Fabiane, and N. Manyala, “A dilute Cu-(Ni) alloy for synthesis of large-area bernal stacked bilayer graphene using atmospheric pressure chemical vapour deposition,” *Journal of Applied Physics*, vol. 119, p. 015306, Jan. 2016.

[185] Z. R. Robinson, P. Tyagi, T. M. Murray, C. A. Ventrice, S. Chen, A. Munson, C. W. Magnuson, and R. S. Ruoff, “Substrate grain size and orientation of Cu and Cu–Ni foils used for the growth of graphene films,” *Journal of Vacuum Science & Technology A: Vacuum, Surfaces, and Films*, vol. 30, p. 011401, Jan. 2012.

[186] Y. Takesaki, K. Kawahara, H. Hibino, S. Okada, M. Tsuji, and H. Ago, “Highly uniform bilayer graphene on epitaxial Cu–Ni(111) alloy,” *Chemistry of Materials*, vol. 28, pp. 4583–4592, May. 2016.

[187] T. Wu, X. Zhang, Q. Yuan, J. Xue, G. Lu, Z. Liu, H. Wang, H. Wang, F. Ding, Q. Yu, X. Xie, and M. Jiang, “Fast growth of inch-sized single-crystalline graphene from a controlled single nucleus on Cu-Ni alloys,” *Nature Materials*, vol. 15, pp. 43–7, Nov. 2015.

[188] C. Yang, T. Wu, H. Wang, G. Zhang, J. Sun, G. Lu, T. Niu, A. Li, X. Xie, and M. Jiang, “Copper-vapor-assisted rapid synthesis of large ab-stacked bilayer graphene domains on Cu-Ni alloy,” *Small*, vol. 12, pp. 2009–13, Feb. 2016.

[189] R. E. Smallman and A. H. W. Ngan, *Modern Physical Metallurgy*. Elsevier Ltd, Oxford, 2013.

[190] W. F. Hosford, *Physical Metallurgy*. CRC Press, Inc., 2010.

[191] R. Petkovic, M. Luton, and J. Jonas, “Recovery and recrystallization of polycrystalline copper after hot working,” *Acta Metallurgica*, vol. 27, pp. 1633–1648, Oct. 1979.

[192] C. Barrett, J. Lytton, and O. Sherby, "Effect of grain size and annealing treatment on steady state creep of copper," tech. rep., DTIC Document, 1965.

[193] W. C. Elmore, "Electrolytic polishing," *Journal of Applied Physics*, vol. 10, pp. 724–727, Oct. 1939.

[194] C. Wagner, "Contribution to the theory of electropolishing," *Journal of The Electrochemical Society*, vol. 101, no. 5, p. 225, 1954.

[195] H. F. Walton, "The anode layer in the electrolytic polishing of copper," *Journal of The Electrochemical Society*, vol. 97, no. 7, pp. 219–226, 1950.

[196] W. C. Elmore, "Electrolytic polishing. II," *Journal of Applied Physics*, vol. 11, pp. 797–799, Dec. 1940.

[197] P. A. Jacquet, "On the anodic behavior of copper in aqueous solutions of orthophosphoric acid," *Transactions of The Electrochemical Society*, vol. 69, p. 629, Jul. 1936.

[198] G. Yang, B. Wang, K. Tawfiq, H. Wei, S. Zhou, and G. Chen, "Electropolishing of surfaces: theory and applications," *Surface Engineering*, vol. 33, pp. 149–166, Jul. 2016.

[199] C. M. A. Brett and A. M. O. Brett, *Electrochemistry: Principles, Methods, and Applications*. Oxford science publications, Oxford University Press, 1993.

[200] T. Brown, *Chemistry: The Central Science*. Mastering Chemistry Series, Pearson Prentice Hall, 2006.

[201] F. A. Lowenheim, *Electroplating: Fundamentals of Surface Finishing*. McGraw-Hill, 1977.

[202] C. M. Cotell, J. A. Sprague, and J. Fred A. Smidt, *Metals Handbook (ASM Handbook): Volume 5. Surface Cleaning, Finishing, and Coating*. American Society for Metals, 1982.

[203] L. Durney, *Graham's Electroplating Engineering Handbook*. Springer, 1984.

[204] M. Schlesinger and M. Paunovic, eds., *Modern Electroplating*. John Wiley & Sons, Inc., Oct. 2010.

[205] L. E. Samuels, *Metallographic Polishing by Mechanical Methods*. ASM International, 2003.

[206] G. H. Han, F. Güneş, J. J. Bae, E. S. Kim, S. J. Chae, H.-J. Shin, J.-Y. Choi, D. Pribat, and Y. H. Lee, "Influence of copper morphology in forming nucleation seeds for graphene growth," *Nano Letters*, vol. 11, pp. 4144–4148, Oct. 2011.

[207] Y. Xiao, H. Kim, C. Mattevi, M. Chhowalla, R. C. Maher, and L. F. Cohen, "Influence of Cu substrate topography on the growth morphology of chemical vapour deposited graphene," *Carbon*, vol. 65, pp. 7–12, Dec. 2013.

[208] T. J. Gnanaprakasa, Y. Gu, S. K. Eddy, Z. Han, W. J. Beck, K. Muralidharan, and S. Raghavan, "The role of copper pretreatment on the morphology of graphene grown by chemical vapor deposition," *Microelectronic Engineering*, vol. 131, pp. 1–7, Jan. 2015.

[209] W. Wang, S. Yang, and A. Wang, "Observation of the unexpected morphology of graphene wrinkle on copper substrate," *Scientific Reports*, vol. 7, Aug. 2017.

[210] R. V. Gorbachev, I. Riaz, R. R. Nair, R. Jalil, L. Britnell, B. D. Belle, E. W. Hill, K. S. Novoselov, K. Watanabe, T. Taniguchi, A. K. Geim, and P. Blake, "Hunting for monolayer boron nitride: Optical and Raman signatures," *Small*, vol. 7, pp. 465–468, Jan. 2011.

[211] R. Laskowski, P. Blaha, and K. Schwarz, "Bonding of hexagonal BN to transition metal surfaces: An ab initio density-functional theory study," *Physical Review B*, vol. 78, Jul. 2008.

[212] P. Braeuninger-Weimer, B. Brennan, A. J. Pollard, and S. Hofmann, "Understanding and controlling Cu-catalyzed graphene nucleation: The role of impurities, roughness, and oxygen scavenging," *Chemistry of Materials*, vol. 28, pp. 8905–8915, Dec. 2016.

[213] Y. Leng, *Materials Characterization*. Wiley VCH Verlag GmbH, 2013.

[214] M. Calleja, M. Tello, and R. Garcia, "Size determination of field-induced water menisci in noncontact atomic force microscopy," *Journal of Applied Physics*, vol. 92, pp. 5539–5542, Nov. 2002.

[215] J. J. D. León, D. M. Fryauf, R. D. Cormia, and N. P. Kobayashi, "Study of the formation of native oxide on copper at room temperature," in *Low-Dimensional Materials and Devices 2016* (N. P. Kobayashi, A. A. Talin, M. S. Islam, and A. V. Davydov, eds.), SPIE, Sep. 2016.

[216] A. Roos, M. Bergkvist, C.-G. Ribbing, and J. Bennett, "Quantitative interface roughness studies of copper oxide on copper," *Thin Solid Films*, vol. 164, pp. 5–11, Oct. 1988.

[217] M. Rauh, P. Wiβmann, and M. Wölfel, "Ellipsometric studies on the oxidation of thin copper films," *Thin Solid Films*, vol. 233, pp. 289–292, Oct. 1993.

[218] A. Ibrahim, S. Akhtar, M. Atieh, R. Karnik, and T. Laoui, "Effects of annealing on copper substrate surface morphology and graphene growth by chemical vapor deposition," *Carbon*, vol. 94, pp. 369–377, Nov. 2015.

[219] K. Hayashi, S. Sato, and N. Yokoyama, "Anisotropic graphene growth accompanied by step bunching on a dynamic copper surface," *Nanotechnology*, vol. 24, p. 025603, Dec. 2012.

[220] X. Li, J. Yin, J. Zhou, and W. Guo, "Large area hexagonal boron nitride monolayer as efficient atomically thick insulating coating against friction and oxidation," *Nanotechnology*, vol. 25, p. 105701, Feb. 2014.

[221] S. Ren, M. Cui, J. Pu, Q. Xue, and L. Wang, "Multilayer regulation of atomic boron nitride films to improve oxidation and corrosion resistance of Cu," *ACS Applied Materials & Interfaces*, vol. 9, pp. 27152–27165, Aug. 2017.

[222] Z. Liu, Y. Gong, W. Zhou, L. Ma, J. Yu, J. C. Idrobo, J. Jung, A. H. MacDonald, R. Vajtai, J. Lou, and P. M. Ajayan, "Ultrathin high-temperature oxidation-resistant coatings of hexagonal boron nitride," *Nature Communications*, vol. 4, Oct. 2013.

[223] Y. Çelik, W. Escoffier, M. Yang, E. Flahaut, and E. Suvacı, “Relationship between heating atmosphere and copper foil impurities during graphene growth via low pressure chemical vapor deposition,” *Carbon*, vol. 109, pp. 529–541, Nov. 2016.

[224] D. Lee, G. D. Kwon, J. H. Kim, E. Moyen, Y. H. Lee, S. Baik, and D. Pribat, “Significant enhancement of the electrical transport properties of graphene films by controlling the surface roughness of Cu foils before and during chemical vapor deposition,” *Nanoscale*, vol. 6, pp. 12943–12951, Sep. 2014.

[225] M. Groover, *Fundamentals of Modern Manufacturing: Materials, Processes, and Systems*. John Wiley & Sons, Inc., Jan. 2010.

[226] S. Kalpakjian and S. Schmid, *Manufacturing Engineering & Technology*. Pearson Education, 2013.

[227] M. Song, X. Liu, and L. Liu, “Size effect on mechanical properties and texture of pure copper foil by cold rolling,” *Materials*, vol. 10, p. 538, May. 2017.

[228] Q. Yu, X. Liu, and D. Tang, “Extreme extensibility of copper foil under compound forming conditions,” *Scientific Reports*, vol. 3, Dec. 2013.

[229] S. M. Kim, A. Hsu, Y.-H. Lee, M. Dresselhaus, T. Palacios, K. K. Kim, and J. Kong, “The effect of copper pre-cleaning on graphene synthesis,” *Nanotechnology*, vol. 24, p. 365602, Aug. 2013.

[230] O. I. Sarajlic and R. G. Mani, “Mesoscale scanning electron and tunneling microscopy study of the surface morphology of thermally annealed copper foils for graphene growth,” *Chemistry of Materials*, vol. 25, pp. 1643–1648, May. 2013.

[231] K. L. Chavez and D. W. Hess, “A novel method of etching copper oxide using acetic acid,” *Journal of The Electrochemical Society*, vol. 148, p. G640, Oct. 2001.

[232] M. Luton, R. Petkovic, and J. Jonas, “Kinetics of recovery and recrystallization in polycrystalline copper,” *Acta Metallurgica*, vol. 28, pp. 729–743, Jun. 1980.

[233] R. A. Petkovic, M. J. Luton, and J. J. Jonas, “Grain size and high-temperature yield strength of polycrystalline copper,” *Metal Science*, vol. 13, pp. 569–572, Oct. 1979.

[234] R. N. Pease and H. S. Taylor, “The reduction of copper oxide by hydrogen,” *Journal of the American Chemical Society*, vol. 43, pp. 2179–2188, Oct. 1921.

[235] M. Z. Butt, “Effect of hydrogen attack on the strength of high purity copper,” *Journal of Materials Science Letters*, vol. 2, pp. 1–2, Jan. 1983.

[236] I. Platzman, R. Brener, H. Haick, and R. Tannenbaum, “Oxidation of polycrystalline copper thin films at ambient conditions,” *Journal of Physical Chemistry C*, vol. 112, pp. 1101–1108, Jan. 2008.

[237] J.-K. Lee, C.-S. Park, and H. Kim, “Sheet resistance variation of graphene grown on annealed and mechanically polished Cu films,” *RSC Adv.*, vol. 4, pp. 62453–62456, Nov. 2014.

[238] J. M. Wofford, S. Nie, K. F. McCarty, N. C. Bartelt, and O. D. Dubon, “Graphene islands on Cu foils: The interplay between shape, orientation, and defects,” *Nano Letters*, vol. 10, pp. 4890–4896, Dec. 2010.

[239] J.-M. Shieh, S.-C. Chang, Y.-L. Wang, B.-T. Dai, S.-S. Cheng, and J. Ting, “Reduction of etch pits of electropolished Cu by additives,” *Journal of The Electrochemical Society*, vol. 151, p. C459, May. 2004.

[240] S. Lee, Y. Chen, and J. Hung, “The investigation of surface morphology forming mechanisms in electropolishing process,” *International Journal of Electrochemical Science*, vol. 7, pp. 12495–12506, Dec. 2012.

[241] S.-C. Chang, J.-M. Shieh, C.-C. Huang, B.-T. Dai, Y.-H. Li, and M.-S. Feng, “Microleveling mechanisms and applications of electropolishing on planarization of copper metalliza-

tion," *Journal of Vacuum Science & Technology B: Microelectronics and Nanometer Structures*, vol. 20, p. 2149, Oct. 2002.

[242] S.-C. Chang, J.-M. Shieh, B.-T. Dai, M.-S. Feng, Y.-H. Li, C. H. Shih, M. H. Tsai, S. L. Shue, R. S. Liang, and Y.-L. Wang, "Superpolishing for planarizing copper damascene interconnects," *Electrochemical and Solid-State Letters*, vol. 6, no. 5, p. G72, 2003.

[243] S.-H. Liu, J.-M. Shieh, C. Chen, K. Hensen, and S.-S. Cheng, "Roles of additives in damascene copper electropolishing," *Journal of The Electrochemical Society*, vol. 153, p. C428, Apr. 2006.

[244] S.-H. Liu, J.-M. Shieh, C. Chen, B.-T. Dai, K. Hensen, and S.-S. Cheng, "Two-additive electrolytes for superplanarizing damascene Cu metals," *Electrochemical and Solid-State Letters*, vol. 8, no. 3, p. C47, 2005.

[245] A. C. Ferrari, J. C. Meyer, V. Scardaci, C. Casiraghi, M. Lazzeri, F. Mauri, S. Piscanec, D. Jiang, K. S. Novoselov, S. Roth, and A. K. Geim, "Raman spectrum of graphene and graphene layers," *Physical Review Letters*, vol. 97, Oct. 2006.

[246] A. C. Ferrari, "Raman spectroscopy of graphene and graphite: Disorder, electron–phonon coupling, doping and nonadiabatic effects," *Solid State Communications*, vol. 143, pp. 47–57, Jul. 2007.

[247] L. Malard, M. Pimenta, G. Dresselhaus, and M. Dresselhaus, "Raman spectroscopy in graphene," *Physics Reports*, vol. 473, pp. 51–87, Apr. 2009.

[248] A. C. Ferrari and D. M. Basko, "Raman spectroscopy as a versatile tool for studying the properties of graphene," *Nature Nanotechnology*, vol. 8, pp. 235–246, Apr. 2013.

[249] L. G. Cançado, A. Jorio, E. H. M. Ferreira, F. Stavale, C. A. Achete, R. B. Capaz, M. V. O. Moutinho, A. Lombardo, T. S. Kulmala, and A. C. Ferrari, "Quantifying defects in graphene

via Raman spectroscopy at different excitation energies," *Nano Letters*, vol. 11, pp. 3190–3196, Jul. 2011.

[250] A. Eckmann, A. Felten, A. Mishchenko, L. Britnell, R. Krupke, K. S. Novoselov, and C. Casiraghi, "Probing the nature of defects in graphene by Raman spectroscopy," *Nano Letters*, vol. 12, pp. 3925–3930, Jul. 2012.

[251] A. Rollett, F. J. Humphreys, G. S. Rohrer, and M. Hatherly, *Recrystallization and Related Annealing Phenomena*. Elsevier Science, 2004.

[252] S. Mahajan, "Formation of annealing twins in f.c.c. crystals," *Acta Materialia*, vol. 45, pp. 2633–2638, Jun. 1997.

[253] C. S. Pande, M. A. Imam, and B. B. Rath, "Study of annealing twins in FCC metals and alloys," *Metallurgical Transactions A*, vol. 21, pp. 2891–2896, Nov. 1990.

[254] A. T. Murdock, A. Koos, T. B. Britton, L. Houben, T. Batten, T. Zhang, A. J. Wilkinson, R. E. Dunin-Borkowski, C. E. Lekka, and N. Grobert, "Controlling the orientation, edge geometry, and thickness of chemical vapor deposition graphene," *ACS Nano*, vol. 7, pp. 1351–1359, Feb. 2013.

[255] K. Hayashi, S. Sato, M. Ikeda, C. Kaneta, and N. Yokoyama, "Selective graphene formation on copper twin crystals," *Journal of the American Chemical Society*, vol. 134, pp. 12492–12498, Jul. 2012.

[256] W. Callister and D. Rethwisch, *Materials Science and Engineering: An Introduction*. John Wiley & Sons Canada, Limited, 9th ed., 2011.

[257] R. S. Barnes, "Diffusion of copper along the grain boundaries of nickel," *Nature*, vol. 166, pp. 1032–1033, Dec. 1950.

[258] F. Bachmann, R. Hielscher, and H. Schaeben, "Texture analysis with MTEX – free and open source software toolbox," *Solid State Phenomena*, vol. 160, pp. 63–68, Feb. 2010.

[259] B. V. Crist, *Handbook of Monochromatic XPS Spectra: The Elements of Native Oxides*. John Wiley & Sons, Inc., 2000.

[260] M. C. Biesinger, B. P. Payne, A. P. Grosvenor, L. W. Lau, A. R. Gerson, and R. S. Smart, "Resolving surface chemical states in XPS analysis of first row transition metals, oxides and hydroxides: Cr, Mn, Fe, Co and Ni," *Applied Surface Science*, vol. 257, pp. 2717–2730, Jan. 2011.

[261] A. P. Grosvenor, M. C. Biesinger, R. S. Smart, and N. S. McIntyre, "New interpretations of XPS spectra of nickel metal and oxides," *Surface Science*, vol. 600, pp. 1771–1779, May. 2006.

[262] B. Payne, M. Biesinger, and N. McIntyre, "The study of polycrystalline nickel metal oxidation by water vapour," *Journal of Electron Spectroscopy and Related Phenomena*, vol. 175, pp. 55–65, Dec. 2009.

[263] M. C. Biesinger, L. W. Lau, A. R. Gerson, and R. S. Smart, "Resolving surface chemical states in XPS analysis of first row transition metals, oxides and hydroxides: Sc, Ti, V, Cu and Zn," *Applied Surface Science*, vol. 257, pp. 887–898, Nov. 2010.

[264] M. C. Biesinger, "Advanced analysis of copper x-ray photoelectron spectra," *Surface and Interface Analysis*, vol. 49, pp. 1325–1334, May. 2017.

[265] A. C. Miller and G. W. Simmons, "Copper by XPS," *Surface Science Spectra*, vol. 2, pp. 55–60, Jan. 1993.

[266] R. P. Vasquez, "CuO by XPS," *Surface Science Spectra*, vol. 5, pp. 262–266, Oct. 1998.

[267] R. P. Vasquez, "Cu_2O by XPS," *Surface Science Spectra*, vol. 5, pp. 257–261, Oct. 1998.

[268] R. P. Vasquez, "$Cu(OH)_2$ by XPS," *Surface Science Spectra*, vol. 5, pp. 267–272, Oct. 1998.

[269] C. Darwin, "XCII. the reflexion of x-rays from imperfect crystals," *The London, Edinburgh, and Dublin Philosophical Magazine and Journal of Science*, vol. 43, pp. 800–829, May. 1922.

[270] W. P. Davey, “Precision measurements of the lattice constants of twelve common metals,” *Physical Review*, vol. 25, pp. 753–761, Jun. 1925.